University of Bremen

Alfred Wegener Institute, Helmholtz Centre for Polar and Marine Research

Structure and variability of the circulation at tidal to intra-seasonal time scales near the 79 North Glacier

Master thesis

submitted in
Postgraduate Programme Environmental Physics

Author:
Luisa von Albedyll
Matr. No: 3031314

Supervisors:
Prof. Dr. Torsten Kanzow
Prof. Dr. Monika Rhein

Tutor:
Dr. Janin Schaffer

Bremen, 18.10.2018

Abstract

Greenland's largest floating ice tongue at the Nioghalvfjerdsfjorden Glacier (79 North Glacier) is thinning, most likely triggered by enhanced submarine melting. The strength of the cavity circulation beneath the floating ice tongue is essentially responsible for the ocean heat flux to the glacier ice and variability in the circulation may have consequences on the basal melt rate. Analyzing four moored records (summers 2016-2017) from the 79 North Glacier calving front, this study characterizes the variability of the cavity circulation and the relative importance of its local and regional drivers. The focus lies on the variability in the currents in Dijmphna Sund, the most relevant export pathway for glacially modified waters out of the glacial cavity. Variability is split into three groups. (1) Half of the variance of the time series is concentrated at sub-daily to daily time scales ($T = 0.25 - 2$ days) and is associated with barotropic tides. (2) Periods of 2-30 days comprise one third of the variance. At those time scales, currents in Dijmphna Sund are weakly linked to sea ice conditions close to the coast and enhanced wind speeds. (3) In periods larger than 30 days, $^1/_6$ of the variance is found. Low-pass filtered Empirical Orthogonal Functions reveal a strong link between the export of glacially modified waters through Dijmphna Sund and the inflow into the glacial cavity. This intra-annual variability of the cavity circulation was also observed by a mooring on the continental shelf 170 km south of the 79 North Glacier. The time series from the calving front and the one from the continental shelf are significantly correlated ($R = 0.65$) and shifted by a time difference of 27 ± 29 hours. The time delay fits well to travel times of baroclinic waves. This suggests that large-scale wave activity may be the main driver of the intra-annual variability of the cavity circulation.

Contents

1 Introduction

1.1 Ocean-glacier interactions in Greenland

Polar ice sheets play an important role in the climate system. Fluctuations in their mass balance have shaped past climatic changes substantially. For example, sea level has risen since the last glacial maximum, i.e., about 20,000 years ago, by over 120 m as a result of mass loss from the ice sheets (e.g., *Church et al.*, 2013). Further, anomalous freshwater contributions during the disintegration of the Laurentide ice sheet covering North America are suspected to have caused the Younger Dryas, a rapid cooling event on the Northern Hemisphere associated with a reduced Atlantic Meridional Overturning circulation (*Fairbanks*, 1989).
The current sea level rise of 3.1 ± 0.3 mm yr^{-1} observed over the last two decades is attributed to ocean thermal expansion (42%) and melting of land ice (58%). The loss of land ice is distributed onto glaciers (21%), the Greenland ice sheet (15%) and the Antarctica ice sheet (8%, *Nerem et al.*, 2018; *WCRP Global Sea Level Budget Group*, 2018). Satellite observations show that the Greenland Ice Sheet loses mass since the early 1990s and that the loss has quadrupled over the past two decades (*Enderlin et al.*, 2014; *Shepherd et al.*, 2012). With respect to sea level, the Greenland Ice Sheet contributed between 2012 and 2016 at a rate of $0.67\,\mathrm{mm\,yr}^{-1}$ (*Bamber et al.*, 2018). Climate models predict an an additional contribution from the Greenland Ice Sheet to global sea level rise of 54-97 mm until the end of the century for a 1.5°C warming szenario (*Marzeion et al.*, 2018).
Widespread retreat and speed-up of marine terminating glaciers, as well as increased surface runoff due to higher surface temperatures are responsible for the observed mass loss of the Greenland Ice Sheet. A large portion of the enhanced ice flux to the ocean is most likely triggered by increased submarine melting at marine-terminating glaciers (e.g., *Hill et al.*, 2017; *Kjeldsen et al.*, 2015; *Straneo and Heimbach*, 2013). Subsequent thinning and accelerated retreat destabilize glaciers and ice shelves and may cause enhanced mass loss. Thus, since the ocean circulation determines the heat flux to the glaciers, a better understanding of the temporal variability of the ocean circulation is of great relevance to improve our predictions of the future contributions to sea level rise from the Greenland Ice Sheet.

Besides sea level rise, increased freshwater release impacts the regional, and most likely the global ocean circulation. Increased ice loss from the Greenland ice sheet contributed to a freshwater anomaly in the North Atlantic Ocean, reaching a total volume of $\sim 3200\,\mathrm{km}^3$ for the time period 1992–2010 (*Bamber et al.*, 2012). A substantial fraction of melt water from Greenland intrudes the ocean at depth and mixes with ambient water (*Straneo et al.*, 2011). When exported off the continental shelf, increased freshwater input is particularly relevant because Greenland's coast is located in the proximity of the North Atlantic dense water formation sites (*Dickson et al.*, 2007). Modeling studies showed that especially melt water from east Greenland reaches the interior of Labrador Sea and may impact the stratification at the convection sites (*Dukhovskoy et al.*, 2016; *Gillard et al.*, 2016). However, it is not well understood yet how the increased melt water alters the Atlantic meridional overturning circulation. Some models suggest a reduction (e.g., *Böning et al.*, 2016; *Weijer et al.*, 2012),

but especially the influence of parameters like runoff location, exact amount and intrusion depth are not well known and only sparsely supported by observations (*Dickson et al.*, 2007; *Gillard et al.*, 2016). Consequently, an improved understanding of the glacial freshwater discharge into the ocean is required to predict the ocean's response to the enhanced ice loss at the Greenland Ice Sheet more realistically.

Key regions to better understand the interactions of the open ocean and marine-terminating glaciers are the glacial fjords around Greenland. Normally, two type of water masses are found in them: light waters of Arctic origin, called Polar Water (PW) and dense, warm waters of Atlantic origin (*Straneo and Cenedese*, 2015). Providing a pathway for the Atlantic water, they steer the flow of warm water to the glacier calving fronts. The dynamics of the fjord's circulation determine the heat transport to the glaciers and the glacial freshwater export to the continental shelf. Within the fjords and on the continental shelves, glacial freshwater may be transformed (e.g., by mixing with waters of Polar or Atlantic origin) before it may modify the hydrographic properties on the continental shelf. Consequently, knowledge of the fjord's dynamics is an important piece to understand ocean-glacier interactions. The fjord's circulation is assumed to result from a combination of different drivers, that interact and exhibit variability at different time scales (*Cottier et al.*, 2010; *Straneo and Cenedese*, 2015; *Sutherland et al.*, 2014a). The most common ones are listed below:

(1) The buoyancy-driven circulation is forced by thermohaline differences. It outputs fresher water at shallow depths and subsequently draws in more saline water at depth (*Motyka et al.*, 2003). The buoyancy-driven circulation is maintained by supply of melt water, i.e., either subglacial runoff (melted at the surface) or basal melt (melted at the ocean-ice interface). Melting along the glacier front (or below a glacial tongue) is strongest at depth, i.e., where the glacier is in contact with the warmest waters. In addition, rising freshwater plumes entrain on their ascent ambient water and thereby enhance the heat transfer until they reach neutral buoyancy. In strongly stratified fjords this level is often reached at the lower limit of the light and cold PW that occupies the upper 100-150 m of the water column (*Straneo and Cenedese*, 2015; *Straneo et al.*, 2011). The buoyancy-driven circulation is thought to be enhanced during summer, because more freshwater is discharged at the grounding line compared to winter when it is driven by basal melt only (*Straneo et al.*, 2011).

(2) Shelf-driven intermediary currents in fjords are induced by density fluctuations at the fjord's mouth. The density gradients between fjord head and mouth can be induced by any forcing, but are often associated with along-shore winds that pile up water at the fjord's mouth inducing downwelling (*Jackson et al.*, 2014; *Straneo et al.*, 2010). This leads to a flow into the fjord in the upper layer and a flow out of the fjord at depth, resulting in a depressed pycnocline within the fjord (*Klinck et al.*, 1981). When the winds calm down and the outer shelf returns to the pre-event state, the circulation reverses (*Straneo et al.*, 2010). Those pulses are associated with strongly sheared, fast flows that reverse in depth and time with a typical duration of 4-10 days (*Jackson et al.*, 2014). When forced by winds, it is expected that the seasonal strength of the intermediary currents is linked to the wind speeds. Waves communicating disturbances in the pycnocline were also shown to initialize a similar intermediary fjord circulation (*Inall et al.*, 2015).

(3) Along-fjord winds influence the fjord circulation (e.g., *Cottier et al.*, 2010; *Klinck et al.*, 1981). A model by *Klinck et al.* (1981) showed that surface circulation can be closely correlated with the winds directed along the fjord, that may be, however, overridden by an intermediary circulation (if present). *Moffat* (2014) showed that in a Patagonian fjord with a shallow sill the local along-fjord wind-driven circulation dominates. During down-

fjord wind events, the existing estuarine circulation is intensified, but during up-fjord wind events the inflow of deep water is significantly reduced and a three-layer exchange flow develops.

(4) Mixing introduced by a variety of processes may lead to water mass modification. In case of vertical mixing, the density stratification will be changed, potentially inducing a mean motion. Wind stress is the dominant driver of mixing in the upper ocean (*Cottier et al.*, 2010). Sea ice enhances the momentum transfer between atmosphere and ocean as long as the floats still move around. *Martin et al.* (2014) found an optimal concentration for increased momentum transfer into the ocean at 80-90% of ice coverage. While sea ice is formed, brine release can induce convective overturning. During times of a closed sea ice cover, other processes like tides can act as exchange agents. For instance, *Kirillov et al.* (2017) observed tides to transport subglacial water from the Flade Isblink Glacier to the continental shelf. In case of silled fjords, tides can cause shelf-fjord exchange flow, introducing a net salt transport and establishing a fjord circulation ("Tidal pumping", see *Boone et al.*, 2017). Apart from tides, low-frequency baroclinic waves can provide kinetic energy for mixing (*Sutherland et al.*, 2014a).

The dynamics of glacial fjord's in Greenland has been subject of an increasing number of recent studies (see *Straneo and Cenedese*, 2015, for a review), but there are still major gaps in understanding the circulation because observations are limited due to logistical challenges of the remoteness of the glacial fjord systems and a semi-permanent sea ice cover (*Sutherland et al.*, 2014a). Most studies focus on fjords in Southern Greenland that reach to tidewater glaciers, for example from west to southeast, Kangia Ice Fjord/Jakobshavn Isbræ(e.g., *Motyka et al.*, 2011), Godthåbsfjord (e.g., *Mortensen et al.*, 2011), and Sermilik Fjord/Helheim Glacier (e.g., *Jackson et al.*, 2014; *Straneo et al.*, 2010). Recently, a number of studies focused also in glacial fjords located North Greenland. Studies on Flade Isblink Ice Cap (Northeast Greenland, 81 °N) explored hydrography, influence of tides and storms and proposed that the outlet glacier has a floating ice tongue (*Bendtsen et al.*, 2017; *Dmitrenko et al.*, 2017; *Kirillov et al.*, 2017). Additionally, circulation at Petermann's glacier that has an extensive ice tongue and is located in North Greenland is described by, e.g., *Johnson et al.* (2011) and *Washam et al.* (2018).

A few wintertime records give some first insights into the seasonality of the fjord circulation (*Boone et al.*, 2017; *Jackson et al.*, 2014; *Mortensen et al.*, 2013), stressing the need of year-long observations (*Straneo and Cenedese*, 2015). This study presents a comprehensive oceanographic data set from the fjord covered by the 79 North Glacier, located in Northeast Greenland. In total, four moorings monitored for seven to twelve months the gateways of the cavity circulation beneath the largest floating ice tongue Greenland's. Those measurements will shed light on the fjord circulation and its seasonal variability near the 79NG. Eventually, those observations will most likely help to improve the general understanding of fjord circulation in Greenland's fjords.

1.2 Ocean influence on the 79 North Glacier

Satellite observations have demonstrated that between 2009 and 2012 60% of the increased mass loss of the Greenland Ice Sheet is forced by enhanced surface runoff and 40% by ice discharge from outlet glaciers that drain the Greenland Ice Sheet (*Enderlin et al.*, 2014; *van den Broeke et al.*, 2009). A large part of Northeast Greenland (approximately 12% of the Greenland Ice Sheet, *Mouginot et al.*, 2015) is drained by the Northeast Greenland Ice Stream (NEGIS), an elongated, narrow region of enhanced flow velocities that reaches deep into the ice sheet (Fig. 1.1 and 1.2, *Joughin et al.*, 2001). Having remained close

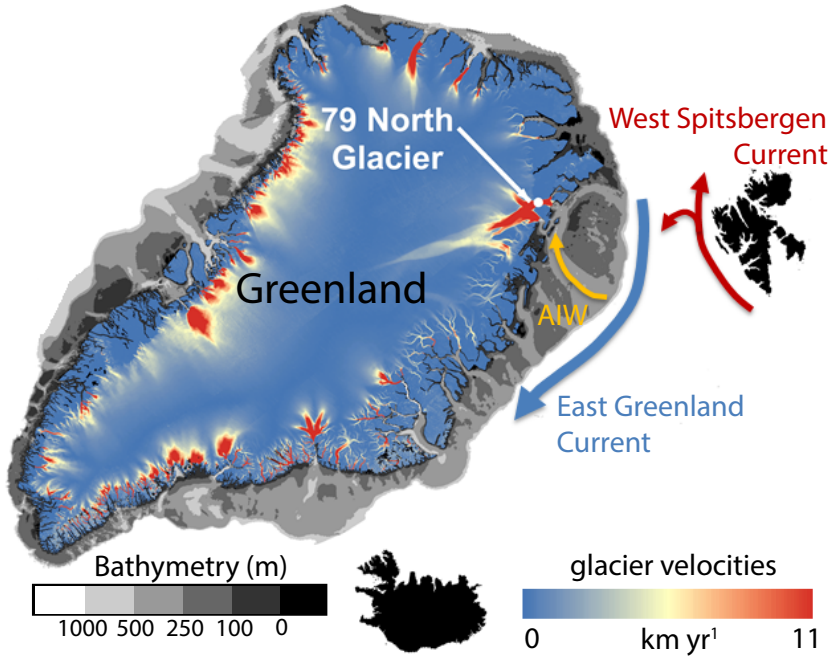

Figure 1.1: Greenland Ice Sheet glacier speeds and major ocean currents in Fram Strait. Warm Atlantic water is transported in the West Spitsbergen current to the Arctic and recirculates in Fram Strait. At the continental shelf break, it is modified to Atlantic Intermediate Water (AIW) and transported to the 79NG. The glacier velocities (provided by ESA) show the 79NG as one outlet of the North East Greenland Ice Stream.

to equilibrium over the last century, the NEGIS seems to respond in more recent years to changes in the climate forcing. Increased surface runoff and enhanced ice discharge via the outlet glaciers of the NEGIS, named Nioghalvfjerdsbræ, Zachariæ Isstrøm and Storstrømmen are the suspected drivers of the observed dynamical thinning (*Khan et al.*, 2014; *Mouginot et al.*, 2015). The floating ice tongue of Zachariæ Isstrøm disintegrated between 2003 and 2012 what lead to an increase in ice discharge by 50% between 1976 and 2015 (*Mouginot et al.*, 2015). The direct neighbor of Zachariæ Isstrøm is Nioghalvfjerdsbræ (Danish for 79 North Glacier, hereafter 79NG). The 79NG has the largest remaining ice shelf in Greenland (70 km long, 20 km wide, Fig. 1.3) whose surface area was remarkably stable. Pinning points at the glacier calving front and upwards sloping bedrock at the grounding line seem to stabilize the glacier. However, recent studies indicate that the floating tongue of the 79NG lost 30% of its thickness from 1999–2014 (*Mouginot et al.*, 2015; *Wilson et al.*, 2017). *Mayer et al.* (2018) showed that the 79NG is out of mass balance equilibrium since 2001. Models predicts a retreat of the grounding line of approximately 10 km within the next 80 years and further thinning of the floating ice tongue (*Choi et al.*, 2017; *Mayer et al.*, 2018). Considering that thin ice is less stable, a disintegration of the ice shelf is likely (*Mayer et al.*, 2018). The mass balance of the 79NG is dominated by submarine melting that accounts for 80% of the annual mass loss when excluding the rare calving events (*Reeh et al.*, 2001; *Wilson et al.*, 2017). *Mayer et al.* (2018) attribute the thinning and its large variability to an increased basal melt due to enhanced heat flux from the ocean. The subglacial melting is triggered by the presence of warm Atlantic waters in the subglacial cavity (*Schaffer et al.*, 2017; *Wilson and Straneo*, 2015). This water mass of Atlantic origin has been observed to warm by 0.5°C in front of the 79NG since the late 1990s (*Schaffer et al.*, 2017). The important role of the ocean to the thinning of the glacier tongue, rises the need for a better understanding of the variability in the oceanic energy flux to the glacier. As summarized above, the glacial fjord circulation is driven by forcing on different time scales and knowledge of those is crucial to understand the temporal variability of the ocean's impact on the 79NG. This thesis intents to contribute to this overarching aim by characterizing variability on time scales shorter than one year of the complex fjord circulation. In the following, a brief overview is given over the known

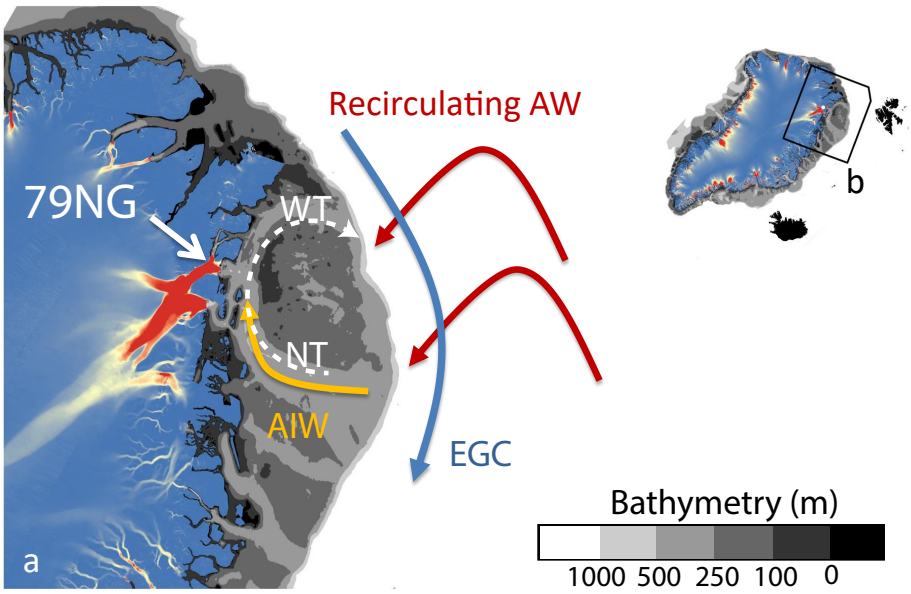

Figure 1.2: Ocean circulation close to and on the Northeast Greenland continental shelf. **a,** Close-up of the Northeast Greenland continental shelf. The East Greenland Current (EGC) transports light Polar Water and recirculated AW along the continental shelf break towards the south. Recirculated Atlantic Water enters the continental shelf and is modified to Atlantic Intermediate Water (AIW). AIW travels in Norske Trough (NT) northwards to the 79NG. The surface circulation (0-200 m deep) is characterized by an anti-cyclonic gyre (white arrow), following the trough system of Norske Trough and Westwind Trough (WT) (*Budéus and Schneider*, 1995; *Schaffer et al.*, 2017). **b,** the black rectangular indicates the region of Greenland displayed in a.

aspects of the hydrographic properties and circulation at the 79NG (Section 1.3). Finally, the focus and concept of this thesis is presented in Section 1.4.

1.3 Hydrographic properties and cavity circulation near the 79 North Glacier

1.3.1 Water masses near the 79 North Glacier

The 79 North glacier is in contact with warm waters of Atlantic origin via a trough system on the Northeast Greenland continental shelf (Fig. 1.1, 1.2, *Schaffer et al.*, 2017). This warm water mass originates from (1) recirculated Atlantic Water (RAW) that is found at the continental shelf break at the entrance of the southern trough (Norske Trough) and (2) modified Arctic Atlantic Water that has been cooled and freshened in the Arctic and is mainly present at the entrance of the trough located to the North (Westwind Trough, 1.2 *Richter*, 2017; *Rudels et al.*, 2005; *Schaffer*, 2017). When mixed onto the continental shelf, the Atlantic water undergoes major transitions leading to a pronounced cooling. Both water masses, transformed RAW and AAW are grouped together under the term Atlantic Intermediate Water (AIW) (*Bourke et al.*, 1987; *Schaffer et al.*, 2017). The warmer part of the AIW is transported via Norske Trough into the 79NG bay, most likely following a continuous pathway deeper than 300 m to the calving front (1.2 *Schaffer*, 2017).

AIW being warmer than 1 °C enters the 79NG cavity through a deep channel in front of the main terminus of the 79NG (1.3, Fig. 1.4, and 1.5) carrying enough heat to melt glacier ice (*Schaffer*, 2017). Most of the melting takes place at the grounding line, where the glacier is in contact with the warmest water (e.g., *Mayer et al.*, 2000; *Wilson and Straneo*, 2015).

Melting occurs in two steps. The ocean heats up the ice to the freezing-point potential temperature that depends on pressure. Then, it further provides the latent heat necessary for the phase change from solid to liquid. As the ocean provides the heat for warming and melting the ice at the glacier base, it cools as result. Basal melt is released which mixes with the ambient water inside the glacier cavity to form a mixture that is fresher and lighter compared to the inflowing AIW (*Straneo and Cenedese*, 2015).

Additionally, subglacial runoff that has drained through cracks and englacial channels to the glacier bed is discharged at the grounding line. Mixing of AIW, basal melt and subglacial runoff forms a plume that is lighter than the surrounding water and ascents along the ice base until it reaches neutral buoyancy. Further mixing with ambient water leads to the formation of glacially modified Atlantic water (mAIW) that leaves the cavity at intermediate depths (approx. 90-250 m).

Using current, potential temperature, and salinity measurements from the main calving front of the 79NG in summer 2016, *Schaffer* (2017) found, that AIW has potential densities of 27.75 to 27.9 $\mathrm{kg\,m^{-3}}$ and temperatures between 0.7 and 1.3 °C in front of the calving front (Fig. 1.4, Fig. 1.5). Such warm water was present only at two of five channels along the glacier calving front (Fig. 1.4).

The mAIW between 120 and 270 m covered a density range between 27.0 and 27.75 $\mathrm{kg\,m^{-3}}$, corresponding to temperatures between -0.5 and 0.7 °C. An Optimum Multiparameter analysis (OMP, see Section 2.1.3 and appendix) based on potential temperature, salinity and dissolved oxygen revealed that in 2016 the mAIW consisted on average of approximately 2% glacial melt water (see Fig. 1.5). Basal melt water accounted for three quarters of the total melt water content (Fig. 1.4, Fig. 1.5). The highest melt water concentrations were present in Dijmphna Sund (Fig. 1.5), i.e., the fjord extending from the minor calving front to the northeast (Fig. 1.3) . Further on the continental shelf, the signature of mAIW becomes less pronounced, possibly induced by mixing with ambient water masses (*Schaffer*, 2017). The upper part of the main pycnocline is formed by PW that exhibits low salinities at potential temperatures close to the freezing point (Fig. 1.5). PW is probably transported from the Arctic ocean onto the continental shelf and not locally formed which is suggested by its nutrient signature that points to a Pacific origin (*Falck*, 2001).

1.3.2 Glacial cavity circulation of the 79 North Glacier

Water exchange across the glacial calving front involves four distinct pathways shaped by the complex bathymetry close to the 79NG (Fig. 1.2, 4.6, *Schaffer*, 2017). All pathways were monitored between summers 2016 and 2017 by moored measurements. While the cavity beneath the floating tongue is deeper than 900 m (*Mayer et al.*, 2000), the bathymetry slopes upwards towards the main calving front, so that the glacier is grounded over a large area. The deepest bathymetric channel and the main gateway for inflow is located between the islands A and the pinning point B (monitored by mooring M2). Here, a 500 m deep depression slopes down into the glacier cavity (Fig. 4.6, *Schaffer*, 2017). Towards the south, there are two more pathways of approximately 300 m depth. The first is located between pinning point B and C (mooring M3) and the second between pinning point D and the coast of Lamberts Land (M4). The bathymetry of the 300 m deep passage is complex and might include a sill of 280 m depth towards the glacier (*Schaffer*, 2017). At the northern, minor calving front that joins into Dijmphna Sund, no such complex bathymetry is known, but the flow is blocked by a 170 m deep sill at the fjord's mouth where mooring M1 was placed (Fig. 1.2).

Wilson and Straneo (2015) proposed that the cavity circulation of the 79NG is a buoyancy-driven estuarine exchange flow, i.e., a circulation mainly determined by the freshwater

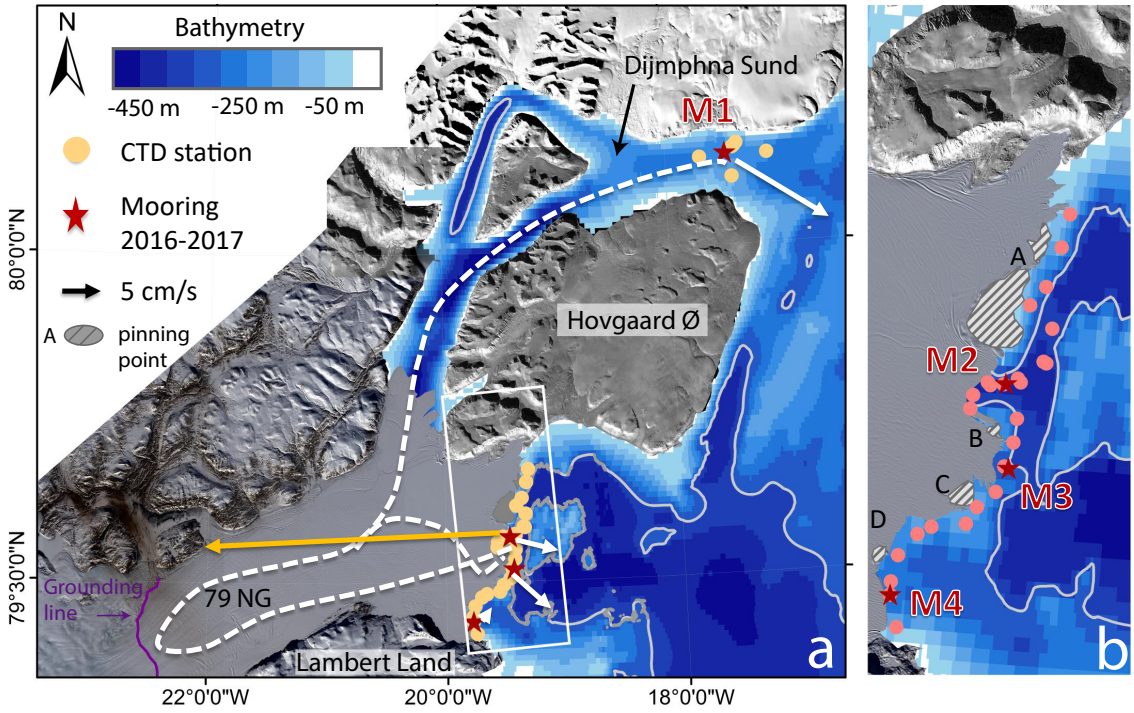

Figure 1.3: Glacial cavity circulation of the 79NG. a, locations of measurement stations (CTD and Mooring M1-M4) at the 79NG calving front and in Dijmphna Sund are displayed. At each mooring site (star), the direction of the strongest flow is indicated by a yellow (flow directed into the cavity) or white (flow directed out of the cavity) arrow. **b,** close-up to the main calving front (see white rectangular in a for extent indicator). The channels to the cavity are located between the pinning points A-D

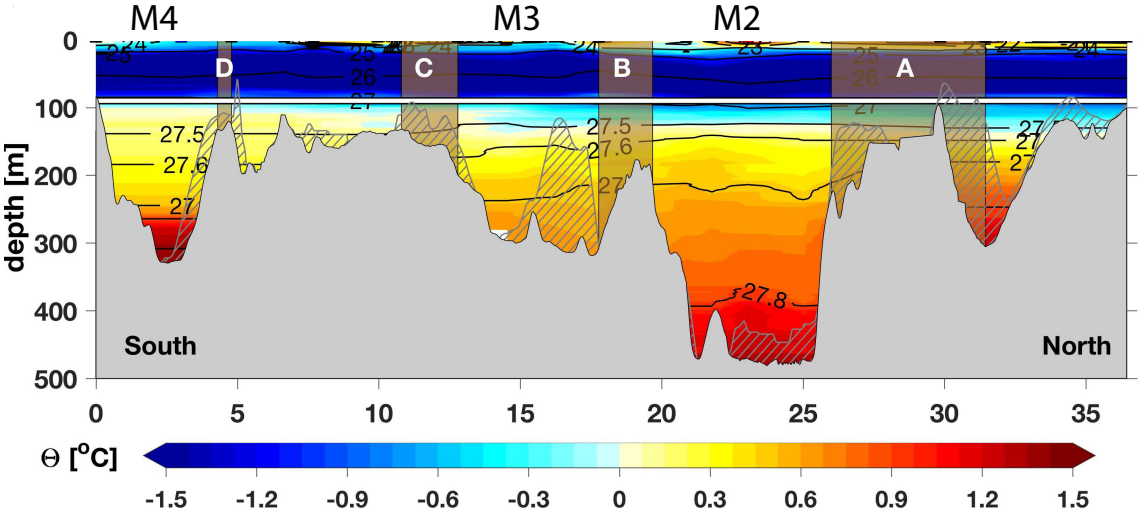

Figure 1.4: Potential Temperature section at the main cavity calving front of the 79NG in summer 2016 during the CTD survey. AIW is present in the cannel between pinning point A and B and between D and the southern coast. Isopycnals are overlain as black lines. Figure adapted from *Schaffer* (2017).

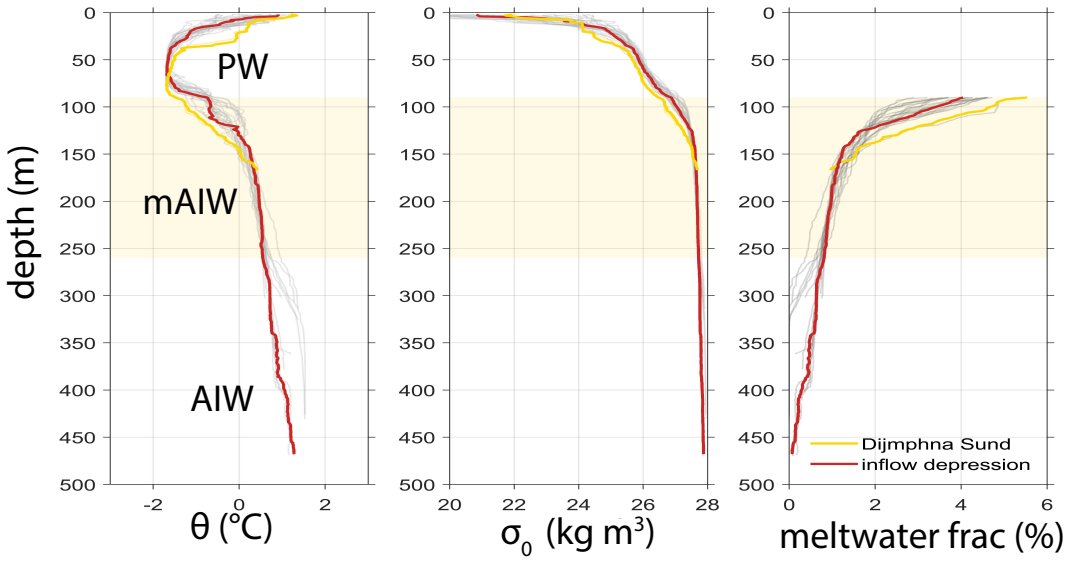

Figure 1.5: Potential temperature, salinity and meltwater content profiles in 2016 for CTD casts at the calving front and in Dijmphna Sund in 2016. **a,** potential temperature profile with indications of water masses. Atlantic Intermediate Water (AIW), glacially modified AIW (mAIW) and Polar Water (PW). A profile taken in Dijmphna Sund (yellow) and one from the inflow depression (red) is highlighted. The depth range in which most outflow is observed is shaded in yellow. **b,** potential density. **c,** melt water fractions beneath 90 m calculated based on an end-member analysis (see Section 2.1.3 and appendix)

supply via basal melting and surface runoff in which inflow takes place as compensation of the export of fresher water. *Schaffer* (2017) suggested that the inflow is additionally hydraulically controlled. Her analysis showed that the bottom-intensified flow that transports AIW into the glacial cavity is associated with a gravity plume that is descending the sill located to the north of shallow bank close to the inflow depression. The density differences between upstream and downstream of the sill arise due to the presence of glacially modified waters in the downstream basin that induce buoyancy gain via mixing. The hydraulically controlled flow is very sensitive to the bifurcation depth, i.e., the height of the AIW layer above the sills that might be influenced by tides, storms, deep convection due to seasonal variability and advected long-term changes (*Schaffer*, 2017).

Balanced transport estimates based on the moored observations weight the relative importance of the different gateways (Fig. 1.6, Schaffer et al 2018, in prep). Inflow of 52 mSv takes place exclusively at the inflow depression (M2) below approx. 240 m. Export is distributed over Dijmphna Sund (-24 mSv) and all other three gateways at the main calving front, i.e., M2 (-13 mSv), M3 (-12 mSv) and M4 (-3 mSv). Dijmphna Sund accounts for almost half of the export and outweighs each of the pathways by almost the double export. Former studies have estimated the role of Dijmphna Sund to be of minor relevance. *Wilson and Straneo* (2015) calculated geostrophic flow velocities of less than $0.3\,\mathrm{m\,s^{-1}}$ below 80 m depth at the mouth of Dijmphna Sund. Furthermore, a moored current meter placed at the glacier rift close to the Dijmphna Sund calving front measured prevailing currents directed to the West, i.e., away from Dijmphna Sund (*Schaffer*, 2017). Indeed, the time series recorded at Dijmphna Sund reveals a strong temporal variability, with velocities varying between $0.1\,\mathrm{m\,s^{-1}}$ and $0.7\,\mathrm{m\,s^{-1}}$ that may explain why single current measurements did not yet capture the fast velocities.

Dijmphna Sund was picked as a suitable start location to study the glacial fjord circulation at the 79NG. Besides the large volume export of mAIW, the melt water fraction analysis

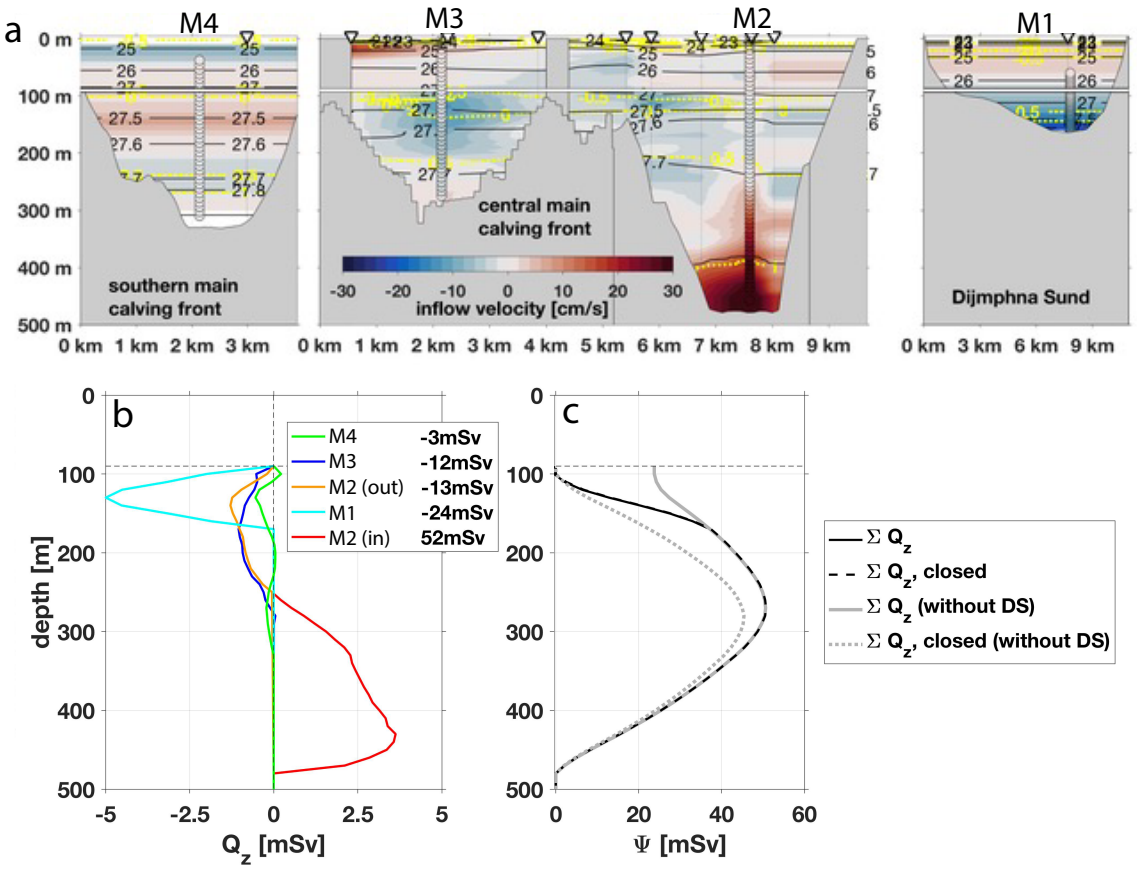

Figure 1.6: Velocity measurements of LADCP survey and balanced transport estimates from moorings. a, velocity section of the four gateways to the glacial cavity from south to north, calculated based on LADCP profiles (triangles) and mean profiles from the moored measurements (circles). Isotherms (yellow lines) and ispycnals (black lines) are overlaid. The cross sections of the channels were used as displayed to calculate transports, displayed in b. **b,** profile of the mean transports for the moorings M1-M4 (Aug 2016-Mar2017). **c,** stream function of the transport; once calculated including Dijmphna Sund (period Aug2016-Mar2017) and excluding Dijmphna Sund (period Aug 2016-Sep 2017). Figure provided by J. Schaffer (personal communication, 2018).

indicated that melt water concentrations were highest, i.e., not only the most, but also the freshest mAIW is exported here (Fig. 4.8). Considering that mAIW higher up in the water column contains more freshwater, and taking into account that mAIW export at Dijmphna Sund takes place at more shallow depths than compared to the main calving front, Dijmphna Sund distributes not only the most mAIW, but also the most freshwater. Fjord processes modifying the circulation in Dijmphna Sund are therefore of high relevance for the freshwater export from the 79NG to the continental shelf. Furthermore, Dijmphna Sund is located about 75 km away from the calving front, i.e., one can assume that lateral gradients, that are most likely present along the calving front, are removed. This may facilitate to bring together the inflow and the outflow of the cavity circulation. Consequently, studying the observed current variability at Dijmphna Sund, their driving force and its link to the observed inflow beneath the 79NG will improve our understanding of the cavity circulation. Thus, it will provide new insights into the ocean-glacier interactions at the 79NG.

1.4 Focus and concept of the thesis

The Sections before summarized the large impact of the ocean on the 79NG on timescales of decades. *Mayer et al.* (2018) showed that the observed thinning of the floating tongue of the 79NG varies strongly on annual time scales, and linked this variability to variations in the ocean heat flux that control the basal melting. The heat flux is set by the heat content of the water and the strength of the cavity circulation. The fact that basal melt is directly linked to variability in the cavity circulation, stresses the need to add knowledge on the ocean's variability. Many of the potential mechanisms influencing the circulation are suspected to exhibit variability at daily to intra-annual time scales (Section 1.1), but only very few observations were available beyond summer campaigns to study those. Between the summers 2016 and 2017, moored hydrographic and current measurements monitored inflow and outflow of the glacial cavity of the 79NG. In this thesis, I will use the data set to characterize the temporal variability of the circulation observed in the export of mAIW through Dijmphna Sund. I will focus on variability on tidal to intra-annual time scales and compare it to external drivers (e.g., wind, sea ice conditions) and the variability observed in the inflowing AIW. Hence, my results are split in two chapters, each guided by one of the following questions:

1. What are the dominant time scales of current variability in Dijmphna Sund and how are they linked to local and regional drivers?

2. How does the cavity circulation influence the variability of mAIW export through Dijmphna Sund?

The characterization of the variability in the cavity circulation aims to establish a consolidated framework to interpret summer measurements. Additionally, it may help to calculate better justified annual basal melt rates from ocean fluxes and could initiate further studies on the impact of short-time variability in basal melting and freshwater export. Furthermore, understanding the processes influencing the cavity circulation is essential for modeling and predicting the response of the cavity circulation to environmental changes.

The remainder of this thesis is laid out as follows: In chapter 2, I present the data sets and the methods I have applied. In chapter 3, I focus on Dijmphna Sund and characterize the temporal variability and its potential local or regional origin by answering questions 1. In Chapter 4, I widen the focus to the cavity circulation to investigate how the variability at Dijmphna Sund is linked to the glacial cavity circulation by answering question 2. In chapter 5, I give a summary and state open points that require further research.

2 Data sets and Methods

This thesis focuses on a set of current time series that were measured by moored instruments from end of August 2016 to the end of September 2017 (Section 2.1.2). Ship-based measurements of hydrographic properties and current speeds, described in Section 2.1.1, were applied to validate the moored observations (Section 3.1.2), to calculate the melt water content (Section 4.5.1) and to put the observations from the moorings in the context of a higher vertical and spatial resolution. Additionally, observed and modeled wind fields (Section 2.2.1), sea ice concentration (Section 2.2.2), and data sets related to the 79NG (Section 2.2.3) were studied to identify potential drivers of the variability in the velocity records. Methods related to specific data sets are described when introducing each data set while the tools related to time series analysis are summarized in a separate Section 2.3.

2.1 Oceanographic data sets

2.1.1 Ship-based measurements

Hydrographic measurements

Hydrographic measurements were carried out in July and August 2016 during the cruise PS100 (*Kanzow*, 2017) and in September and October 2017 during the cruise PS109 (*Kanzow et al.*, 2018b), both on board of the R/V *Polarstern*. In 2016, 29, and in 2017, additional 20 profiles were conducted at the calving front of the 79NG and in Dijmphna Sund (see Fig. 1.3 for locations). A ship-lowered Conductivity-Temperature-Depth (CTD) probe of type SBE 911plus was used to measure conductivity, temperature, and pressure. Additional sensors recorded dissolved oxygen (hereafter oxygen) with a polarographic membrane oxygen sensor of type SBE43. The data sets are available from the World Data Center PANGAEA (*Kanzow et al.*, 2017a,b; *Kanzow et al.*, 2018a). Niskin water bottles attached to the CTD rosette are used to sample the water column at different depths for conductivity and oxygen sensor calibration (*Kanzow et al.*, 2018b).

During processing, CTD data was checked for outliers, compared to the calibration samples and corrected for possible sensor drifts. In addition, all points were averaged into 1 dbar bins (*Rohardt*, 2018). Comparing in-situ salinity measurements taken from the Niskin bottles with the conductivity sensors, revealed a difference of -0.0007 mS m^2 at the beginning and 0.0017 mS m^2 at the end of the cruise in 2017. The CTD data was corrected for the offset assuming a linear drift. Temperature sensors were corrected by 0.00017 °C based on a post-calibration of the instrument (*Rohardt*, 2018). During cruise PS100 a root mean square difference of 0.002 was achieved between salinity bottle data and sensor measurements (*Schaffer*, 2017). Temperature is converted to potential temperature (Θ) to eliminate the thermal effects of compression to compare water masses at different depths. Potential density (ρ) is calculated from salinity and potential temperature and expressed as density anomaly $\sigma_{theta} = \rho - 1000$ kg m^{-3}.

Current measurements

Measurements of current speed and direction were obtained using a Accoustic Doppler Current Profiler (ADCP). Mounted on the CTD rosette, an upward looking and an downward looking instrument were lowered through the water column while they were recording. The measuring principle of an ADCP is based on the Doppler shift. The ADCP sends out an acoustic pulse with constant frequency and records the signal that is backscattered from floating particles that have approximately the size of the wavelength of the signal (for 300 kHz approx. 5 mm). These particles, e.g. plankton, are excited by the sound waves and re-emit them with the same frequency. Assuming that the scatterers move on average with the same horizontal velocity as the currents do, the frequency of the signal is shifted to lower (higher) frequencies, when particles move away from (towards) the source. The ADCP records the frequency and the time of the incoming signals and calculates the Doppler shift (i.e., the difference in frequency) between the sound waves sent out and received. Since the backscatter comes from particles closer and further away from the instrument, travel times are different which is translated into distance. The ADCP set-up of four beams that are tilted by an angle of 20-30°allows to resolve currents in three dimensions. Furthermore, the four beam constellation allows for an error estimate at each depth bin (*Thurnherr*, 2010).

2.1.2 Moorings

The moorings M1-M4 (79NG) and M5 (Île de France) were deployed during the *Polarstern* cruise PS100 in summer 2016 and recovered a year later in summer 2017. While all moorings located along the main calving front recorded data over the whole moored period, the ADCP at M1 stopped recording data on March, 8, 2017 due to low batteries. All moorings were equipped with at least one upward-looking ADCP for current measurements and one SBE37 microCAT for temperature and salinity measurements (Tab. 2.1). Temperature data was logged, depending on the instrument every 30 sec (microCats at M1, M2, M4), 10 min (temperature loggers at M1, M2) or 15 min (micorCat at M3). Velocity was recorded every 30 min (M3) /60 min (M1, M3, M4) in burst mode with a vertical resolution of 4 or 8 m (see Tab. 2.1). Detailed information on the moorings and the measurement instruments are given in Table 2.1. Processed mooring data is about to be archived in the data bank Pangaea with a detailed description of the processing steps (Janin Schaffer, personal communication 2018).
In cases in which measured temperatures recorded from the temperature loggers are compared to microCATs (temperature, salinity and pressure measurements) or CTD measurements, temperature was used instead of potential temperature. For those cases, since measurements were compared at similar depths, the bias is expected to be small.

Transport estimates (section 4.3) were obtained from J. Schaffer (personal communication, 2018). They are based on the velocity records from the moored ADCPs and the cross-sections topography displayed in Figure 1.6. At the deepest channel, where strong current speeds up to 40-50 cm/s were observed, velocities below 250 m depth and 250 m away from the mooring (i.e. close to the sidewalls) have been reduced by 50%. The calculated mean residual mass transport across the entire calving front based on all moored measurements is close to zero. The mass budget has been closed at every timestep by adding a barotropic velocity to achieve compensated transport estimates.

Table 2.1: Basic information on moorings M1-M5 Total water depth, coordinates, and attached instrument are provided for each mooring. For the attached ADPCs, the depth of the deepest measurement and the vertical resolution is stated, separated by "/". For the temperature measurements, the type of instrument and its depth is stated.

Mooring	Water depth	Location	ADCP	Thermometers
M1	172 m	80°8.92'N 17°24.56'W	QMADCP (164 m/4 m)	SBE37 (164 m)
M2	474 m	79°34.13'N, 19 °46.64' W	LRADCP (436/8 m) AQD(457/-)	SBE37(202 m, 460 m) SBE56 (227 m,257 m, 287 m, 317 m, 347 m 377 m, 407 m,427 m)
M3	284 m	79°26.40'N 19 °46.64' W	LRADCP (274 m/8 m)	SBE37 (293 m)
M4	326 m	79 °31,16'N 19°25,82'W	QMADCP (314 m/4 m)	
M5	411 m	78°09.02'N 15 °54.00'W	LRADCP (400 m/8 m)	SBE37(201 m), SBE56 (236 m,266 m, 296 m)

2.1.3 Optimum Multiparameter Analysis

To characterize and distinguish mAIW at different locations, the relative contributions of the source water types that form mAIW were analyzed. An end-member analysis using the Optimum Multiparameter (OMP) approach as described below is used to achieve this goal. The following brief description of the OMP is based on previous work, provided to the reader in the appendix.

End-member water analysis is based on the idea of an unique set of water mass properties whose sinks and sources are only found at boundary interfaces (e.g. ocean/atmopshere, ocean/ice, *Mackas et al.*, 1987). When transported away from the formation site, those properties do not change unless mixing occurs, where the conservative properties combine linearly to a new set of properties. This linearity allows to decompose a new water mass into its source water types by setting up a system of linear equations like the following:

$$d_{obs,i} = \Sigma\ x_i A_i + R_i \tag{2.1}$$

In formula 2.1 each observed property of the water parcel d_{obs} is expressed as a linear combination of fractions x_i of the source-water masses and their characteristic properties A_i. Mass conservation is ensured by adding one equation that sums up all fractions to 1. In the case of an over-determined system (more properties than source water types), it can be solved by an Optimum Multiparameter Analysis (OMP, *Hinrichsen and Tomczak*, 1993; *Huhn et al.*, 2008; *Tomczak and Large*, 1989).

In the ideal case, all observations can be fully explained by the linear equations and the residual R_i is zero. However, uncertainties in the measurements and/or the source water type definitions will lead to nonzero residuals. Therefore, a combination of positive mixing ratios is searched that minimizes the residual, i.e. the deviation between observed and computed properties (*Huhn et al.*, 2008; *Mackas et al.*, 1987). This is commonly done by finding the least squares solution of the problem in matrix formulation:

$$\boldsymbol{Ax} - \boldsymbol{d}_{obs} = \boldsymbol{R} \tag{2.2}$$

In this study, weighted linear equations are solved using the Matlab built in function *lsqnonneg* that solves constraint linear equation systems for both, the over-determined and the critical case. The calculated residuals of the equations are used as a measure of quality (*Huhn et al.*, 2008).

The end-members of the AIW in 2016 and 2017 are found by picking the warmest and most saline measurements taken at the 79NG, i.e. the most outstanding peaks in Θ-S space. To account for variability, a mean of 12 peaks is used to define the final end-member (*Huhn et al.*, 2008). The standard deviation expresses the error of the end-member definition. Oxygen measurements corresponding to the points chosen in Θ-S space are averaged to define the AIW oxygen end-member. A detailed explanation of the end-members of basal melt and runoff which are found by theoretical considerations are explained in the appendix.

2.1.4 Wave speeds

Waves are present at a broad band of frequencies and speeds in the ocean, from high frequency internal waves to low frequency internal seiches. Waves originate when parcels are displaced by an external force in a medium which has a restoring force. The latter pushes the parcels back to its original position where it overshoots and is restored again (*Talley et al.*, 2011).
The speed of waves depends on the type (i.e. the restoring force) and the properties of the medium (e.g. water depth, density). Here, two approximations described in *Talley et al.* (2011) are stated that have been used in section 4.5.2 to estimate wave travel times. Surface gravity waves are induced by any forcing that mounds up or depresses the whole water column while gravity acts as restoring force. Shallow-water (long) gravity waves appear when the wavelengths are greater than the water depth H. Those waves are barotrop and non-dispersive, i.e. their phase speed c_p is constant and equal to the group speed that is given by:

$$c_p = \sqrt{gH} \tag{2.3}$$

Interfacial internal gravity waves describe an internal wave that is traveling along a density interface between two layers of different density within the stratified ocean. They are very similar to gravity waves and their speed is approximated using the reduced gravity (g') in equation 2.3.

$$c_p \approx \frac{\Delta\rho \cdot g}{\rho_0} H_1 = \sqrt{g' H_1} \tag{2.4}$$

Here, ρ_0 is the mean density of both layers, $\Delta\rho$ refers to the difference in density between both layers and H_1 is the mean thickness of the upper layer. This approximation is only valid when the upper layer is much thinner than the lower one. Internal waves have often much larger amplitudes than surface waves because the density contrast between the different water layers is strongly reduced in comparison to the density contrast between ocean and air. They are baroclinic, that implies for example that acceleration in the layers involved is directed to opposite directions.

2.2 Data sets related to atmosphere and cryosphere

2.2.1 Surface wind speeds over the Northeast Greenland continental shelf

Wind observations were obtained from a weather station from the Danish Meteorological Institute on Henrik Kroeyer Holme, a group of islands located in Westwind Trough (80°38'N 13°43'W) about 90 km away from the mooring in Dijmphna Sund and about 170 km away from the main calving front. The data set consists of hourly wind speed and direction at 10 m above ground, together with a quality control flag. The time period between January 2015 and January 2018 was analyzed, but many missing information, particularly during the winter months, lead to the need of an additional data set.

Therefore, wind data from the Japanese 55-year Reanalysis (JRA-55) supported the analysis (*Kobayashi et al.*, 2015). The data set has a resolution of approximately 55 km and contains among other variables wind speed at 10 m above the surface. Prior to the analysis of the wind field described in section 3.3, all points covering the continental shelf were examined. Since there was little difference in the general pattern, the wind information from the pixel, in which the mooring in Dijmphna Sund is located, was considered for further analysis only.

2.2.2 Sea ice concentration on the Northeast Greenland continental shelf

Sea ice concentration data for the Northeast Greenland Shelf was downloaded from the University of Bremen that produces sea ice concentration maps based on the 89 GHz frequency of the Advanced Microwave Scanning Radiometer 2 (AMSR2) with a resolution of 3.125 km (AMSR2 *Grosfeld et al.*, 2016; *Spreen et al.*, 2008). This data set was chosen because due to its high spatial resolution it contained information on the sea ice conditions in the narrow (10 km wide) Dijmphna Sund. Sea ice data was analyzed for September 2016 until March 2017 covering the same period as the current measurements do.

2.2.3 Basal melt rate estimates using the fluxgate approach

To investigate a potential influence of freshwater supply from the 79NG on the fjord circulation, a fluxgate approach was chosen to estimate the basal melt rate (section 4.5.1). The fluxgate approach is based on estimating the difference of ice transport passing through an upper and lower gate within a certain time and to attribute the difference to basal melt. Therefore, it requires (a) glacier speeds from 2016 and 2017, (b) the grounding line and calving front position, (c) glacier thickness at the fluxgates, and (d) the surface mass balance for 2016 and 2017. In the following, the data sets (a)-(d) are described (see also Tab. 2.2). Second, a short review on the fluxgate method is given, mainly based on *Enderlin and Howat* (2013).

(a) Glacier speeds for 2016 were calculated using feature tracking on a set of six cloud-free optical images from 2016/05/04 to 2016/09/03 taken by Landsat 8 (NASA). For details on the method, the reader is directed to *Fahnestock et al.* (2016) and for a recent application of feature tracking on glacier velocities to *Messerli et al.* (2014). To ensure similar viewpoint and illumination conditions to reduce the noise, only images from similar satellite paths were taken that were acquired temporally close (max. one month apart). Feature tracking measures displacements between unique features as e.g. crevasses or debris on two images separated in time and relates them to surface motion. The displacement is found by moving a search window (here approx. 2 km × 2 km, corresponding to four times the expected displacement) by steps of 240 m and calculating the cross-correlation between each patch of an image. The highest correlation was expected to correspond to the displacement that

was converted to velocity taking into account the time difference between the images. By averaging the results of all five image pairs, an average glacier speed with a resolution of 250 m was produced. The displacement measured on stationary features close to the glacier was used to quantify the error of the speed, resulting in $\pm$ 105 m yr^{-1} (*Bevan et al.*, 2012; *Messerli et al.*, 2014; *Paul et al.*, 2017).

For 2017 glacier speeds, there was already a data set with very similar characteristics available from ESA (Greenland Ice Sheet CCI). The glacier surface velocities have been created from feature-tracking of optical Sentinel-2 data (horizontal resolution 12 m) acquired between 2017/06/25 and 2017/08/10. The resolution of the data product is 50 m. An error estimate of $\pm$ 204 m was obtained by calculating the standard deviation of pixels over stable terrain (*Paul et al.*, 2017).

(b) The current grounding line zone (from 2017/03/05) of the 79NG was also available from ESA (Greenland Ice Sheet CCI). Remote sensing observations cannot provide direct measurements of the grounding line, but InSAR (Interferometric Synthetic Aperture Radar) provided by the ERS-1/-2 SAR tandem mission and Sentinel-1 SAR is able to detect the tidal flexure zone by identifying very small changes in surface elevation and movements. The calving front was mapped for both years from optical images.

(c) The ice thickness at the grounding line and the claving front was extracted from BedMachine v3 Greenland (*Morlighem et al.*, 2017) that is compiled from a NASA's Operation IceBridge overflight in 2014 (*Mouginot et al.*, 2015, , supplement). The uncertainty is provided in the data set with $\pm$ 20 m. The ice thickness data were compared at the calving front with the freeboard of the floating tongue in 2013-2015 taken from the ArcticDEM (Polar Geospatial Centre), a high-resolution digital elevation model (5 m resolution). Estimating the total thickness of the floating ice tongue with a mean density of 970 kg m^{-3} of the glacial tongue indicated similar results as the one from BedMachine.

(d) Monthly surface mass balance data for 2016 and 2017 were obtained from B. Noël (personal communication, 2018). The data set is created by downscaling a RACMO2.3p2 run at 5.5 km resolution to 1 km resolution. The physics of the RACMO2.3p2 model are described in *Noël et al.* (2018).

Based on the grounding line and the calving front the fluxgates were defined. The first fluxgate was set at the location of the grounding line. The second fluxgate is located 15 km upstream of the calving front, before the 79NG splits into the main calving front and the minor calving front towards Dijmphna Sund. Since *Wilson et al.* (2017) showed that basal melting is negligible close to the calving front, the associated error was expected to be small.

To calculate basal melt rates, the steps that are explained in the following, are conducted (*Enderlin and Howat*, 2013):

1. Calculate discharge at both fluxgates, one located at the grounding line and one close to calving front (equation 2.5).
2. Estimate thinning due to divergence using the glacier geometry (equation: 2.6).
3. Take the difference between both fluxgates, correct for the divergence and add the surface mass balance to obtain the basal melt rate (equation 2.7).

1. *Discharge* was calculated at the grounding line (subscript g) and at the calving front fluxgate (subscript f) using velocity (u), ice thickness (h) and glacier width (w) using the following equation:

$$Q = u \cdot h \cdot w \tag{2.5}$$

Table 2.2: Overview of glacial data sets used for basal melt rate estimates

type of dataset	creator (reference)	reference date	resolution	additional information
grounding line	ESA Glacier CCI	March 2017		used for 2016 and 2017, constructed from InSAR ERS-1/-2 and Sentinel-1
glacier velocities 2016	this study	April to Sept. 2016	240 m	based on optical feature tracking
glacier velocities 2017	ESA Glacier CCI	June to August 2017	50 m	based on optical feature tracking
ice thickness	BedMachine Greenland (*Morlighem et al.*, 2017; *Mouginot et al.*, 2015)	2014	150 m	mass conservation over grounded ice and airborne gravity inversion over the floating ice tongue (*Mouginot et al.*, 2015). Freeboard estimates of glacier tongue from ArcticDEM (Polar Geospatial Centre)
SMB	B. Noël	monthly, 2016-2017	1 km	reanalyse data using RAMCMO2.3p2 (*Noël et al.*, 2018)

2. *Divergence (Div* was calculated following *Enderlin and Howat* (2013) based on the speed gradient $\frac{U_g - U_f}{L}$, the width gradient $\frac{W_g - W_f}{L}$, the mean ice thickness $H_{mean} = \frac{H_g + H_f}{2}$, and the mean glacier width $W_{mean} = \frac{W_g + W_f}{2}$. L is referring to the length of the glacier along the main flow line. Consequently, divergence is given by:

$$Div = H_{mean} \cdot \frac{U_g - U_f}{L} \cdot \frac{W_g - W_f}{L} \cdot W_{mean} \cdot L \tag{2.6}$$

3. The surface mass balance (SMB) reflects an average at both fluxgate locations. Finally, the *basal melt rate* was calculated by

$$m_{basal} = \frac{Q_g - Q_f + Div}{W_{mean} \cdot L} + SMB \tag{2.7}$$

Here, m_{basal} refers to an average of the whole floating ice tongue per year.

2.3 Time series analysis

A basic purpose of time series analysis is to define the variability of a data series. Often, a signal consists of periodic and aperiodic components that are superimposed on a secular (long-term) trend and biased by uncorrelated random noise (**?**). To differentiate those components, various tools are available that are described below, mainly based on **?** and lecture material from *Lilly* (2017a).
The framework of the time series analysis is given by some general considerations. The fundamental frequency f_1 is the lowest frequency (longest period) that can be resolved, i.e., it describes a signal with a period equal to the total length of the record T:

$$f_1 = \frac{1}{N\Delta t} = \frac{1}{T} \tag{2.8}$$

N refers to the number of measurements and Δt to the time between two measurements. The record length also determines the frequency resolution, i.e. how much two signals with frequencies f_1 and f_2 must differ to be detectable that equals the fundamental frequency

$$\delta f = |f_2 - f_1| = \frac{1}{N\Delta t} = \frac{1}{T} \tag{2.9}$$

The upper limit of the resolved spectra is given by the Nyquist frequency that is defined as

$$f_N = \frac{1}{2\Delta t} \tag{2.10}$$

and states that it takes at least two sampling intervals (i.e. three data points) to resolve a sinusoidal signal with frequency f_N. In practical applications, noise and measurement errors may increase this theoretical limit to rather four or more data points. Energy from frequencies unresolved by the sampling (too low or too high), is redistributed to the resolved frequencies and may cause errors, called aliasing.

Prior to many calculations, the data sets were interpolated linearly and filtered using the jlab toolbox by J. Lilly (*Lilly*, 2017b) and the Matlab built-in functions *butter* and *filtfilt*. The low-pass filters were constructed using a Hanning-filter. Since the start and end of the filtered time series is contaminated by edge-effects, those points are often lost. To avoid such a reduction, the time series is mirrored at the edge. Nevertheless, one needs to consider this fact when interpreting the end points. The band-pass filters were constructed as butter-worth filters of fourth order that have been proved before to be the most stable for the data used. They were applied with a function that performs zero-phase filtering that is achieved by filtering in both directions to avoid frequency dependend shifts of the signal (Matlab function *filtfilt*).

Cross-covariance functions characterize the linear dependence of two time series (x, y) and were used to calculate correlation coefficients for different time lags k. The normalized cross-covariance function $\rho_{x,y}$ is defined by:

$$C_{x,y}(k\Delta t) = \frac{1}{N-1} \sum_{1}^{N-k} [y_i - \bar{y}][x_{i+k} - \bar{x}] \tag{2.11}$$

$$\rho_{x,y} = \frac{C_{x,y}(k\Delta t)}{\sigma_x \sigma_y} \tag{2.12}$$

where σ refers to the variance of the time series. The value of the cross-covariance function C at lag 0 was given as a measure of correlation (correlation coefficient, **?**, p.374-376).

Spectral estimates

Time series analysis can be done in time and in frequency domain. To transform a time series into the frequency domain, the Fourier transformation can be used. This method is based on the principle that one can decomposed a stationary time series into a linear combination of sines and cosines, called a Fourier series. For a discrete time series $y(t)$ of finite length N, the Fourier series has the form

$$y(t_n) = \frac{1}{2}A_0 + \sum_{p=1}^{N/2} [A_p \cos(2\pi f_p t) + B_p \sin(2\pi f_p t)] \tag{2.13}$$

where f_p are multiples of the fundamental frequency and n refers to different time steps $t_n = t_1, t_2, ..., t_N = n \cdot \Delta t$. Important requirement for the functions used is that they are

independent from each other, i.e. the coefficients can be determined independently and that a finite number of Fourier coefficients will result in the minimum mean square error between the original data and the fitted Fourier combination. The contributions of each function with frequency f_p are weighted by the constant Fourier coefficients A_p, B_p that describe the relative contribution of this frequency to the observed signal. This concept is used when estimating the power spectrum of a time series that displays the energy per unit frequency bandwidth for each frequency. The coefficients A_p and B_p are obtained by multiplying the Fourier series by $\cos(f_p t)$ and $\sin(f_p t)$, respectively and sum them up.

$$A_p = \frac{2}{N} \sum_{n=1}^{N} y_n \cos(\frac{2\pi pn}{N}) \tag{2.14}$$

$$A_0 = \frac{2}{N} \sum_{n=1}^{N} y_n \tag{2.15}$$

$$B_p = \frac{2}{N} \sum_{n=1}^{N} y_n \sin(\frac{2\pi pn}{N}) \tag{2.16}$$

$$B_0 = 0 \tag{2.17}$$

The squared amplitudes of the coefficients A_p and B_p refer to the variance of the frequency band and is called spectral energy.

The considerations mode above can be expanded to vector properties, e.g., velocity that is expressed as complex value.

$$w(t) = u(t) + iv(t) \tag{2.18}$$

When calculating the spectrum of the complex-valued velocity, it is possible to split the spectra in a u and v component, or in positive and negative parts, related to an clockwise and counterclockwise sense of rotation of the circular components. In the second case, the spectrum is called rotary spectrum. The current vector $w(t)$ can be expressed as Fourier series (here of infinite length:)

$$w(t) = \bar{u(t)} + i\bar{v(t)} + \sum_{p=1}^{\infty} \{e^{\frac{(\epsilon_p^+ + \epsilon_p^-)}{2}} [A_p^+ + A_p^-] \cos(w_p t + \frac{i(\epsilon_p^+ + \epsilon_p^-)}{2}) \tag{2.19}$$

$$+ i(A_p^+ - A_p^-) \sin(w_p t + \frac{(\epsilon_p^+ + \epsilon_p^-)}{2})\} \tag{2.20}$$

where A_p^+ and A_p^- reflect the amplitudes of the rotary components and ϵ_p^+ and ϵ_p^- the corresponding phase angles.

The result of Fourier analysis on a discrete time series is a periodogram spectral estimate. This estimate differs from the true spectrum because of the finite length of the time series. It can be considered as the product of an infinitely long time series with a rectangular window, that is zero outside of the sampled time, and one during the sampled time. When transforming this product, the resulting spectrum is distorted by the rectangle function. Therefore, when using the *direct periodiogram method* to calculate the Fourier coefficients, a form of filtering is required to reduce the edge-effects. This is archived by using the Multi-taper method, that smooths the undesirable effects of the rectangle function. Additionally, the multiplication with the set of orthogonal functions (tapers) leads to frequency-domain averaging that increases the statistical reliability of the spectrum.

The resulting periodogram spectral estimate of the rotary components is normalized such that the sum of the negative (SNN) and the positive (SPP) component approximates the

variance of the time series of length N. Consequently, the variance of the time series is then equal to

$$\sigma^2_{odd} = \frac{1}{2\pi} \cdot (f_2 - f_1) \cdot (\sum_{2}^{N} \mathrm{SPP} + \sum_{2}^{N} \mathrm{SNN}) \tag{2.21}$$

$$\sigma^2_{even} = \frac{1}{2\pi} \cdot (f_2 - f_1) \cdot (\sum_{2}^{N-1} \mathrm{SPP} + \sum_{2}^{N-1} \mathrm{SNN}) \tag{2.22}$$

In case N is even (σ^2_{even}), the calculation is adapted (as shown) to avoid the duplication of the Nyquist frequency (*Lilly*, 2017a). In this study, variance is used as measure of variability. For a discrete time series y of length N with the mean $\bar{y}$, an estimate of the variance is given by:

$$\sigma^2 \equiv= \frac{1}{N} \sum_{i=1}^{N} [y_i - \bar{y}]^2 \tag{2.23}$$

When variance is quantified in this study in respect to different frequency ranges, it was calculated integrating the spectral estimate as expressed in equation 2.22 over a certain frequency range. Figure 3.6 illustrates the areas that have been integrated. The spectral estimates have been calculated with a Matlab routine provided by J. Lilly that calculates multi-taper spectra (*Lilly*, 2017b).

Harmonic Analysis

While Fourier analysis can only fit amplitudes to multiples of the fundamental frequency, harmonic analysis provides another approach to determine the relative importance of well-known frequencies. Here, it is used to fit functions at tidal frequencies to the discrete time series. Since there are more observations than functions of interest, this leads to an overdetermined problem which is solved by using optimization techniques. That implies to minimize the squared difference between the original data and the fit of the time series as it is implemented in the Matlab package t-tide (see *Pawlowicz et al.*, 2002, for details).

Wavelets

When the amplitudes of the different functions of the Fourier analysis vary in time, the basic assumption of the Fourier analysis is violated. In such cases of non-stationary time series, wavelet transforms are more suited because they "unwrap" the spectrum across time. A wavelet is an oscillating function that is localized in time. For instance, the Morlet wavelet, that is the product of a complex exponential function, that controls the oscillation, multiplied by a Gaussian that leads to the localization in time. Calculating a wavelet transform means comparing the variability of the original time series with the known variability of the mother wavelet. This mother wavelet can be trimmed to have varying degrees of oscillation at each time step of the time series. In this way, the mother wavelet can be used to estimate the variability at each time step. Hereby, resolution in time and frequency still obey the Heisenberg uncertainty relation $\Delta t \Delta f < \frac{1}{4}\pi$, i.e., increasing the temporal resolution decreases the frequency resolution and vice versa. Here, generalized morse wavelets were calculated and applied on the time series, using the functions provided by the toolbox of J. Lilly (*Lilly*, 2017b). The morse wavelets are controlled by two parameters. One characterizes the symmetry of the wavelets in the frequency domain. The other one describes the bandwidth of the frequency domain. Increasing this parameter leads to highly time-localized as opposed to frequency-localized wavelets. Plotting the

averaged amplitude of each frequency at each time step leads to a wavelet plot as e.g. 4.5. For details on morse wavelets and the mathematical expressions of wavelts in general see also *Lilly and Olhede* (2012).

Empirical Orthogonal Functions

Empirical orthogonal function analysis (EOFs, also known as principal component analysis) is an inverse technique that decomposes a signal Ψ into a linear combination of orthogonal functions ϕ (also called statistical "modes") scaled by an amplitude α. This can be written as

$$\Psi(z_m, t) = \sum_{i=1}^{M} \alpha_i(t)\phi_i(m) \tag{2.24}$$

with the orthogonality condition (δ_{ij} is Kronecker delta)

$$\sum_{m=1}^{M} \phi_i(m)\phi_j(m) = \delta_{ij} \tag{2.25}$$

EOFs have the advantage that variability, that is not coherent within the data set, is suppressed and connections between the records are emphasized. For a unique determination of the EOFs, the amplitudes are uncorrelated over the sample data. Prior to calculations, the time series is de-trended.

Usually, already the first few functions account for most of the variance of the time series and their pattern may be, but does not have to be linked to a dynamical mechanism. EOFs therefore provide a compact description of the spatial and temporal variability of a data series. Mathematically, the EOF analysis is equivalent to solving for eigenvectors (the EOFs) and corresponding eigenvalues (the amplitude) of a matrix. In matrix formulation this can be written as

$$\boldsymbol{C\Phi} - \lambda \boldsymbol{I\Phi} = 0 \tag{2.26}$$

where $\boldsymbol{C}$ represents the covariance matrix, $\boldsymbol{I}$ is the unity matrix, λ the variance in each mode, and $\boldsymbol{\Phi}$ are the eigenvectors. Solving the eigenvalue problem includes transformation the system into a diagonal matrix that represents a set of orthogonal functions, the EOFs. In the diagonal matrix, the EOFs are ordered by the variance that is associated with them, i.e. the first mode contains the highest percentage of total variance. In total, the variance of the time series equals the sum of the variance in the eigenvalues. The modes reflect a variation in both directions around the mean. Their amplitude (phase and magnitude) is determined by the time dependent amplitudes of the EOFs that are given by:

$$\alpha_i(t) = \sum_{m=1}^{M} \Psi_m(t)\Phi(m)_i \tag{2.27}$$

An example of EOFs and their amplitudes are displayed in Fig. 4.7.

3 Export of glacially modified waters via Dijmphna Sund

Section 1.3.2 stressed the high relevance of Dijmphna Sund as an export pathway of mAIW. Located between the 79NG and Westwind Trough, it provides a channelized pathway for freshwater allowing freshwater to flow from the 79NG cavity onto the continental shelf. Local and remote drivers are likely to influence the fjord's circulation that eventually determines when and where the freshwater is exported. Following research question 1, the aim of this chapter is to characterize the structure and the variability of the currents observed at the mouth of Dijmphna Sund and to associate the variations with potential drivers.
The chapter is structured as follows: First, the prevailing water mass properties and currents are laid out. Based on this, the temporal variability of the currents is characterized at different time scales. Finally, a possible link between the current speeds and strong winds as well as reduced sea ice concentration is investigated as a potential driver of the local circulation. In this spatial context, I define flow directed away from the glacier as outflow, and flow towards the calving front as inflow.

3.1 Hydrography and circulation at Dijmphna Sund

3.1.1 Water masses in Dijmphna Sund

In summers 2016 and 2017, measurements were conducted at the mouth of Dijmphna Sund, 75 km offshore of the smaller, northern calving front of the 79NG (for details see 2.1.1). A sill of maximal 170 m depth separates the fjord from the southern end of Westwind Trough (see Fig. 1.3). CTD profiles retrieved in 2016 and 2017 show the presence of two water masses (Fig. 3.1 a,b). The upper part of the water column (approx. 30-90 m) is occupied by Polar Water, that is characterized by the coldest temperatures close to the freezing line and forms the upper part of the pycnocline (for details see section 1.3.1). In the 30 m thick surface layer, the temperature is highly seasonal. The observations from 2016 represent summer conditions with surface temperatures up to 1 °C, while profiles from 2017 exhibit a low stratification that may be related to mixing due to sea ice formation and subsequent brine release.
Below 80-110 m mAIW is located, characterized by relatively warm temperatures (-0.5 to 0.7 °C) and high densities (27.0-27.75 $kg\,m^{-3}$) (*Schaffer*, 2017). At the bottom, a temperature maximum of 0.4 °C (2016) and 0.9 °C (2017) is observed, which is substantially colder than the AIW entering the cavity at the main calving front that has temperatures of of 1.3 °C (2016) and 1.8 °C (2017). In Θ-S space, observations from Dijmphna Sund plot close to the melting line (Gade-line) connecting the AIW end-member with a hypothetical end-member of basal melt (Fig. 3.1 c). With decreasing depths, the properties change due to entrainment of runoff and mixing with overlying Polar Waters.

At 169 m, a moored temperature sensor recorded the chronology of the warming in the mAIW that was observed in the CTD casts already (Fig. 3.1 d). Overall, the warming trend appears almost linear with deviations by a few pronounced potential temperature peaks of up to 1.5°C. A linear interpolation of the potential temperature indicates an

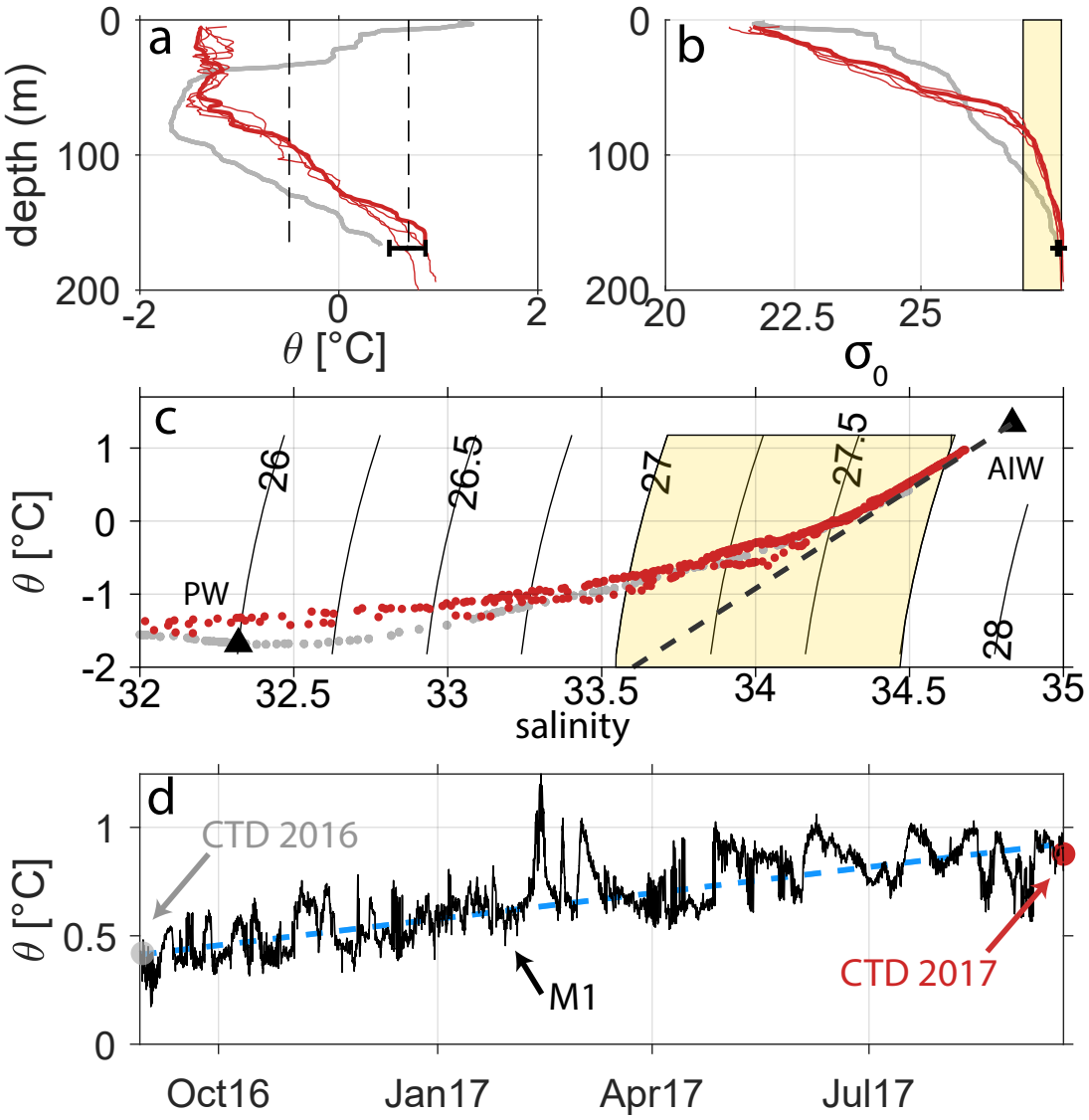

Figure 3.1: Hydrographic properties at the mouth of Dijmphna Sund based on ship-lowered profiles taken in summers 2016 (gray) and 2017 (red) and the moored temperature record from M1 (black). The density range of the mAIW water (27.-27.75) is marked yellow. **a,** potential temperature profiles. The black bars indicate the mean and standard deviation of the temperature time series of the moored instrument **b,** Potential density profiles. **c,** Θ-S characteristics of CTD data with salinities larger than 32. The melting line (dashed) and the end-members of AIW and PW (black triangles) are given. **d,** Time series of potential temperature of M1 with estimated linear trend (blue dashed) and CTD measurements from 2016 (gray dot) and 2017 (red dot).

increase of 0.51 °C within the yearlong observation. The temperature variability (standard deviation of 0.18 °C) is 2.8-times lower in comparison to the overall warming of 0.51 °C. Changes in temperature and salinity are positively correlated (R=0.92), such that a drop in temperature corresponds to a decrease in salinity and potential density. However, the temporal variability of the temperature is neither correlated to magnitude nor direction of the flowrecorded by the ADCP and described in the following sections.
The CTD profiles from 2016 and 2017 confirm that the warming has taken place over the whole mAIW layer as temperatures have risen at all depths below 90 m by 0.4 to 0.5 °C (Fig. 3.1 a). Applying the density definition of mAIW (σ=27.0-27.75 kg m^{-3}) of *Schaffer* (2017), results not only in a change of the properties of mAIW, but also in an increase in thickness of the mAIW layer by 30 m.

In the following chapter, I will consider a depth of 90 m as the upper limit of the mAIW water mass at Dijmphna Sund because both characteristics of mAIW described by *Schaffer* (2017) are fulfilled at this depth: The potential temperature is larger than 0.5 °C and the potential density anomaly has reached 27.0 kg m^{-3}. The following sections of this chapter will focus on the subsurface circulation carrying mAIW from the 79NG cavity onto the continental shelf.

3.1.2 Current speeds in Dijmphna Sund

Validation of the flow direction in Dijmphna Sund

Prior to any analysis of the currents, the flow direction measured by the moored instrument was validated by comparing it to LADCP and vessel-mounted ADCP measurements from the deployment (Fig. 3.2). All measurements indicate flow towards the East, with a magnitude of about 10 cm s^{-1}. There is a good agreement of SADCP and LADCP data in direction and magnitude. The moored ADCP agrees in magnitude with the other measurements. However, the moored ADCP deviates from LADCP and SADCP in direction by up to 40 °to the South. On average, there is an offset of 13 °in direction between 100 and 160 m.

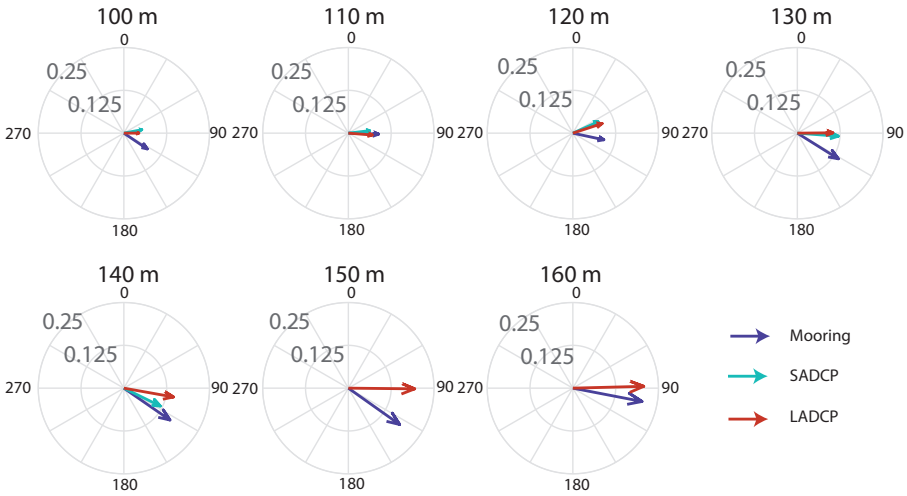

Figure 3.2: Comparison of LADCP, SADCP and moored ADCP measurements at the mooring location. The measurements are compared on a 10 m vertical resolution for the 2016/08/29, 1:30 am (bottom time of LADCP). For the moored velocities, the measurement at 1:00 am and 2:00 am was averaged.

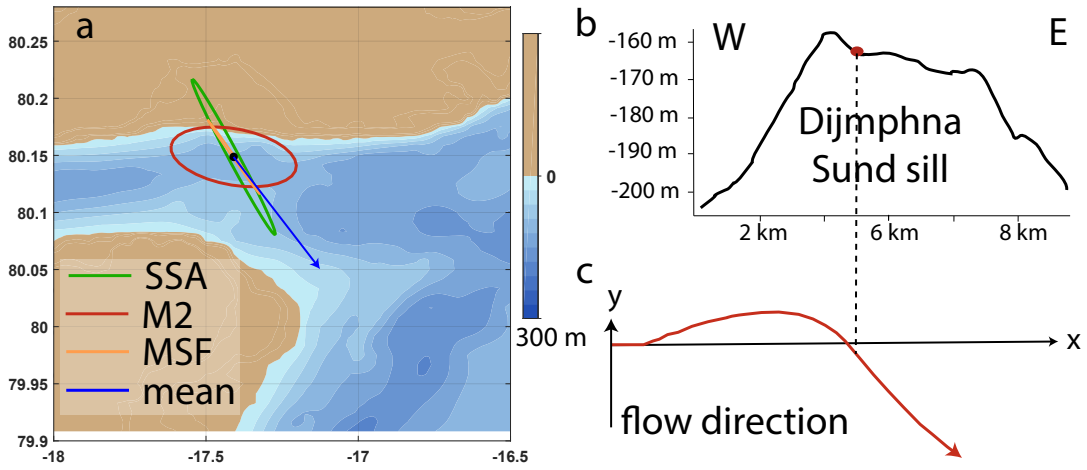

Figure 3.3: Tidal ellipses and vorticity conservation over the Dijmphna Sund sill. a, mooring location (black dot), tidal ellipses and direction of mean flow. M2 is aligned parallel to the bathymetry based on RTopo-2 (*Schaffer et al.*, 2016). **b,** west-east depth profile over the sill at the mouth of Dijmphna Sund. The mooring location is marked by a red dot. **c,** Schematic trajectories of a water parcel in x,y plane of westerly flow over a topographic barrier (*Holton*, 2004).

This systematic deviation raises the question whether a general offset exist in the moored measurements. The northern coastline is orientated west-east and supports the direction suggested by the SADCP and LADCP measurements. However, considering the geometry of the southern shore (headland), it seems possible that the flow has a component that turns towards the south at the mouth of the fjord. Additional evidence is given by tidal currents which primarily follow the topography. Tidal analysis revealed currents in two major directions. The stronger one is orientated towards the southeast, and the second one is aligned west-east (Fig. 3.3a, see section 3.2 for more details). The presence of this second component aligned parallel to the topography makes a systematic offset unlikely. One of the potential causes for a deviation from a purely west-east directed current may be related to the conservation of potential vorticity on top of the sill where the mooring is located (Fig. 3.3b). A rough estimate (see below) shows that the turning of the flow due to the increase in the sea floor height is expected to be in the same order of magnitude as the observed deviation from a pure west-east orientation:

The mean flow at the mooring location is

$$\begin{pmatrix} u_1 \\ v_1 \end{pmatrix} = \begin{pmatrix} 7.6\,\mathrm{cm\,s^{-1}} \\ -9.8\,\mathrm{cm\,s^{-1}} \end{pmatrix}. \tag{3.1}$$

Assuming an hypothetical flow of identical magnitude at a distance of 6 km (x=6 km, y=0 km) in front of the sill towards the east, results in

$$\begin{pmatrix} u_0 \\ v_0 \end{pmatrix} = \begin{pmatrix} 12.4\,\mathrm{cm\,s^{-1}} \\ 0 \end{pmatrix}. \tag{3.2}$$

The change in relative vorticity ξ between both stations is given by

$$\xi = \frac{\Delta v}{\Delta x} - \frac{\Delta u}{\Delta y} \tag{3.3}$$

$$\Delta\xi_1 = \xi_0 - \xi_1 = 0 - 1.6 * 10^{-5}\,\mathrm{s^{-1}} \tag{3.4}$$

$$= -1.6 * 10^{-5}\,\mathrm{s^{-1}}. \tag{3.5}$$

Estimating the vorticity change by the equation of potential vorticity leads to.

$$P = \frac{\xi + f}{h} = const. \tag{3.6}$$

$$\Delta\xi_2 = f(\frac{h_2}{h_1} - 1) = -2.63 * 10^{-5}\,\mathrm{s}^{-1}. \tag{3.7}$$

with $h_1 = 170\,m$, $h_2 = 208\,m$ and $f = 1.4363 \cdot 10{-}4\ \mathrm{s}^{-1}$ the Coriolis parameter at 80 °. Since $\Delta\xi_1 \approx \Delta\xi_2$, potential vorticity conservation may be responsible for the turning of the flow.

To sum up, tidal analysis confirms that there is a component in the flow parallel to the topography and the bathymetry offers a plausible explanation why the flow turns to the southeast as it was recorded by the moored ADCP. A weaker flow, as observed during tidal influence, will be less deviated. Consequently, the measured direction of the moored ADCP appears reasonable. Deviations of the lowered ADCP measurements may be related to the high temporal and spatial variability characterized in the next sections.

Mean flow at Dijmphna Sund

Having confidence in the measured directions, the analysis of the average flow direction reveals a prevailing flow direction to the southeast (131 °), i.e. out of Dijmphna Sund (see Fig. 1.3). Within the mAIW layer, the mean flow direction varies with depth by ±15 °. Therefore, the current time series was rotated into the mean flow direction of the strongest (absolute) flow (i.e., by 132 °). The flow profile obtained in this way shows a bottom-intensified flow with maximum speeds of 12.4 cm s^{-1} at 144 m (Fig. 3.4 a). Towards the bottom, the flow is slowed down by friction. Averaged over depth and time, the downstream

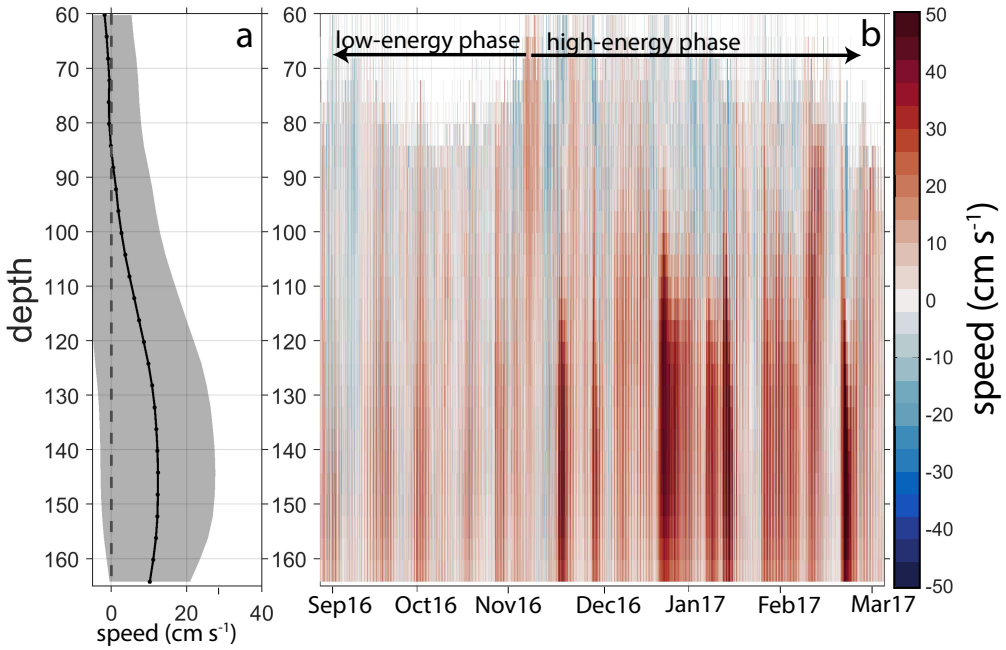

Figure 3.4: Moored current measurements in Dijmphna Sund. a, mean flow speed in the prevailing flow direction averaged for each depth (black dots) with the respective standard deviation (gray shading). **b,** speed time series rotated into the prevailing flow direction in each depth interval for a time period from end of August 2016 until March 2017. The low- and high-energy phases are marked by arrows (see text)

mean velocity in the mAIW layer reaches 8.6 ± 15 cm s^{-1}. The large standard deviation (>200%) indicates a large variability of the flow which is discussed in detail in the following section.

3.2 Temporal variability of currents in the mAIW layer

The current time series obtained from the upward looking ADCP at the mouth of Dijmphna Sund is visualized in Figure 3.4b. At first sight, one can divide the time series into a period of low and one of high energy. From September to mid November, flow speeds alternate slightly around zero. In contrast, from November to March, one observes events of enhanced current speed lasting for 5–10 days. Those events are strongest below 120 m depth, but are observed occasionally up to 100 m depth.

As most of the variability appears simultaneously in all depth bins (Fig. 3.4 b), a detailed analysis was restricted representatively to the depth of the strongest flow. To separate variability at different time scales, the time series was filtered following *von Appen et al.* (2016). Period limits of 30 days, 2 days, and 0.25 days separate the intra-annual variability (T>30 days) from a monthly component (2-30 days, see Fig. 3.5). The daily to sub-daily range contains al periods between 0.25 and 2 days and all variability with periods smaller than 0.25 days was considered to be high frequency variability. Those limits were chosen to separate a trend and seasonal variations (T> 30 days), from mesocale variability including eddies (T=2-30 days). A lower limit of 2 days, made sure that tides and inertial oscillations (T=2-0.25) were removed from the monthly variability. The high-frequency limit was chosen to exclude high-frequency noise from the analysis.
In addition, a spectral estimate was calculated (Fig. 3.6). Since the record had a total length of 191 days and was sampled at a rate of 1 hour, it can resolve time periods that lay between 191 days (fundamental frequency) and 30 min (Nyquist frequency). A rotary pairing was chosen for display (see section 2.3) because it displayed more anisotropy than the Cartesian pairing. As typical for a spectrum of ocean currents, most energy is located at the lower frequencies (Fig. 3.6). The power density starts to decrease at a period of approximately 30 days. Distinct peaks are found in the daily to sub-daily range.

Intra-annual variability

The intra-annual variability accounts for 14% of the total variance of the time series (see equation 2.22, 3.6) and underlies the differentiation into a low and high energy phase (Fig. 3.5 a). Speeds vary around a mean of 7 cm s^{-1} from September until mid of November. The second period has a mean of 17 cm s^{-1} and is characterized by a two step transition to the flow speed maximum in late December, until it levels out. When comparing the calm and high-energy period in frequency domain, the largest deviations are located in the low frequencies up to a period of 10 days. Consequently, the change between the two phases is related to processes with time scales longer than 10 days.

Monthly variability

The monthly component unites 29% of the variability and shapes all of the pronounced peaks starting from mid of November (Fig. 3.5 a,c). The shape of those peaks is rather asymmetric, with a sharp increase. The spectral estimate does not provide any information on dominant periods in this range. Counting the pronounced peaks occurring every 5-20 days, leads to an average period of 10–11 days for the whole time series. This period agrees

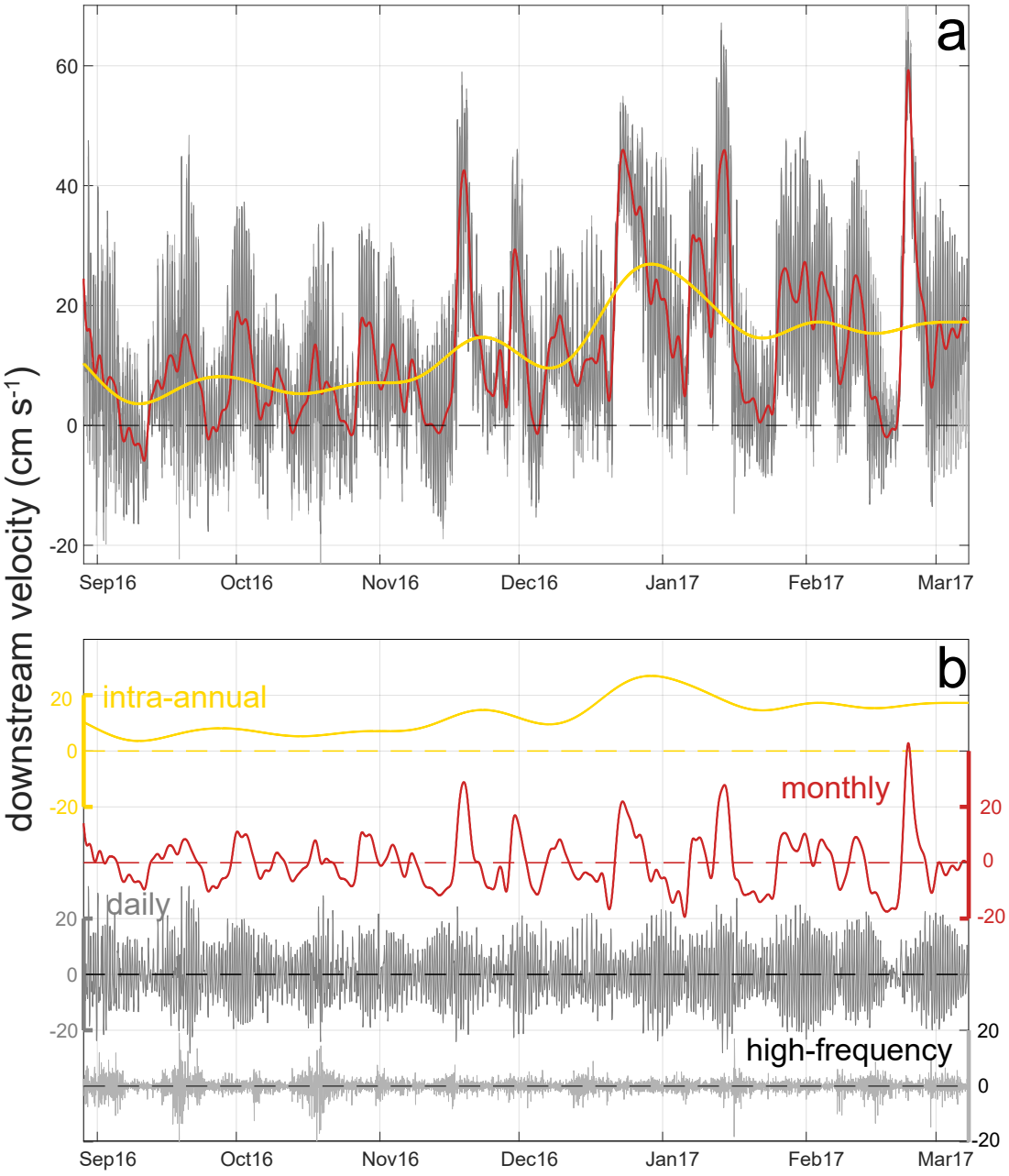

Figure 3.5: Current time series rotated in the prevailing flow direction at 144 m depth. The signal was bandpass filtered in intra-annual (T>30 days), monthly (T=2-30 days), sub-daily to daily (T=0.25-2 days) and high-frequency variability (T<0.25 days). **a,** the different bandpass filtered signals are stacked to display the measured time series. **b,** the different components are displayed separately.

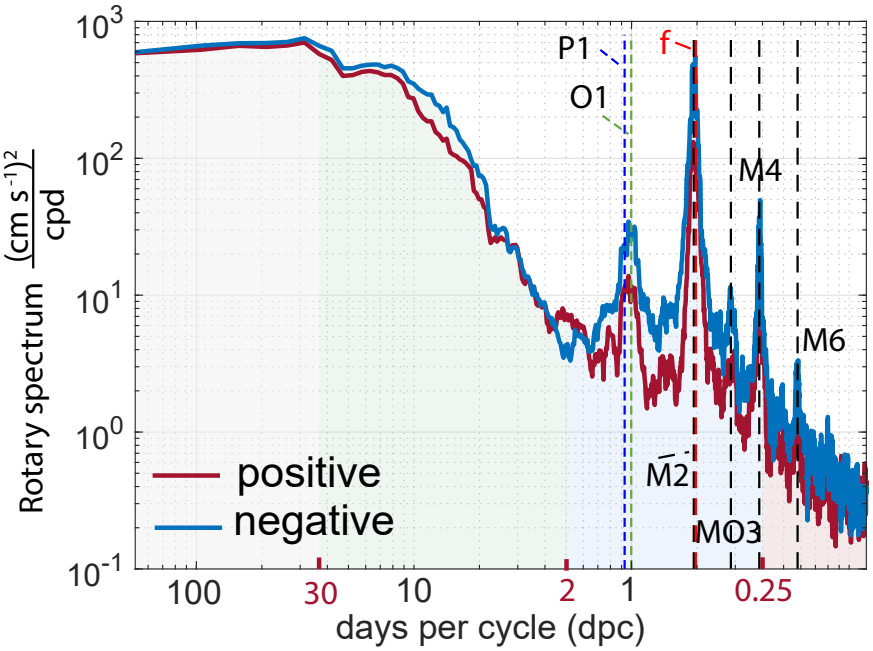

Figure 3.6: Rotary spectrum of the largest downstream component. Tidal periods are displayed as dotted lines and named. The Coriolis frequency f has a period of T=0.5080 days per cycle. The spectrum was divided into four parts (intra-annual, monthly, sub-daily to daily and high frequency), that are shaded in different colors. The limits of the different parts are marked in red on the x-axis.

well with the time scales estimated above for processes leading to the shift between the low- and high-energy phase.

Daily to sub-daily variability

Daily to sub-daily variability accounts for more than half of the variance (53%). In this range, the negative component of the rotary spectrum outweighs the positive one, most pronounced at the inertial frequency f that almost coincides with the diurnal tides (f=1.9686 cpd, M2=1.9323), indicating the presence of near-inertial motions rotating clockwise (Fig. 3.6). The near-inertial motions have been generated by winds and maintained by a balance between Coriolis and centrifugal acceleration, but they decay rapidly within a few cycles (*Pugh and Woodworth*, 2014; *Stramska et al.*, 2016). Furthermore, the appearance of the spectral estimate is dominated by pronounced peaks at frequencies associated with astronomically forced tides. The strongest signal is visible at the frequencies of the semi-diurnal tides (Fig. 3.6). This is confirmed by the the filtered time series that is characterized by a fairly regular semi-diurnal tidal cycle (Fig. 4.4). Except of the spring-neap cycle caused by interference phenomena, there is no obvious change in amplitude over the time.
Spectral estimates were compared for all depths and it was concluded that tidal currents are mostly barotropic. The spectral estimate of the strongest flow reveals peaks at the diurnal and semi-diurnal tidal frequencies, as well as several shallow water components as MS_f and higher harmonics of the basic tidal frequencies like M4 and M8. Shallow water tides arise when tidal currents (e.g., associated with M2 and S2) are modified by bottom friction and other physical processes that depend on higher powers of the tidal amplitude.

This results in constituents with angular speeds of multiples, sums or differences of the original speeds (e.g., MS_f) with a frequency equal to the difference between the interacting components ($f = 2(\omega_{M2} - \omega_{S2})$). Similarly, the fourth-diurnal tide M4 is the first harmonic of M2 (*Pugh and Woodworth*, 2014). The shallow water depth at the Dijmphna Sund sill (170 m) and the headland of the southern coastline favor the origin of higher tidal harmonics and explain the high abundance of shallow water tides (*Pugh and Woodworth*, 2014, p. 135).

A second approach for tidal analysis was performed using classical harmonic analysis, which is implemented in the Matlab routine t-tide (*Pawlowicz et al.*, 2002). Since harmonic analysis fits amplitude and phase to predetermined (i.e., tidal) frequencies, its results may differ from the one of the spectral estimate that is limited to frequencies which are multiples of the fundamental frequency ($f_1 = \frac{1}{T}$) (*Pawlowicz et al.*, 2002; **?**, p.392). Calculations were performed on the complex current series and on the northward and westward component separately. Also, the temporal evolution of the tides was examined by taking only short sections of the total time series.

A common result of all runs is the frequent occurrence of S_{SA}, M_2 and MS_f. S_{SA} is a solar semi-annual tide, that is often strongly enhanced by seasonal climate variations and may be obscured by its radiational counterpart whose origin is no longer related to gravitational forcing, but to the climatic variations of temperature and pressure (*Pugh and Woodworth*, 2014, p. 65, 122). Its tidal ellipse is orientated southeast, parallel to the mean flow. Since the current record at M1 lasts only 191 days, there may be only one full period of SSA (T=182.5 days) recorded in the data. Consequently, it is possible that this estimate also contain biased low-frequency events which are unrelated to tides. M_2 is the main semi-diurnal tide, associated with the mean motion of the Moon. Overall, it is orientated parallel to the coastline (west-east), but an analysis of monthly parts revealed that it changes orientation from west-east during September and October to southeast in November until March. MS_f is a fortnightly shallow-water tide whose period (T=14.77 days) is the same as the spring-neap modulations (*Pugh and Woodworth*, 2014). It is orientated like S_{SA} towards the southeast. Comparing the results of the spectral estimate to the results from t-tide, reveals a bias of the results from t-tide to longer frequency tides. Neither the frequency of S_{SA} nor the one of MS_f are associated with particularly pronounced peaks in the spectrum.

The relative importance of the most significant tidal components calculated with t-tide and their orientation is displayed in Fig. 3.7a. Tidal currents are depicted as current ellipses, describing the line that is traced by the tip of the current vector during one tidal cycle. Its inclination gives the angle between the direction of the maximum tidal flow and true East.

Overall, 20% of the total variance is accounted to the predicted constituents by t-tide. Taking into account that it is possible to identify even more tidal peaks than suggested by t-tide, this result is probably underestimating the relevance of tides. The amplitudes of the tidal currents (S_{SA}=7.7 cm s^{-1}, M_2=6.0 cm s^{-1}, MS_f=4.0 cm s^{-1}) reach up to 60% of the mean flow of 12.4 cm s^{-1} and may be relevant when the ambient flow directed out of the fjord is weak. As one of the striking questions is whether Dijmphna Sund may temporarily experience inflow, a detailed analysis of the flow direction is laid out below.

High-frequency band

The high-frequency variability accounts for the least variance (4%). In the spectral estimate (Fig. 3.6), a few peaks of this frequency range may be still associated with sub-diurnal tides (e.g. M8). The filtered time series shows irregular occurring events with larger amplitudes mainly during autumn (Fig. 3.5). Such high frequency variability may be caused by ocean

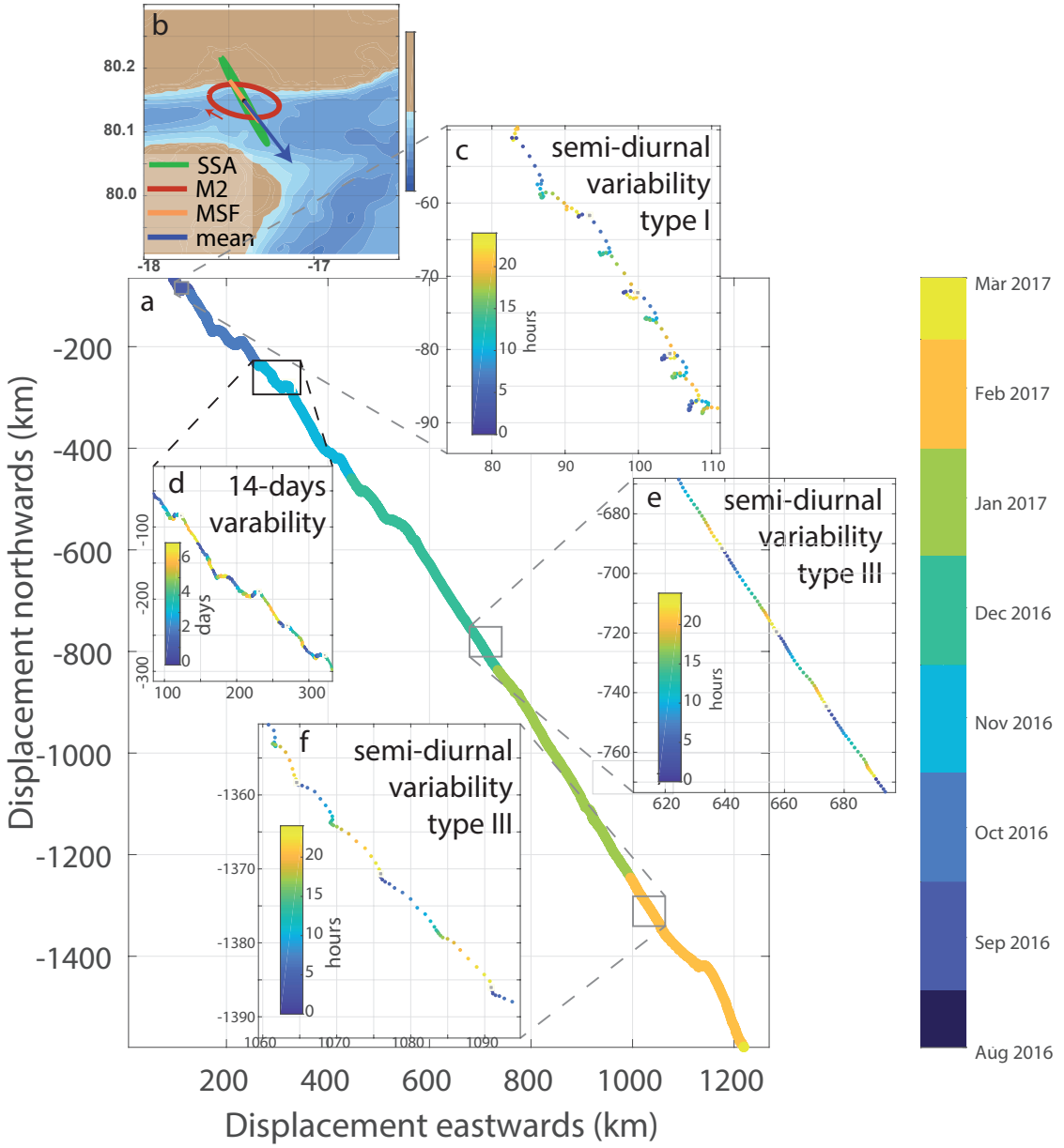

Figure 3.7: Flow direction in Dijmphna Sund a, Progressive vector diagram of the total time series of the flow indicates a flow to the southeast. **b,** Tidal ellipses at Dijmphna Sund and mean flow direction (see 3.3 for a larger version), **c,e,f**, Close-ups of the progressive vector diagram, the color-coded indicates the hour. The flow direction and speed varies on a semi-diurnal period with varying characteristics (type I-III). **d**, Fortnightly variability in flow direction, the color-code indicates days.

phenomena (e.g. small scale turbulences), but also by random contributions from the instrument sensors, i.e. noise.

Variability of the flow direction

Even though variability of the flow direction is indirectly included in the analysis of the flow magnitude in downstream direction, this section aims to point out some patterns of the flow direction in detail. In general, variability in the flow direction is low, but it exhibits some interesting features (Figure 3.7). The progressive vector diagram shows a constant main flow direction to the southeast. In regular intervals of 14 days, one observes periods of 3-4 days with weak flow towards the northwest, almost perpendicular to the main flow direction. Additionally, on a daily base, there is a full anticyclonic rotation of the current direction that is orientated west-east. While velocities are increased (larger spacing of points) when the circular flow directs to the mean flow direction, they are strongly reduced when directed to the opposite direction. This results in 4 hours of strong flow to the southeast and 8 hours of a weak clockwise turning flow directed rather into the fjord. Due to their 12 hours cycle and almost constant magnitude, those movements are associated with the semi-diurnal tides. The orientation of the current ellipses (mainly north-south) matches with the results of t-tide that suggested a M2 tidal ellipse aligned West-East. Also, it is possible that the fortnightly variability is associated with the spring-neap cycle. Those regular patterns of direction changes are not persistent with time, but change according to the intra-annual variability. From August to mid of November tidal ellipses, orientated mainly west-east, are recorded, superimposed on a strong mean flow directed to the southeast (phase I). Flow at depths below 140 m into the fjord is small. From mid of November until mid of January (with interruptions), tidal currents orientated westward are suppressed. Tidal cycles are only present in a variation of the current velocity pointing into the main flow direction (phase II). A third phase occurs from mid of January until beginning of March that appears to be half way both extremes of phase I and phase II. A tidal ellipse is hinted, but not completed.

In brief, most energy in the observed current variability is found at mainly two different frequency bands. Variability in the sub-daily to daily range accounts for 53% of the total variance and is associated with tides. Intra-annual and monthly variability (in total 43%) show both an increase in intensity from November onwards. Monthly variability varies (irregularly) at periods of approx. 10 days, which is a period associated with synoptic time scales. The next section investigates possible links between the variability in the current speeds and two potential driving mechanisms operating at those time scales.

3.3 Potential forcing of the circulation in Dijmphna Sund

Monthly variability on synoptic time scales (T=10 days) suggests that processes with similar periods may be responsible for the observed peaks. Therefore, two parameters changing on such time scales were analyzed: first, local wind and second, the sea ice concentration. Meteorological measurements were taken from an island called Henrik Krøyer Holme in Westwind Trough about 90 km northeastward of the mooring location. Additional reanalysis wind data with a resolution of 55 km from *Kobayashi et al.* (2015) complement the weather observations that suffers a lack of data in winter. Sea ice concentration data from passive microwave remote sensing is provided in a resolution of 3.125 km and was available for the whole region (for details on data sets see section 2.2). Sea ice concentration in Dijmphna Sund was averaged for a 10×10 km large area centered around the mooring location and plotted versus the outflow velocity.

The wind data recorded at Henrik Krøyer Holme shows a seasonal cycle, with increased wind speeds and a higher variability in winter and calmer periods in summer (Figure 3.8 b). In the winter 2016/2017 the weather station recorded several storm events with wind speeds of up to 30 cm s^{-1} blowing towards the south (Figure 3.8 a,b). The reanalysis data resemble only partly the observational data and are not able to reflect the strong wind events. Due to the sparse data availability, it is not possible to establish an event based relation between wind and currents, but winds increase at the same time in the year as the currents do.

Besides, sea ice concentration may influence the ocean state either by brine rejection during sea ice formation increasing or dampening the wind stress onto the ocean (Figure 3.8b). Sea ice coverage in Dijmphna Sund reached 100% in October 2016. From mid of December, the sea ice broke repeatedly apart and was subsequently reduced down to 85%. From March onwards, the sea ice cover stabilized again to 100%. As those changes occur at the same time of the year like the increases in velocity, the possibility of a relation was considered. Correlation coefficients were calculated between sea ice concentration at each location and the current velocity. At the mooring location itself, there is a weak anti-correlation of R=-0.33 (significant at 91% confidence interval). Remarkably, significant weak anti-correlations are observed as well in all areas that are located south or southeast of the shore (see Fig. 3.8c).

In sum, analyzing wind data for Dijmphna Sund is rather difficult as the data availability is poor. Nevertheless, it became clear that there are stronger and more variable winds in winter in Westwind Trough. Further, one could establish a weak connection between reduced sea ice concentration and increased current speeds, that will be discussed in the next section.

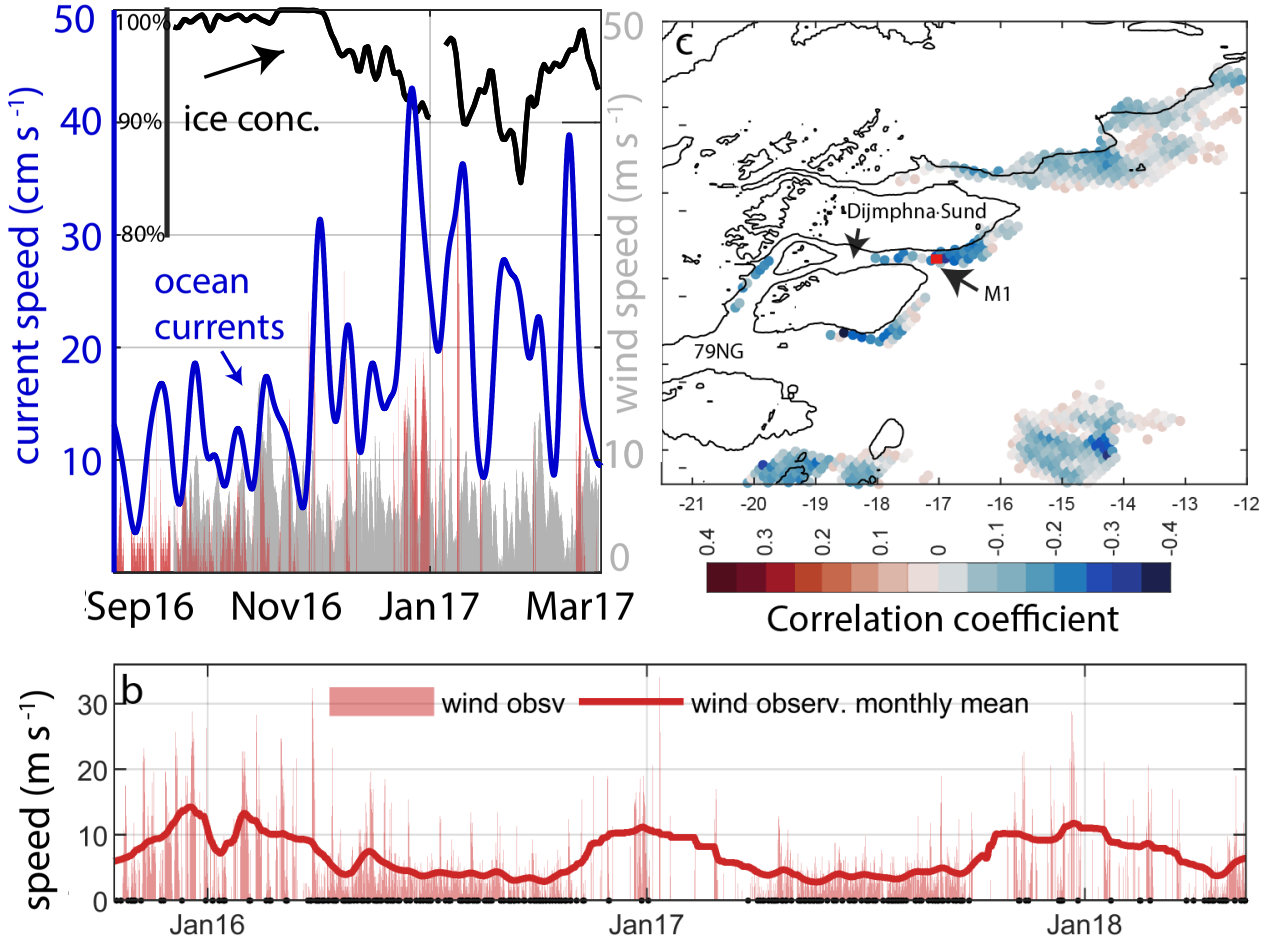

Figure 3.8: Comparison of current velocities, wind speed and sea ice concentration. **a,** sea ice concentration in black, ocean currents (blue line), absolute wind speed from reanalysis data (gray bars) and absolute speed from a weather station at Henrik Kroeyer Holme (red bars). Black dots indicate where wind speeds are below $3\,\mathrm{cm\,s^{-1}}$ to separate them from the times where no observations are available. **b,** 2.5-year long time series of absolute wind speeds at Henrik Kroeyer Holme (monthly mean is given by a thick line). **c,** significant correlations between sea ice concentration (at the respective location) and the ocean speeds at M1.

3.4 Discussion

The analysis of the seven month long current record from the mouth of Dijmphna Sund confirmed the assumption of earlier studies that the fjord is an export pathway of glacially modified waters (*Schaffer*, 2017; *Wilson and Straneo*, 2015). Beyond that, the analysis revealed some new aspects. First, except for a weak inflow associated with tides currents were directed out of the fjord. Consequently, Dijmphna Sund is permanently an export pathway, with mean current velocities outnumbering the earlier estimates by a factor of 40 (*Wilson and Straneo*, 2015). Since water properties at depth are associated with glacially modified waters, one can conclude that the currents at Dijmphna Sund are at least partly related to the buoyancy driven circulation (glacier-induced, see e.g. *Straneo and Cenedese*, 2015) that provides the continuous stream of mAIW in the west. Unlike other fjords where this circulation is two-dimensional or due to rotation slightly three-dimensional at the fjord's mouth, export of mAIW at Dijmphna Sund is spatially decoupled from the inflow of AIW to the glacier. Chapter 4 will analyze how the Dijmphna Sund branch is linked to the subglacial cavity circulation. In this context, the observed warming of the mAIW layer of 0.5 °C might have had consequences for the heat flux within the cavity. Calibration of the sensor prior to deployment and after the recovery rule out a sensor drift, and as shown in 4, this signal was recorded at the main calving front as well.

A characteristic feature of the time series is its variability of up to 30 cm s^{-1} a day (daily means) that is distributed over different frequency bands. Half of this variability is associated with tidal currents that have a magnitude of 4 cm s^{-1} (M2). That matches well with the findings of *Topp and Johnson* (1997) that described a M2 component of 3-5 cm s^{-1} in Westwind Trough. The channel geometry and the shallow water depths could be responsible for the enhanced tidal currents and the presence of shallow-water tides (*Pugh and Woodworth*, 2014). During times of complete sea ice coverage, the importance of tidal currents in the cavity circulation increases, because they provide a source of kinetic energy for conversion to vertical mixing (*Mueller et al.*, 2012). This kinetic energy is a crucial element to sustain the thermohaline circulation. First, mixing is necessary to raise the warm water to the ice base against the stable stratification that is established when melting a near-horizontal ice shelf base. Second, a plume of mAIW rising along the ice base sustains its motion due to continuous melting despite the increase in freezing point, must extract heat from the ambient water by mixing (*Williams et al.*, 1998). Tides that increase the mixing may have a large influence on the basal melt rates, as it was recently predicted for the Filchner-Ronne Ice Shelf by *Makinson et al.* (2011). Besides an impact on the basal melt rate, tidal currents can drive an exchange flow between the cavity and the adjacent shelf as modeled for the southern Weddell Sea by (*Makinson and Nicholls*, 1999). In the Weddell Sea, tides are stronger by a factor of 10 than measured at Dijmphna Sund, but a study from Flade Isblink has demonstrated that tidal velocities low as 1-2 cm s^{-1} may already contribute to water renewal at the calving front and induce internal waves. Consequently, the effect of the tidal movements observed in Dijmphna Sund may contribute to the heat transport to the glacier.

Unlike tides, intra-annual and monthly variability that account together for 43% of the variability have a major impact on the export of freshwater to the Westwind Trough. The intra-annual variability ($>$ 30 days) indicate a low- and a high-energy phase, a trend that is picked up in the monthly variability (2-30 days) that exhibits irregularly occurring peaks with a mean period of 10 days that are enhanced from mid of November. I hypothesize that both might be at least partly associated with atmospheric conditions. The reason for this is twofold. First, the intra-annual current speeds increase at the same time in the year as the winds do. Second, there is a weak link between sea ice concentration and the

current strength at Dijmphna Sund that will be elaborated further in the following section. However, one needs to consider that the time series only covers half a year, i.e., is too short to establish a solid relation between seasonal variations in atmospheric conditions and the ocean currents.

Possible impact of winds and sea ice concentration on local circulation

Based on the correlation between sea ice concentration and current speeds at Dijmphna Sund, one rises the question whether sea ice influences the currents or whether both might get affected by the same forcing.
Sea ice cover reduction has been observed earlier in this region before (*Böhm et al.*, 1997; *Martin et al.*, 2014; *Schneider and Budéus*, 1997). *Böhm et al.* (1997) associated the decrease in sea ice concentration (below 90%) close to the Northeast Greenland coast in winter with the Northeast water polynya, first described as summer polynya by *Schneider and Budéus* (1995). Studies showed that in winter, during times of strong northerly winds, a latent heat (coastal) polynya with ice concentrations below 90% occurs (*Böhm et al.*, 1997; *Schneider and Budéus*, 1995, 1997). Repeated stormy outburst during winter from northwest direction push newly formed sea-ice out of the region that is sheltered from sea-ice import by the coast and ice barriers (*Schneider and Budéus*, 1997). The fact that all areas located south/southeast of the shore exhibit a similar significant anti-correlation with the current speed ($R<-0.3$) strengthen the point that northerly winds blowing over the coast lead to a reduction in sea ice concentration.

A winter polynya may influence a fjord's stratification significantly by brine injection (e.g. *Cottier et al.*, 2010). Since sea ice concentrations drop repeatedly during the winter below 90%, one should consider whether sea ice formation affects the local currents. As shown by *Boone et al.* (2017) and *Dmitrenko et al.* (2015) for the Young Sound- Tyrolerfjord system (74°, NE Greenland) a winter polynya at a sill can lead to brine-induced gravity plumes and subsequent enhanced current speeds. However, the situation in Dijmphna Sund differs with respect to sea ice concentration, water depth and general circulation pattern. The polynya described by *Dmitrenko et al.* (2015) is characterized by sea ice concentrations of 40-60%, is located over a sill that has a depth of 40 m, and the circulation is characterized by inflow to the fjord at depth and outflow at the surface. Since the temperature and salinity record at the bottom shows no signs of occasional cold brine-enriched waters, a direct influence of the reduced sea ice concentration of 85-90% at Dijmphna Sund onto the bottom-intensified currents seems unlikely.

A second possibility to explain the correlation between sea ice cover and ocean circulation are changes in the wind forcing that affects both.
As stated above the Northeast water winter polynya is maintained by northerly winds that were present during the winter 2016/2017. The effects of wind forcing on fjord circulation are manifold, but a closed sea ice cover can reduce the influence significantly (e.g. *Cottier et al.*, 2010). In contrast, broken sea ice coverage even increases the momentum transfer to the ocean due to its great rigidity. *Martin et al.* (2014) found an optimal sea ice concentration of 80-90% for momentum transfer to the ocean, a concentration that was reached for 18 days at Dijmphna Sund between end of September and March. Consequently, wind forcing affects most likely the fjord circulation in winter. A recent example of wind-forcing on the heavily sea ice covered continental shelf close to Flade Isblink, Northeast Greenland, was given by *Kirillov et al.* (2017). They showed that a northerly storm event gave rise to down-welling dynamics associated with on-shore Ekman transport in the upper 40 m of the water column and and a compensating off-shore flow at intermediate depths (40-66 m and probably deeper *Kirillov et al.*, 2017). Data quality restrained the depth range

with reliable data to the upper 66 m of the water column. As the winds ceased, the flow reversed. This is an example of the so called intermediary circulation that is driven by pressure gradients between the fjord and the continental shelf and was described in other Greenland's fjords before (e.g. *Jackson et al.*, 2014; *Straneo and Cenedese*, 2015; *Straneo et al.*, 2010; *Sutherland et al.*, 2014b). The gradients can be formed by any forcing, but are often associated with along-shore (i.e. here northerly) winds that pile up water and depress the halocline at the fjord's mouth (*Jackson et al.*, 2014; *Straneo et al.*, 2010). This leads to an inflow in the upper layer and an outflow at depth, resulting in a depressed halocline in the fjord (*Klinck et al.*, 1981). As the winds calm down and the outer shelf returns to the pre-event state, the circulation reverses (*Straneo et al.*, 2010). Those pulses are associated with strongly sheared, fast flows that reverse in depth and time with a typical duration of 4-10 days (*Jackson et al.*, 2014). The current time series at Dijmphna Sund shows indeed periods of strong velocity increases at depth followed by very low velocities. However, the currents at the recorded depths are barotrop and surface velocities were not covered by the ADCP. Those could help to establish a reliably relationship between the wind influence and the ocean currents.
To sum up, the anti-correlation between sea ice concentration and currents point to wind-forcing. Initially, northerly winds may reduce the sea ice coverage to 80-90% at Dijmphna Sund. Further wind stress will then be transfered to the ocean surface to an larger extent. I speculate that storms may then induce downwelling favorable conditions at the fjord mouth. A compensating undercurrent may enhance flow velocities in the deeper layers of Dijmphna Sund.

Consequently, an impact of regional winds onto the circulation is likely, and has been observed elsewhere before (e.g., Pine Island Bay *Webber et al.*, 2017), but cannot fully explain the observed oceanic variability. Since Dijmphna Sund is all year round a part of the buoyancy driven, glacial circulation, it appears inevitable to discuss the variability described in this chapter in the context of the overall glacial circulation. Consequently, the next chapter will focus on the role of Dijmphna Sund in the cavity circulation of the 79NG.

4 Influence of the cavity circulation on the variability in mAIW export through Dijmphna Sund

The preceding chapter elaborated that the mean currents at Dijmphna Sund must be strongly linked to the cavity circulation. Since winds and sea ice concentration could not yet explain the observed variability in the outflow, Dijmphna Sund is now set into the context of the cavity circulation. Guided by research question 2 (Section 1.4), this chapter aims to find evidence of further drivers of the current variability influencing the glacier-ocean interactions by exterminating similarities and differences between flow into the glacier cavity (inflow) and out of the cavity (outflow).
The following chapter is laid out as follows: Section 4.1 describes the regional water masses and circulation pattern at the main calving front. The temporal variability of the circulation is characterized in Section 4.2. Spatial relationships between the gateways were established using transport calculations in Section 4.3 and Section 4.4. Eventually, the influence of the glacier onto the circulation, as well as the link to the shelf circulation is analyzed in Section 4.5 and discussed in Section 4.6.

4.1 Regional water masses and circulation at the 79NG calving front

4.1.1 Hydrography near the 79NG calving front

In the 79NG bay, three water masses are present (see Section 1.3 for details). Warm (>0.7 °C) and dense (> 27.75 kg m^{-3}) AIW occupies the depths below 240-300 m and is overlaid by mAIW that has been formed through mixing of AIW with glacial melt water. From approximately the glacier draft (90-100 m) to the surface, Polar Water (PW) is present that is characterized by temperatures at the freezing point. The following Section provides a short overview on the changes in mAIW and AIW as seen in the CTD casts 2016 and 2017, but does not intent to give a full description of the changes of the water masses.
As already observed at Dijmphna Sund (see Section 3.1.1) temperatures warmed and salinity increased during the observational period. At the main calving front, warming is observed in all water depths below the main thermocline at approximately 100 m depth (Fig. 4.1a). Consequently, PW remains unchanged, but mAIW and AIW show increased temperatures. Using the LADCP profiles from the inflow depression (location of mooring M2) indicates that inflow was present in 2016 between 310 m and 467 m and in 2017 between 250 m and 467 m. Those depths were used to define the interface between mAIW and AIW. As upper limit of the mAIW, 90 m (corresponding to the glacier draft) was taken. Using those limits to calculate mean temperature results in an increase of mAIW by 0.11°C from 0.41°C to 0.52°C. AIW warmed by 0.36°C from 0.81°C to 1.17°C. However, those values do not reflect the heat content of the flow as no weighting with the volume fluxes had been applied. The moored time series (Fig. 4.1b) indicates that the warming trend started mid of November. Comparing temperatures associated with inflow at M2 (427 m) and outflow at Dijmphna Sund (M2, 169 m) revealed a high correlation (R=0.78),

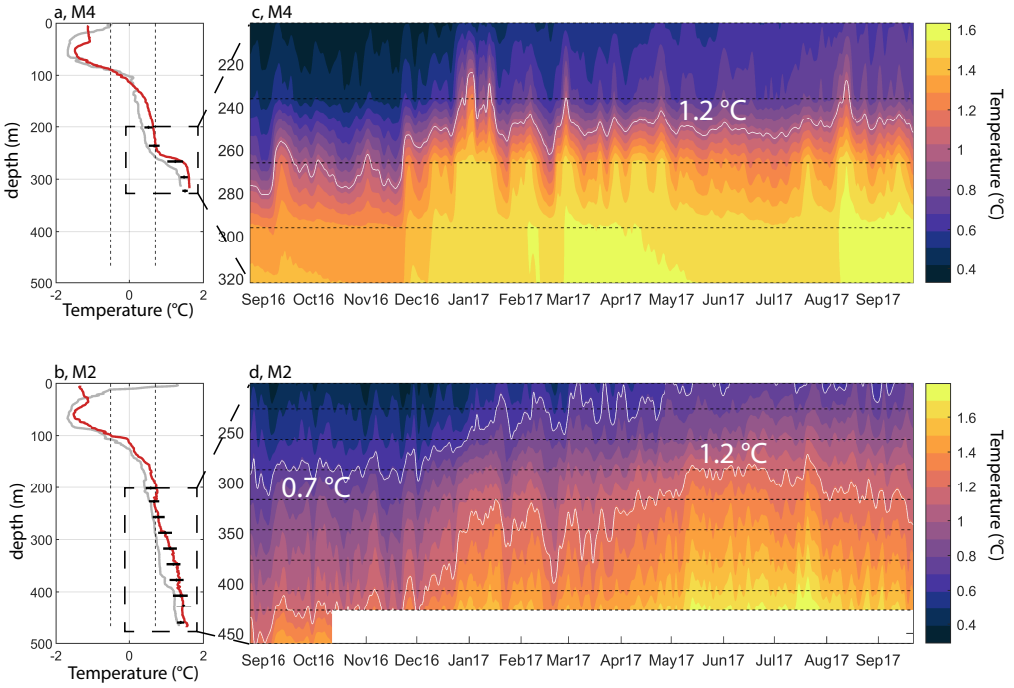

Figure 4.1: Temperature record at moorings M2 and M4 a,b, CTD profiles taken close to the moorings in 2016 (gray) and 2017 (red). The mean and standard deviation of the temperature measured by the moored instrument is given in black. **c,d,** Temperature time series from the moored instrument. The depth range is indicated on the CTD profiles in a,b. The 0.7°C and 1.2°C isotherms are given as white lines

that is increased to 0.79 when shifting the Dijmphna Sund time series backwards by 5.5 days. Similar results are obtained for all other temperature time series. This indicates that a large part of the temperature fluctuations at all sites occur (almost) simultaneously and are not advected through the glacial circulation.
The moored observations indicate that the 0.7°C isotherm that was used as proxy for the interface between mAIW and AIW was located on average at M2 at 203 m and at M4 at 207 m. Comparing its depth with the one at which the flow reverses will help to understand whether the AIW layer thickness increased or whether this interface was shifted to warmer temperatures (see Section 4.2).

4.1.2 Exchange flow across the glacial calving front

Flow exchange between fjord and glacial cavity takes place at four gateways (for details see Section 1.3.2 and Fig. 1.3). Time averaged flow profiles at those gateways rotated into the direction of the strongest flow are displayed in Figure 4.2 a-d. They are analyzed in the following from north to south.
At the main gateway for AIW entering the cavity (see Fig. 1.3), mooring M2 measured eastward flow (-27°) in the upper layer (100-243 m), and westward flow (176°) in the lower layer (243-436 m, see Fig. 4.2b). Maximal mean inflow speeds of 38 $\pm$ 12 cm s^{-1} are found at the lowest bin (436 m). An additional mechanical current meter placed at 457 m measuring similar velocities, indicates that inflow speeds are highest in the 25 m above the bottom at 463 m. The depth at which the flow reverses on average (243 m) is located deeper than the average of the 0.7°C isotherm (203 m) associated with the AIW/mAIW limit. Time averaged outflow speeds peak at 164 m with -3 $\pm$ 7 cm s^{-1} (Fig. 4.2b) and decrease to almost zero at about 100 m.

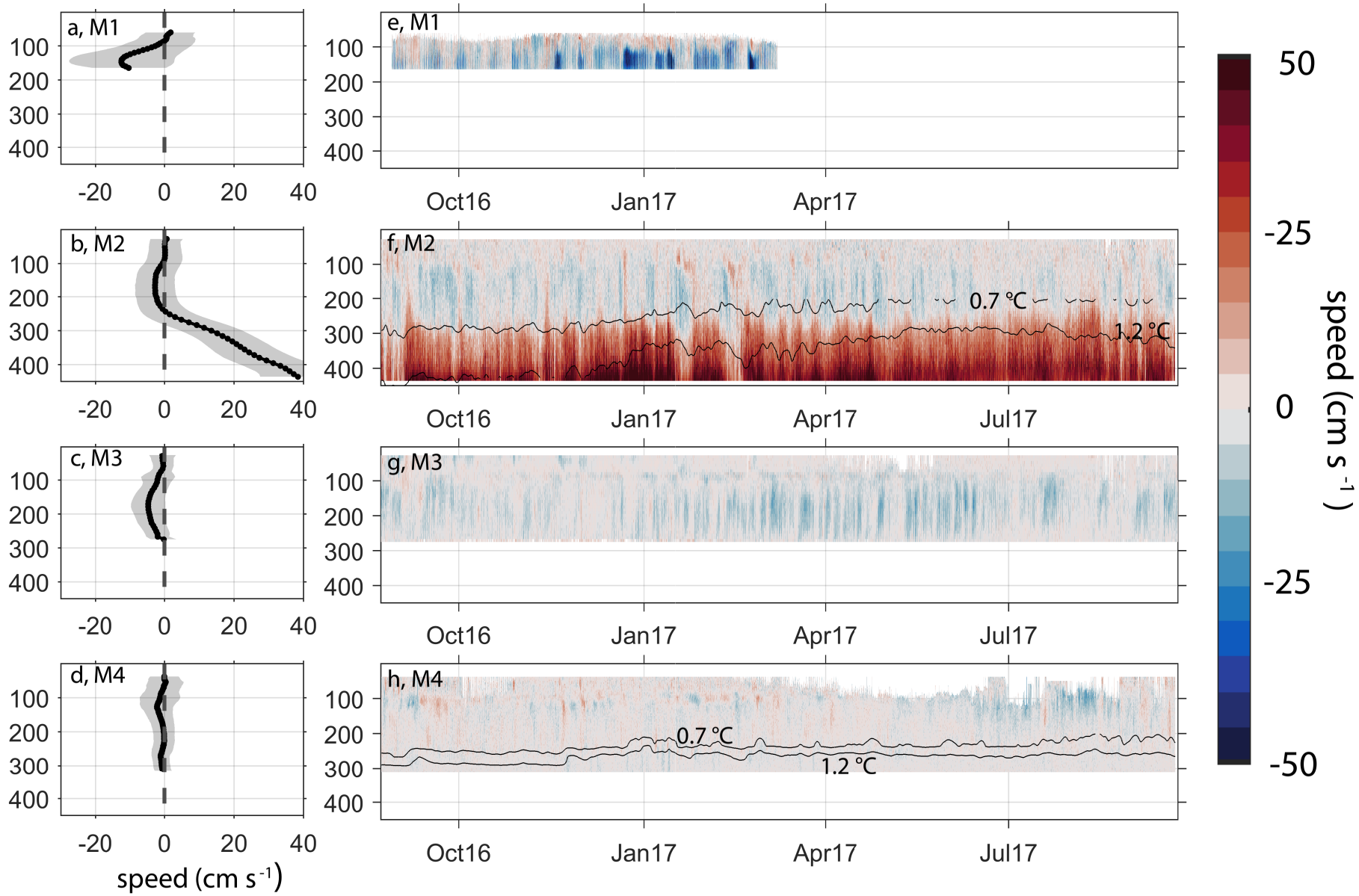

Figure 4.2: Rotated mean flow and time series at mooring M1-M4. a-d, mean flow speed in the prevailing flow direction averaged for each depth (black dots) with the respective standard deviation (gray shading). **e-h,** current time series of rotated speed into the prevailing flow direction in each depth interval for a time period from end of August 2016 until September 2017. The depth of the 0.7°and 1.2°isotherm is overlaid in M2 and M4 as black line.

South of M2, at the mid part of the main calving front (Fig. 1.3), the time series of mooring M3 indicates that the time averaged flow is directed towards the southeast (-56 °), and peaks at 179 m with a mean velocity of -5 ± 6 cm s^{-1} (Fig. 4.2). Velocities close to zero below 300 m and the absence of water denser than 27.8 kg m^3 (see Fig. 1.4) rule out this passage as a second pathway of AIW to the glacier cavity, but transport calculations indicated that 23% of the export of mAIW out of the 79NG cavity is taking place here.
The southern most mooring (M4) is characterized by very low velocities with a mean of -1 ± 5 cm s^{-1} (Fig. 4.2d). The flow is pointing towards the east (9°, Fig. 1.3), i.e. away from the calving front. The time averaged flow varies with depth between -0.35 cm s^{-1} (at 54 m) and 2.13 cm s^{-1} (at 126 m) and exhibits a second flow maximum of 1.1. cm s^{-1} at 270 m. Even though the channel may be deep enough to allow in- and outflow and CTD measurements indicate the presence of AIW below 207 m (average of the 0.7 °isotherm, see Fig. 4.1), the mooring recorded no significant exchange flow.
Comparing the bottom-intensified flow profile of Dijmphna Sund (speed maximum of -12.4 cm s^{-1}, Fig. 4.2a) with the ones from the main calving front, reveals clearly that Dijmphna Sund exhibits the strongest velocities directed away from the calving front. Weaker outflow with maximums of 2 to 4 cm s^{-1} in depths of 120-180 m is present at M2 and M3. At the southern most channel (M4), there is barely any flow observed.

4.2 Temporal variability of the cavity exchange flow

Figure 4.2e-h depicts the current time series at all depths. At M2 and M4, temperature loggers covering the water column provide sufficient high coverage to calculate the depth of the 0.7 °C isotherm that serves as an indicator for the interface between AIW and mAIW. Most striking feature of the M2 time series is the division in inflow (positive, bottom) and outflow (negative, top) and the temporal variability of this reversing point between 230-320 m (Figure 4.2e). Most changes of the flow appear barotrop at M2, i.e. increased outflow is often observed at the same time as decreased inflow (e.g. end of January, end of December), shifting the reversing point downwards and vice versa. Occasionally, one observes flow directed into the glacial cavity at all depths.
Below 240 m (average point of flow reversal), mean velocities are 20.1 ±16.3 cm s^{-1}, with fluctuations between zero and 70 cm s^{-1}. Fastest changes were observed end of January and February when velocity drops quickly (0.45 cm s^{-1} per hour) below 10 cm s^{-1} for a total duration of 4-10 days. Between 90-240 m, averaged velocities of this layer range between ±20 cm s^{-1}, with an average speed of -1.2 ±5.5 cm s^{-1}.
In 2016, the 0.7 °C isotherm was located at the same depth where the flow reverses, describing the interface between mAIW and AIW. When inflow happens over the whole water column, the 0.7 °C isotherm stays at constant depth, and subsequently, mAIW flows back into the glacial cavity at M2. From mid of November until January, the flow reversal point and the 0.7 °C isotherm increased together, pointing to an increase in speed and thickness of the AIW layer. However, from end of January onwards, the 0.7°C isotherm continues to rise while the flow reversal point returns to a deeper level, resulting in an outward directed flow of water masses with temperatures larger than 0.7 °. Consequently, mAIW leaving the cavity has warmed as well.
The mooring M3 differs from M1 and M2 by barotropic variability at higher frequencies (Fig. 4.2g). Increased outflow pulses last only 1-2 days, instead of 5-10 days as observed at Dijmphna Sund or at the inflow depression. The intensity of the variability increases between mid of March until mid of June, i.e. shifted by 2-3 months to the increase in variability observed at Dijmphna Sund. Reversed flow (inflow) is rarely observed at this gateway, but may occur occasionally in the upper 90-110 m.

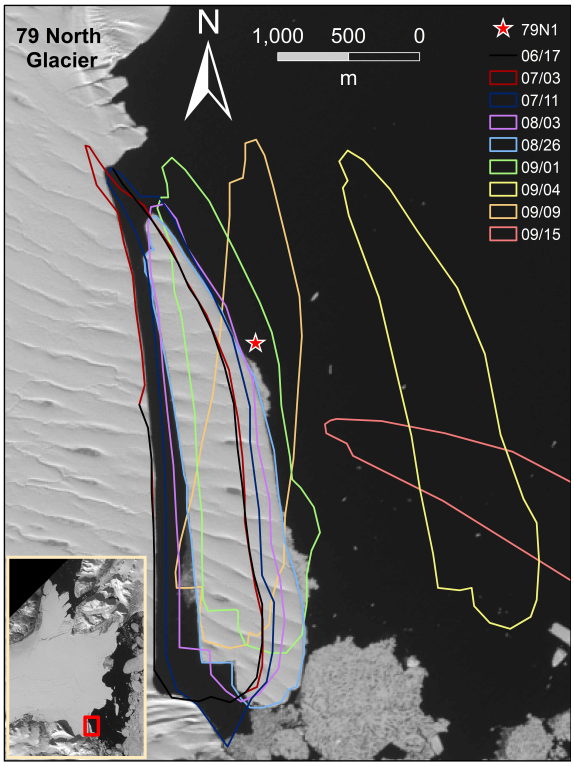

Figure 4.3: Iceberg overriding mooring M4. An iceberg calved between 2017/06/17 and 2017/07/03 and approached the mooring M4. The iceberg drifted first to the west, overrode the mooring for the first time (09/01), continued to drift to the northwest (09/04), was pushed backwards again (09/09) and eventually left the front to the southwest (09/15).

At the southern most mooring (M4), most variability is observed between 100-150 m (Fig. 4.2h). From June until August 2017, outflow velocities are strongly enhanced and may be associated with an calving event that took place between 2017/06/17 and 2017/07/03 (Fig. 4.3). The calved iceberg drifted towards the northeast, i.e. the direction of the mean flow indicated by M4 for the depths 50-300 m and turned backwards again (Fig. 4.3). On its way it overrode mooring M4 twice. The overpass of the iceberg is recorded from the 2017/07/20 to the 2017/09/11 in the echo amplitudes of the ADCP that rise to almost 100% in the upper 60 m. This event awakes the question what role the upper 90-150 m play in the glacier-ocean interactions, in particular in iceberg calving.

When compared to the records from the main calving front, currents at Dijmphna Sund (Fig. 4.2e) correspond best to the time series of the inflow depression. There is a match in amplitude, but also in intra-annual variability, as current speeds increase at both sites in winter. Single events, as the reduced inflow in end of January and February are present in both records, but lack at the southern gateways.
Those similarities will be studied in detail in the second part of this Section, and as most changes appear barotrop, the following Sections are restricted to the depth of the strongest flow. For mooring 79N2, two depths were chosen, the depth of the strongest inflow (436 m) and strongest outflow (164 m).

Variability at different time scales

Comparing the time series of the velocities at the depth of the strongest current speeds emphasis the similarities between Dijmphna Sund and the inflow at M2 (Fig. 4.4). Following the classification from chapter 3, the signal was filtered in intra-annual (T>30 days) and monthly variability (2-30 days, Fig. 4.4). No correlation was found on daily timescales and less (not shown).
The outflow at Dijmphna Sund and the inflow at the main calving front resemble each other most strongly at intra-annual time scales. Here, a common increase is observed in

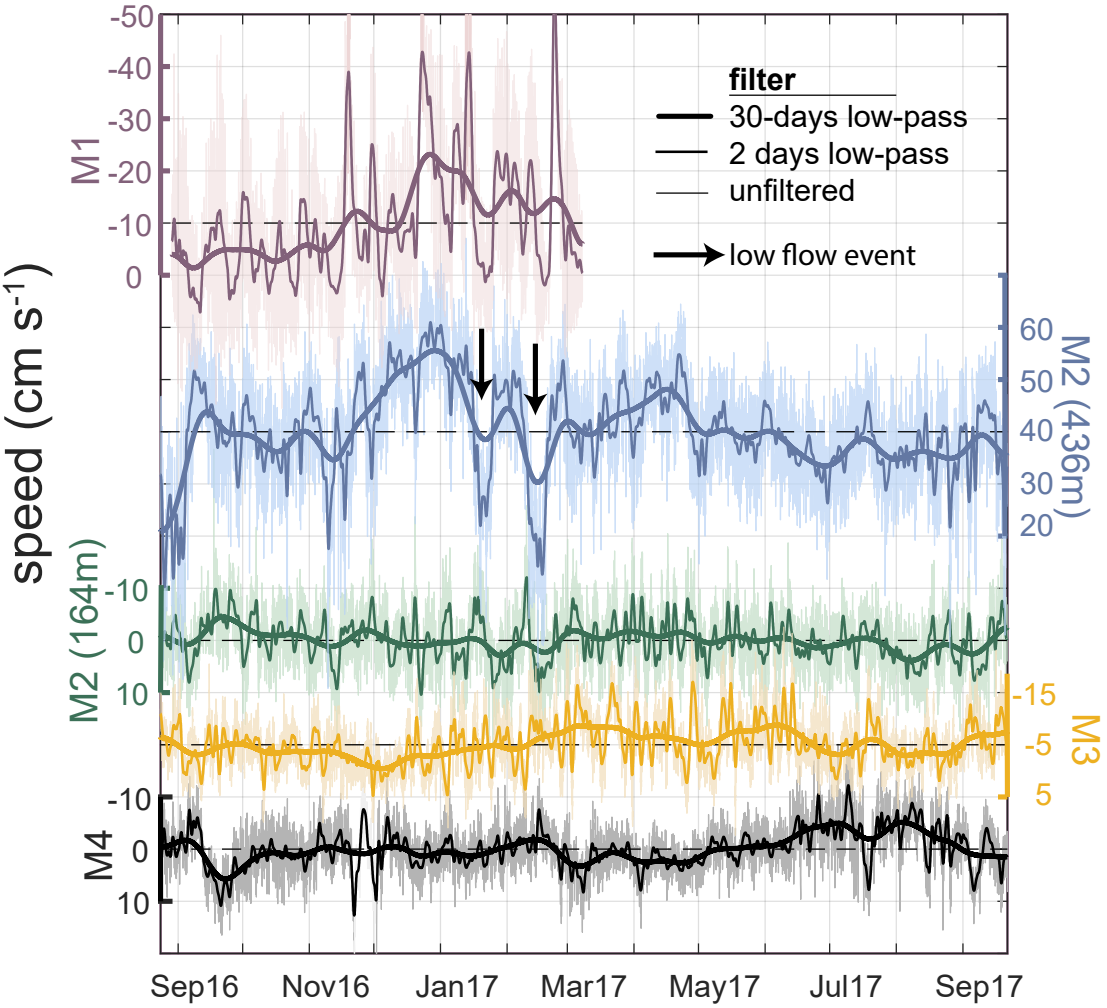

Figure 4.4: Filtered time series of rotated currents at M1-M4. Each time series was filtered with a low-pass filter with cutoff frequency of 30 days (thick dark line) and 2 days (thin dark line). The unfiltered data is displayed as thin, light lines. For means of better comparisons with the inflow at M2 (436 m), the y-axises of the export gateways (M1,M2 (164 m), M3, M4) were reversed.

November that happens gradually at M2, and in sequences of fast pulses at Dijmphna Sund. The maximum speed in January is followed in both series by two events of reduced speeds end of January and end of February that appear at M1 with a delay of 3 and 24 hours, respectively.
Both filtered time series have the same standard deviation ($6\,\mathrm{cm\,s^{-1}}$). Relative to the total variability present, the intra-annual variability explains 17% at Dijmphna Sund, and even 28% of the total variance of the currents. This discrepancy is explained by the fact that variability induced by tides play a minor role at the main glacier front compared to Dijmphna Sund as only 13% instead of 53% (at M1) of the variance is located in the daily to sub-daily range.

At time scales of 2-30 days, one cannot establish a clear relation between Dijmphna Sund and the inflow as some of the events are shared, but others lack an equivalent. Further, neither of the other three time series shares an obvious common variability with Dijmphna Sund or the inflow. Normalized cross-covariance functions confirmed that there is no significant correlation (with and without lag) between the velocity records.

Spectral estimates of the time series did not show any preferred periods in the low frequency range. Wavelet transforms were calculated to characterize the non-stationary variability. The wavelets (displayed for inflow and Dijmphna Sund, Fig. 4.5) show most intensity of the inflow is located at periods between 20-33 days. Here, three major events associated with low inflow velocities are most pronounced, appearing in September 2016, end of January and February 2017. They appear as stretched out horizontal bands, an appearance that tends to reflect waves rather than eddies that appear as vertically elongated features.
At Dijmphna Sund, the intensified features appear shifted into shorter periods of 10 days and their shape changed to triangular, i.e. more energy is located in higher frequencies than compared to the inflow features. Similar to the inflow, the intensity increases from November onwards. As already mentioned, and illustrated in Fig. 4.5, peaks in the daily to sub-daily range are more pronounced at Dijmphna Sund than at M2.
Consequently, the variability of the circulation does not have a fixed period and is better characterized by reoccurring events with periods in the range of 10-33 days. On long, intra-annual time scales, there is a good match between the two main branches of the circulation, but the lack of agreement with the other export gateways at M2, M3 and M4 is unexpected and needs further investigation. To establish a meaningful, spatial and temporal relationship between the different export gateways of the glacial circulation, estimates of the transport through the gateways are analyzed in the Sections 4.3 and 4.4.

4.3 Volume transport across the calving front

In the following Section, a brief description of the transport time series (J. Schaffer, personal communication, 2018, see Section 2.1.2 for details) is given, to prepare an analysis of the spatial connections using empirical orthogonal functions (EOFs, Section 4.4). Volume transport directed out of the cavity is marked by a negative sign (termed export), whereas volume transport into the cavity is defined positive (inflow).
The transports are essentially consistent with the mean flow pattern and indicate that most of the flow directed towards the glacier front takes place in the inflow depression below 240 m (89% of all inflow, Figure 4.6). Contributions to the inflow from other moorings, e.g. M4 (7%) are mainly from the upper water column (100-120 m). On average, most outward directed transport takes place at M1 (37%). At the main calving front, outward flow is distributed over M2 (28%), M3 (22%) and M4 (13%). The relative importance of the export pathways changes strongly with time. While M2 accounts always for at least

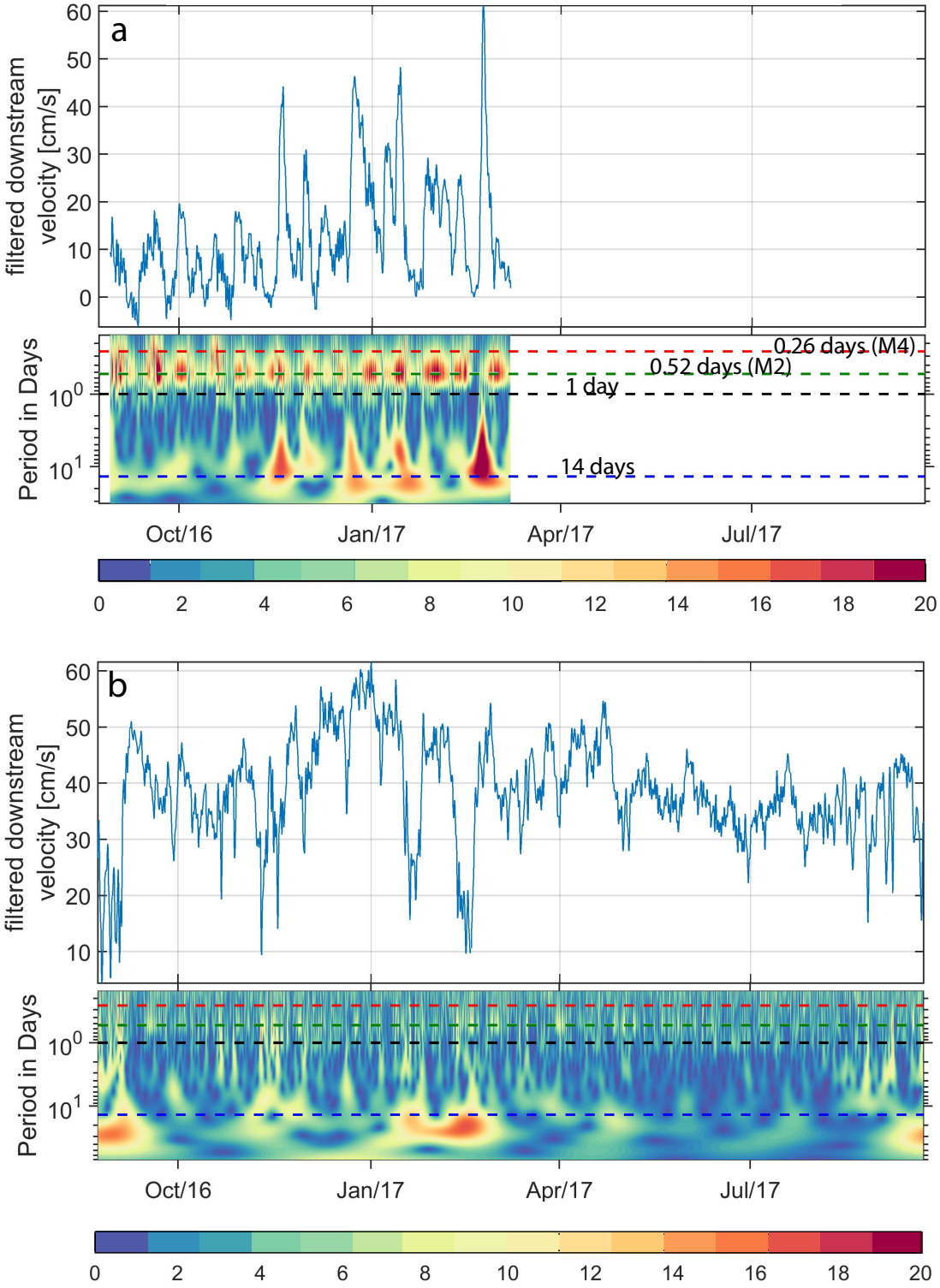

Figure 4.5: Wavelets of the downstream component at M1 and M2 (436 m). The downstream velocity (flow into the mean direction of the strongest flow) is shown together with the wavelet. Periods associated with different time scales are marked by horizontal dashed lines.

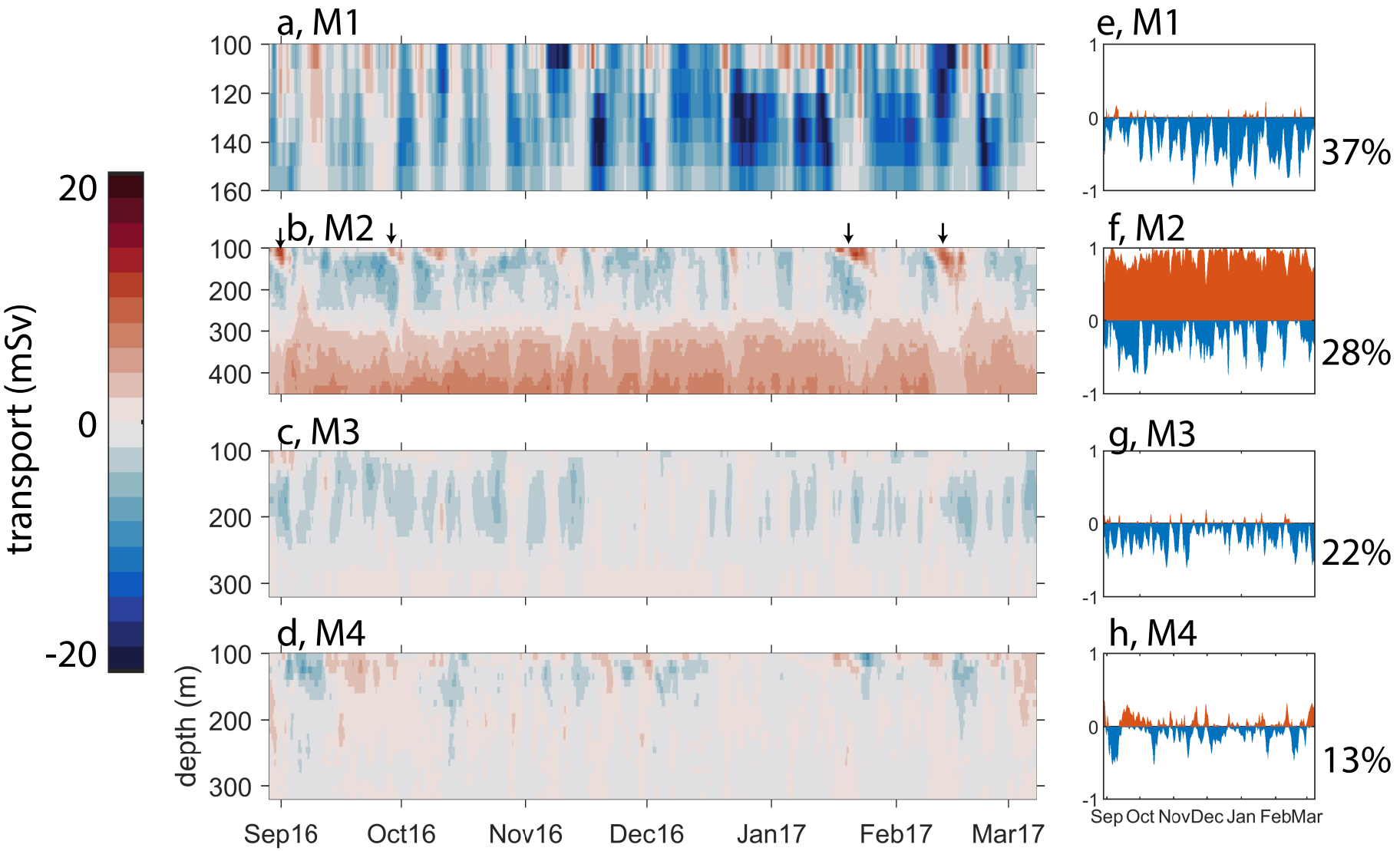

Figure 4.6: Transport at M1-M4 a-d, time series of volume transport per depth bin at M1-M4. Times in which there is at M2 a three-layer current system instead of the regular two layers are marked with arrows (observed at the 2016/08/31 (deployment of moorings), 2016/10/10, 2017/12/01, 2017/01/21 and, 2017/02/17) **e-h,** the relative contribution (fraction of 1) to the total inflow (red) and the total outflow (blue) underlines the different relevance of the gateways. The average contribution to outflow for each gateway is given in %.

50% of the inflow, the relative importance of e.g. Dijmphna Sund as export gateway varies strongly between 0 and 96%. At M1 and M2, not only the strength of the prevailing flow direction increased in winter, but also the one of the occasionally reversed flow between 100-140 m depth. At M2, this part of the water column plays an important role when the regular two layer flow is occasionally overridden by a three layer current system. At such events, inflow depths are reduced to 310 m, while outflow (120-310 m) is enhanced. At the same time, inflow takes place between 90-120 m that outweighs (per depth bin) even the inflow at the bottom.
The following Section will investigate such interactions between the gateways and the different depths systematically, using EOFs.

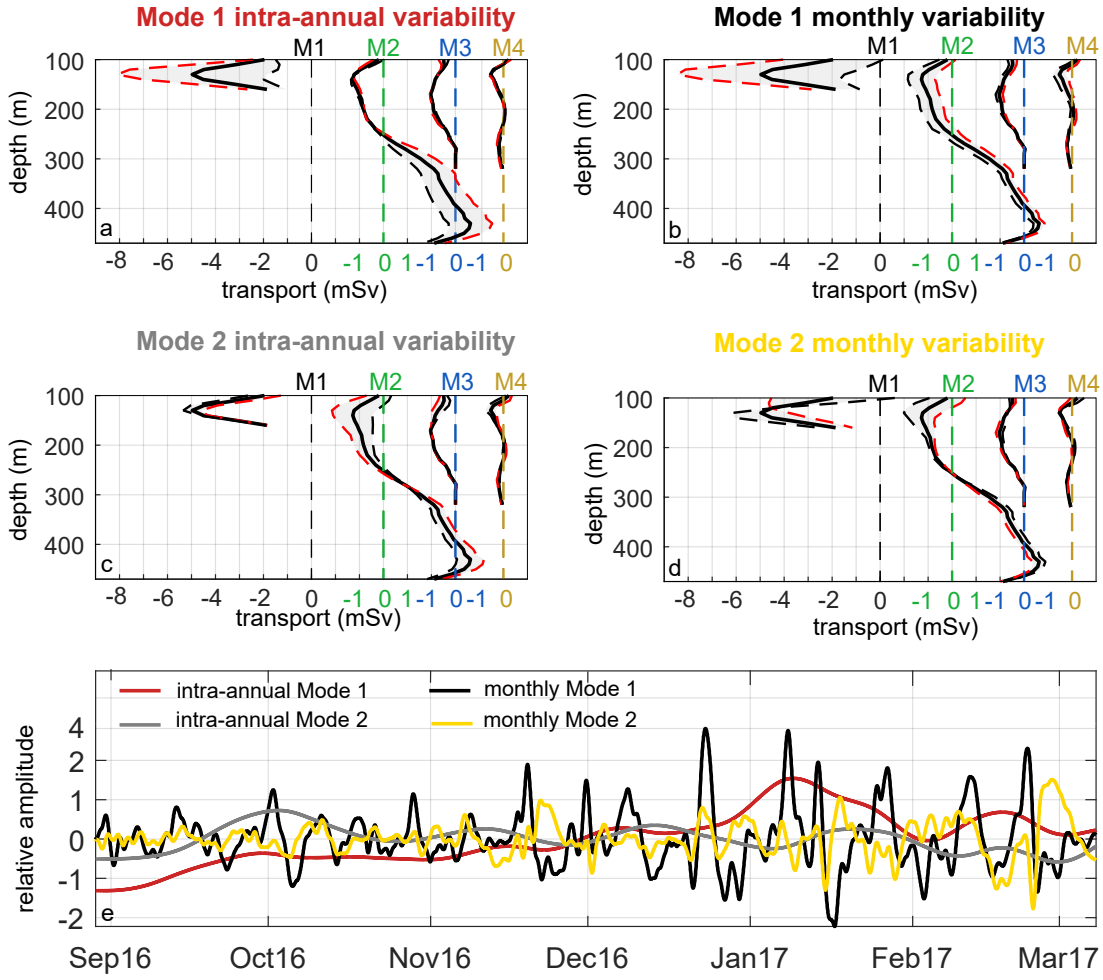

Figure 4.7: EOFs of filtered time series. a-d, mode 1 and 2 of the EOFs from the four gateways. Panel a,c shows the EOFs of periods larger than 30 days (intra-annual) and panel b,d displays the EOFS or periods between 2 and 30 days (monthly variability). The thick black line indicates the mean flow at each mooring and the modes are shown with dashed lines (red: positive, black: negative). **e,** time series of the amplitudes of the EOFs shown in a-d.

4.4 Spatio-temporal links between the exchange gateways of the glacial cavity

Applying filters before calculating the EOFs makes patterns in the lower frequencies visible that are otherwise masked by the high variances associated with the tides. For the low frequency bands (T>2 days), mode 1 and mode 2 explain together between 83% (intra-annual variability) and 65% (monthly variability) of the variance.
Mode 1 of the intra-annual variability (68% explained variance) depicts the expected balance between Dijmphna Sund and the inflow depression (Fig. 4.7a). Increased outflow at Dijmphna Sund is compensated by enhanced inflow at M2 and vice versa.
Additionally, the EOFs reveal that in phases of increased inflow, one also observes enhanced outflow at M3 and M4, a relationship that has not been detected in the time series analysis presented in Section 4.2. In contrast, at M2, one observes a decrease in export between 120-240 m.
For mode 2 (16%) the relevance as export gateway is interchanged for Dijmphna Sund (M1) and M2 (outflow). Increased inflow is compensated by stronger outflow at M2 (100-270 m) and M3 instead of through Dijmphna Sund.
The temporal varying relevance of mode 1 and 2 and their prevailing phase is given by their amplitudes, depicted in Figure 4.7e. The amplitude of mode 1 describes the two main phases already pointed out based on the time series analysis of current speeds characterized in Section 3.2. Mode 1 is negative from September until December, i.e. flow speeds are decreased, and positive between December and March.
Consequently, the EOFs of the intra-annual variability illustrate that variability of the inflow may be compensated by different export gateways, mainly Dijmphna Sund (mode 1) and M2 (shallow depths, mode 2). This complexity may explain why there is no obvious relationship between the outward directed transport time series.

Mode 1 of the monthly variability explains 48% of the total variance. In contrast to the intra-annual variability, most variance is found in the upper water column, i.e. the outflow, while the inflow remains almost constant (Figure 4.7b). Mode 1 also emphasizes a spatial difference. While outflow decreases at the main glacier front (M2, M3, M4) at almost constant inflow, Dijmphna Sund reaches its maximal export volume. Also, this mode indicates the largest changes in the depth of flow reversal at M2.
The second mode of the monthly variability accounts for only 16.8% (mode 3: 12%) and accents changes in the upper 100-170 m (Figure 4.7d). Unless all the other modes, there is no obvious balance between the export through Dijmphna Sund and the flow at M2. Flow speeds at Dijmphna Sund are enhanced in the upper 100-130 m, but reduced below, i.e., may compensate each other. A similar situation is observed at M2.
The amplitude of both modes of the monthly variability have larger amplitudes from mid of December onwards (Figure 4.7e).

Summing up, the EOFs of the monthly variability confirm that at these time scales, one finds only a weak connection between water flowing into and out of the subglacial cavity. The first mode characterizes a setup in which variations in the flow in Dijmphna Sund and the outflow at the main calving front balance each other. The variability in volume transport is subsequently partly introduced by variability in the outflow, not necessary the inflow. Thus, parts of the variations in the export of mAIW via Dijmphna Sund may be interpreted uncoupled from the variability observed in the inflowing currents at the main calving front. Furthermore, mode 1 of the monthly variability has the strongest impact on the depth at which the flow reverses at M2. The EOFs suggest that variations of this depth are accompanied by larger changes in the outflow.

The EOFs stressed that large parts of the variability observed at Dijmphna Sund is linked to the cavity circulation. The interplay of the different gateways can explain a part of the variability at monthly time scales, but it remains unclear so far, what introduces the variability at intra-annual time scales. This question is elaborated in the next Section.

4.5 Potential drivers of the observed variability in the exchange flow

The Sections above highlight that at intra-annual time scales, Dijmphna Sund and the inflow at M2 balance each other in most cases (Mode 1, 67.8% of the total variance). Consequently, this variability may have important implications for ocean-glacier interaction with respect to the amount of melting the glacier from below. The following two subsections will investigate whether the intra-annual variability is rather related to changes of the buoyancy driven circulation induced by freshwater supply (Section 4.5.1) or whether external forces controlling the shelf circulation have an impact on the fjord circulation (Section 4.5.2).

4.5.1 Freshwater supply

Since the buoyancy-driven estuarine exchange flow is sensitive to freshwater input, the supply of basal melt water and surface runoff is investigated. To compare the supply of basal melt in 2016 and 2017, two approaches are chosen: First, basal melt rates of the floating tongue are estimated using remotely sensed data. Second, melt water fractions are derived from an OMP (see Section 2.1.3 and appendix) analysis that split mAIW into AIW, basal melt and surface runoff (Fig. 4.8, for details on method see also thesis paper, appendix).

Basal melt rates were estimated using a fluxgate approach, i.e. ice flux at the grounding line was compared with the one at the calving front. After correcting for divergence and surface melt, the resulting difference was accounted to basal melt. Ice flux was defined as the product of velocity at the gate and the cross-section of the gate (see Section 2.2.3).
In 2016, the mean glacier at the grounding line was $1207 \pm 200\,\mathrm{m\,yr^{-1}}$. In 2017, the speed at the grounding line were higher with $1267 \pm 305\,\mathrm{m\,yr^{-1}}$. Ice front velocities were inferred from a section that was located before the glacier tongue divides into the main calving front and the Dijmphna Sund calving front. Thus, one can take into account both gateways and the fact that speed values at the calving front are often noisy due to mixed pixels with sea ice. Mean velocities at the calving front fluxgate were $486 \pm 82\,\mathrm{m\,yr^{-1}}$ and $513 \pm 153\,\mathrm{m\,yr^{-1}}$ in 2016 and 2017, respectively.
The mean surface mass balance for 2016 (-1.79 ± 0.34 m) and 2017 (-1.13 ± 0.32 m) based on the regional climate model RACMO2.3p2 (personal communication, B.Noël, 2018) indicates less surface melting in 2017. Geometrical factors as divergence, the distance between

Table 4.1: End-members of OMP with their uncertainties: Atlantic Intermediate Water (AIW) in 2016 and 2017, basal melt water (BMW) and subglacial runoff (SGR)

	AIW_{2016}	AIW_{2017}	BMW	SGR
Θ [°C]	1.34 ± 0.11	1.68 ± 0.06	−93 ± 0.27	−0.22 ± 0.13
salinity [ ]	34.83 ± 0.05	34.86 ± 0.02	0	0
oxygen [μmol l^{-1}]	295 ± 1	295 ± 1	1253 ± 8	311 ± 2

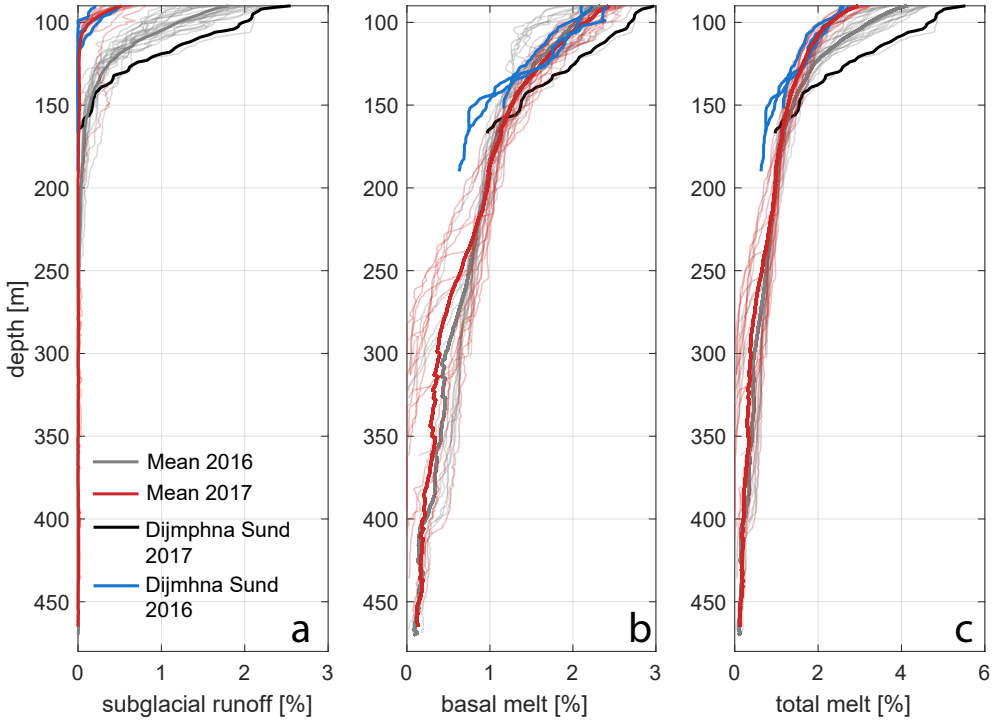

Figure 4.8: Profiles of meltwater fractions based on CTD survey in 2016 and 2017. Profiles of all casts from 2016 and 2017 are displayed in gray and red, respectively. The profiles from Dijmphna Sund are highlighted. **a,** fraction of subglacial runoff. **b,** fraction of basal melt. **c,** combined fraction of subglacial runoff and basal melt.

the grounding line and the calving front and the ice thicknesses were assumed to be constant over the short time period. Ice thickness at the grounding line was 602 ± 48 m, and 145 ± 44 m at the calving front fluxgate.
Based on the glacial mass budget calculations, I derived basal melt rates of of 8.0 m yr^{-1} and 9.2 m yr^{-1} for 2016 and 2017, respectively. The error was estimated applying error propagation on all formulas. In cases in which the spatial variability expressed in the standard deviation outweighs the estimated error of the data set, the former was used. This yield in an uncertainty estimate of ± 2.0 m yr^{-1} and ± 2.9 m yr^{-1} in 2016 and 2017, respectively. Consequently, the results lie within the uncertainty of the method.

For the melt water analysis, the end-members for run-off and basal melt water were derived from theoretical considerations and therefore assumed to be constant for both years. The end-member of AIW in 2017 was found for each year by picking the warmest twelve measurements (at 12 different locations from the calving front, see Tab. 4.1). The observed warming of the AIW made it necessary to adapt the end-member. Error estimates are given based on a Monte-Carlo simulation with disturbed end-member in the range of their standard deviation (see thesis paper, appendix). The simulation revealed that subglacial runoff and basal melt have an error of 5.3% and 11.5%, respectively.
The OMP confirmed the reduction in surface runoff in 2017. The results show substantially less surface runoff in 2017 (mean 90-100 m: 0.31 ± 0.02%) than 2016 (mean 90-100 m: 1.48 ± 0.08%, Fig. 4.8). Net monthly mass loss takes place in June, July, and August in both years.
In contrast to the glaciological estimates, the OMP indicates a slight decrease in basal melt water in mAIW for 2017. On average, 1.29 ± 0.15% (2016: 1.42 ± 0.17 %) of the mAIW was basal melt. The decrease in basal melt water fraction is found mostly below depths

of 200 m, whereas in the upper 90-150 m, basal melt water fractions remained constant. Possible sources of errors as e.g. errors in the end-member or a different choice of stations that introduce a spatial bias.

In brief, the analysis above lead to differences in melt water between 2016 and 2017 that lie within the uncertainties of the methods what makes it difficult to come to a conclusion on the impact of freshwater onto the cavity circulation. A second driver is explored in the following Section to identify other potential sources.

4.5.2 Remote control

Besides a link to the buoyancy driven circulation, the intra-annual variability may also be linked to large-scale atmospheric and/or oceanographic pattern. In this case, other locations at the shelf should share the oceanic variability observed at the 79NG. Thus, in the following, flow characteristics into the subglacial cavity are compared to measurements carried out in the boundary current observed in Norske Trough. *Schaffer et al.* (2017) showed that AIW present in the 79NG bay has been carried by a bottom-intensified flow from the shelf break via Norske Trough towards the 79NG. Figure 4.9 displays the velocities of the strongest flow of the inflow at the 79NG calving front and a mooring located close to Île de France, located in Norske Trough, i.e. southeast of the 79NG calving front. At both locations, the depth bin with the strongest flow (M2: 436 m, M5: 300 m) was rotated into the main flow direction, detrended and normalized by their variance to emphasis the variability that they have in common. Low-pass filtered at a cutoff period of 2 days, the velocity time series show a significant correlation of R=0.48. A low-pass filter of 30 days increased the correlation to R=0.61. Filtering the signal with a bandpass filter of width 2 days and with variable start/end points from 1 to 60 days revealed that mainly the periods of 16 to 28 days (max. at 18 days) and periods larger than 34 days contribute to the high correlation. Thus, drivers of the shared variability act most likely at time scales larger than 18 days.
Cross-correlation functions indicate a delay between M2 at the glacier front and the mooring at Île de France. The delay depends on the filtering applied (i.e. the frequencies present) and the time period that is compared. To estimate a mean and a range for the delay, cross-correlations were calculated systematically for each filtering between 4-18 days and three-month intervals shifted always by 14 days. The limits for the filtering were chosen based on the correlation coefficient. At 4 days the correlation coefficient is larger than 0.5, i.e. one assumes a robust similarity that the algorithm can detect. At 18 days the correlation coefficient is largest. The lengths of the time intervals of three months was a trade-off between temporal resolution and a sufficient amount of independent data points for the comparison. Shifts greater than 10% of the length of the time series (9 days) were excluded to sustain a statistically reliable result (*Talley et al.*, 2011). This resulted in 252 valid observations with a mean of 27 hours and a standard deviation of 29 hours. The cross-correlations indicated that for September until mid of November, longer periods (larger low-pass filter), resulted in larger delays (approx. 60 hours). This shifted, going together with a general decrease in delay (to about 30 hours) in mid of November until July, when shorter periods indicated less delay.

A signal with a mean delay of 27 hours needs a speed of 1.75 m s^{-1} to cover the distance of 170 km (direct pathway) between the moorings. In case of a difference of 56 hours, a speed of 0.84 m s^{-1} is necessary. The upper boundary is given by a delay of $\pm$ 1 hour, that requires a speed of 47 m s^{-1}. Taking into account that the signal is first observed at M2, but mean flow speeds are directed into the opposite direction, the speed estimate needs to be corrected for this mean flow before being compared to theoretical considerations of

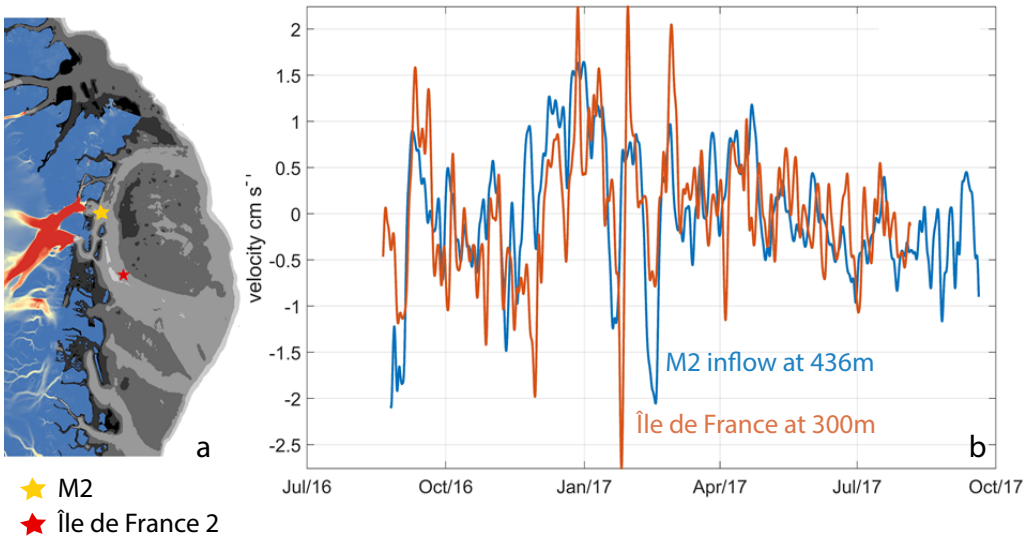

Figure 4.9: Speed rotated in the direction of the strongest flow at M2 (calving front) and Île de France. a, mooring location of M2 and Île de France 2 on the Northeast Greenland shelf. See Figure 1.3 for details on the currents. **b,** rotated currents measured at M2 and Île de France. The time series are from the depth bin of the strongest flow and are low-pass filtered (cut-off frequency 4 days).

phase velocity calculations. *Schaffer* (2017) estimated a mean flow speed of 5 cm s^{-1} of the AIW layer in Norske Trough. Considering that, the phase velocity of the signal would be 1.80 m s^{-1} in absence of a mean flow.

Travel times for barotropic waves were estimated to be in the order of 1 hour (density of 27.4 kg m^{-3}, water depth of 300-400 m, formula see Section 2.1.4). Consequently, shorter delays in the order of an hour may be explained by barotropic waves. For a rough estimate of the speed of the baroclinic wave (Section 2.1.4), the water column was simplified into a PW layer (25.5-27 kg m^{-3}) occupying the upper 100-200 m and a AIW layer below (27.8 kg m^{-3}). This range of values results in speeds between c=0.87 m s^{-1} (ρ_{PW}=1027 kg m^{-3}, thickness of 100 m) and c=2.10 m s^{-1} (ρ_{PW}=25.5 kg m^{-3}, thickness of 200 m). According to this rough estimate, interfacial internal waves would be able to travel the distance in 23-57 hours (1-2.4 days). Those results fit well with the range of speeds derived from the delay.

Thus, the results presented in this chapter have elaborated that the low-frequency variability in the currents at Dijmphna Sund are linked to the cavity circulation. The variations in the cavity circulation are most likely introduced by large-scale baroclinic waves. Potential forcing of those waves and implications of this results are discussed in Section 4.6.1.

4.6 Discussion

At intra-annual time scales (T>30 days) the time series of the flow through Dijmphna Sund and the one of the inflow at the main calving front resemble each other. Thus, they are connected, implying that the intra-annual variability is affecting the cavity circulation at the 79NG which has most likely an affect on the basal melt rates.

Comparing the current time series and calculating EOFs showed that there is only a weak link between the outflow observed at the four export gateways. This lack of coherent behavior may arise from an export of mAIW that varies spatially or due to incomplete observations. Depending on the origin of the plume, mAIW export may vary greatly in space. The spatial initialization of the plume at the grounding line and its subsequent pathways under the ice guided by basal channels (*Millgate et al.*, 2013; *Wilson et al.*, 2017) may be responsible for the systematic change between M2 and Dijmphna Sund as preferred export pathway (see EOFs, intra-annual variability).
Spatial variability of the outflow may also be introduced at the calving front. The circulation is expected to be three-dimensional with multiple plumes interacting, while further away (i.e. in Dijmphna Sund), the lateral gradients may have been reduced by mixing, resulting in a two layer circulation (*Straneo and Cenedese*, 2015). Consequently, one mooring may be sufficient to extrapolate flow through the channel at Dijmphna Sund, but not at the export gateways at the main calving front. As the inflow happens mostly through the channeled inflow depression, it is better constrained. Consequently, one can assume that inflow at the main calving front and outflow through Dijmphna Sund reflect the variability of the cavity circulation best. Thus, discrepancies may be party related to incomplete observations at the calving front.

The positive correlation between the outflow through Dijmphna Sund and the inflow at M2 at time scales of T>30 days is a major outcome based on various methods. Still, due to the short duration of the time series at Dijmphna Sund (191 days), further measurements from instruments that are currently still deployed will help to constrain the link. Additionally, a continuation of the time series for one or two years may confirm whether the acceleration of the current speeds is a seasonal signal associated with the winter months as suggested by *Topp and Johnson* (1997).
At shorter time scales of 2-30 days, the connection between inflow at M2 and outflow through Dijmphna Sund is less pronounced. The EOFs suggest that at monthly time scales, mainly the export gateways interact with each other. However, as the EOFs were calculated based on compensated transport calculations, one also needs to consider an artificial origin of the signal. It was renounced to normalize the time series by their variance to keep the physical meaning of the numbers before calculating the EOFs. Consequently, time series with large variability (Dijmphna Sund and the inflow) are weighted stronger. Therefore, variability at M1 (defined as product of amplitude and mode) may dominate the EOF with little contributions from M2, M3, and M4.

4.6.1 Drivers of intra-annual variability

Having identified the intra-annual variability as part of the cavity circulation, freshwater supply was examined as potential driver.
The buoyancy-driven estuarine exchange flow is sensitive to the amount of freshwater input, as the plume's buoyancy depends directly on it (e.g. *Motyka et al.*, 2003; *Straneo et al.*, 2011). Therefore, changes in the supply of basal melt water and runoff may have an impact on the circulation. A recent study about the 79 NG indicated cavity exchange time scales of 90 $\pm$ 35 days (*Mayer et al.*, 2018), i.e. a time span significantly shorter than the period

of the observed warming (> 8 months). Following (*Holland*, 2017), one can expect an equilibrium response in melting to the temperature increase, i.e. stronger basal melt in 2017 compared to 2016 is reasonable.
Estimated melt rates of 8.0 ± 2.0 m yr^{-1} and 9.2 ± 2.9 m yr^{-1} are lower than the 12.2 ±1.6 m yr^{-1} derived from an ice-shelf plume model for oceanographic conditions in 2014 (*Mayer et al.*, 2018), but fit well with estimates of 8.3 ±2.1 m yr^{-1} derived from heat and salt budgets in 2016 (*Schaffer*, 2017). *Wilson et al.* (2017) estimated an submarine melt flux of $1.32{\cdot}10^{10}$ m^3 yr−1 ice for 2011-2015 based on Lagrangian hydrostatic ice thickness changes calculated from digital elevation models. Their result is about 17% larger than the results obtained for 2017 with the fluxgate approach. Overall, my estimates are in the same order of magnitude as the ones calculated in earlier studies. Deviations may arise from the uncertainties of the different approaches, but also due to the fact that the fluxgate approach relies on the assumption that the ice tongue is in steady state, i.e. ice speeds can exactly compensate the loss due to surface and basal melt, resulting in a constant ice thickness (*Enderlin and Howat*, 2013; *Wilson et al.*, 2017). However, recent studies showed that this assumption is violated because the floating tongue is thinning; most likely due to increased basal melt (*Mayer et al.*, 2018; *Wilson et al.*, 2017). Therefore, the fluxgate approach is likely to underestimate the basal melt rates.
The OMP, however, reveals no significant increase in basal melt between summers 2016 and 2017. When comparing results from both approaches, one needs to consider that the OMP probably reflects melt rates from 90 ± 35 days (*Mayer et al.*, 2018), whereas the glacier speeds (most influencing component of the fluxgate approach) were averaged over April to October 2017 (7 months). This long averaging period prevents final conclusions on the influence of basal melt water on the intra-annual variability. However, most likely, the time scales of the intra-annual variability are too short to be explained by changes in the basal melt rate. The error estimates indicate that both methods, OMP and fluxgate, produce differences between 2016 and 2017 that lie within their measurement uncertainty. The uncertainty estimate of the fluxgate approach is conservative and different spatial realizations may help to reduce the error. Furthermore, one could revisit the velocity errors following *Paul et al.* (2017), because they are the largest source of uncertainty with ± 105 m s^{-1}(2016) and ± 205 m s^{-1} (2017).
In context of increased AIW and mAIW temperatures that equal a warming that was observed before comparing 1979-1999 with data from 2000-2016 (*Schaffer*, 2017), a potential increase in basal melt rates shall be considered. In principle, basal melt increases quadratically when the ocean warms (*Holland et al.*, 2008), but considering a warming of mAIW at the same time, the extracted heat may have remained constant. In this case, an increased cavity circulation may have lead to more heat flux to the ice base and may have caused increased basal melt. *Schaffer* (2017) suggested the circulation is additionally forced by a hydraulically controlled inflow descending the sill located to the North (325 m) of the inflow depression. Since the speed of the gravity plume is very sensitive to the height of the AIW layer above this sill, a temperature increase that is connected to a thickening of the AIW layer, may influence the strength of the inflow as well. Any other mechanism working comprehensive over the shelf influencing the AIW layer, would also impact the cavity circulation and subsequently the basal melt rate (*Mayer et al.*, 2018).

The high correlation between the inflow at the calving front and the currents at Norske Trough suggest that waves may be such a mechanism influencing the cavity circulation. Besides high travel speeds, further evidence for waves is provided by the wavelet of M2. Here, the horizontally elongated features at periods of 20-33 days are associated with low frequency, wave-like variability (see Fig. 4.5). Additionally, the presence of waves at the glacier front is supported by the temperature records from the calving front that show a

high correlation and (almost) no time delay between in- and outflow. Waves heaving the thermocline may be responsible for those variations.
A few conclusions may be drawn from the observations about the characteristics of the waves. First, they travel on large scales, because they were measured at two sites 170 km apart from each other. This fits with the second observations that their periods are subinertial, probably in the order of 18 days at which the best correlation is reached between both records. Thirdly, the estimated average speed is in the order of $1.7\,\mathrm{m\,s^{-1}}$. Fourthly, the waves may be dispersive, since the filtering has a large impact on the estimated delays, indicating that waves of different frequency, travel at different speeds. Fithly, the wave action is enhanced during the winter months, but also present in all other seasons. Finally, the travel direction is probably north to south, because the signal is first observed at the 79NG. Here, some limiting considerations are needed. It may be that the forcing is always closer to 79NG, but not necessarily to the north what could also lead to the observed delay. Further, since the time delay is not constant, the location where the wave is initiated, may vary as well. Additionally, reflections could lead to a more complex travel path as purely north-south.
Those considerations lead to the hypothesis that the observed waves may belong to the class of topographic waves (coastal-trapped waves). This class of waves is found at the coast (or other topographic features) and on sloping continental shelfs. They are induced by an ambient potential-vorticity gradient because of the continental slope (*Cushman-Roisin*, 1994; *Gill*, 1982) and are characterized by large wavelengths (tens to hundreds of kilometers) and subinterial periods (*Buchwald and Adams*, 1968; *Talley et al.*, 2011). Further, those waves have in common that they propagate with shallow water to the right, and that their amplitude decays towards the ocean. One extreme case of this wave class are Kelvin wave that are solved for an ideal ocean with a flat bottom topography and vertical sides (*Dukhovskoy et al.*, 2009). Kelvin waves obey the same laws for phase speed as gravity waves; i.e., they can be approximated as long internal gravity waves (*Dukhovskoy et al.*, 2009; *Talley et al.*, 2011). Using this approximation (see 2.1.4 for equation and Section 4.5.2 for results) and assuming a wave traveling from north to south, one can conclude, that internal Kelvin wave speeds are high enough to explain a delay of at least 23 hours. Kelvin waves are non-dispersive, and consequently, one needs to elaborate whether the assumption of dispersion of the waves observed is valid.

Inall et al. (2015) showed how coastal-trapped waves contributed significantly to fjord-shelf exchange in a large fjord in Svalbard. Similar to this study, they observed an intensification in coastal-trapped wave energy during winter and related it to the weaker stratification during autumn (changes wave speed) and winter and the higher abundance of storm-events in Fram Strait. Topographic waves may be caused by different mechanisms. Other waves (e.g. tides) traveling along the continental shelf and interacting with irreguarities of the topography (*Brink*, 1991), meander in large ocean currents (*Shaw and Csanady*, 1988) and large scale-wind fields inducing coastal up- and downwelling are known to introduce them (*Brink*, 1991; *Dukhovskoy et al.*, 2009; *Inall et al.*, 2015). Considering the seasonality observed in the wave energy, one might hypothesize that a driver with a similar enforcement in winter is forcing the waves, e.g. the East Greenland Current (*Bacon et al.*, 2014), increased eddy activity of the West Spitzbergen current (*von Appen et al.*, 2016), or large-scale weather systems (*Rogers*, 2005). In case of large-scale weather systems as forcing of the waves that lead Ekman transport, this could serve as well as consistent theory for the observed link between current velocities and sea ice concentration at Dijmphna Sund described in Section 3.3.

The assumptions made above are made based on observations from two spots, and consequently, observations from Westwind Trough and other shelf locations may help to confirm

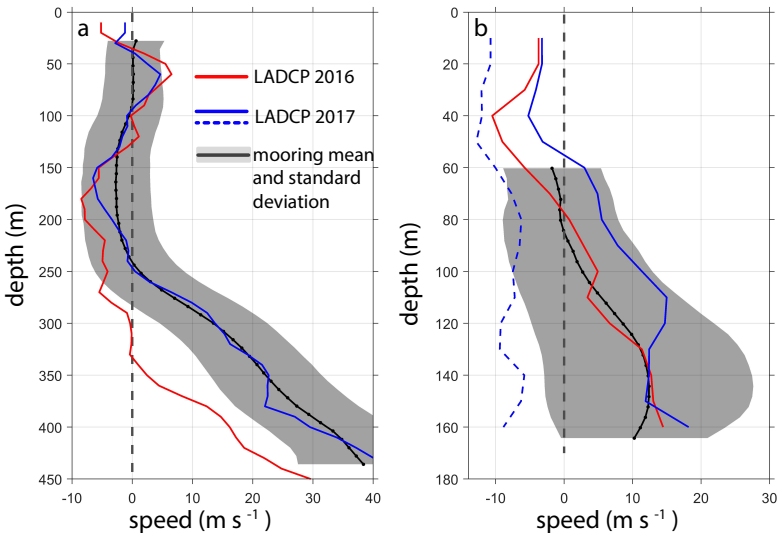

Figure 4.10: LADCP measurements in the framework of flow velocities established by the moorings. LADCP profiles measured in 2016 and 2017 are overlain on the mean and standard deviation from the moored velocity measurements. **a,** M2. **b,** M1. The two different casts in 2017 are displayed with a solid and dashed line.

the speed and travel direction of the waves. Model runs with for example FESOM (*Danilov et al.*, 2017) may add additional knowledge on wave propagation on the shelf and potential drivers. Extending the current time series by another year may also add evidence on the proposed seasonal nature of the wave activity.

4.6.2 Implications of the intra-annual variability

The observations covering 7-12 months enabled a detailed characterization of the variability of the currents. The framework helps to put single observations into a broader context. As example, the LADCP survey in 2016 at the inflow depression (M2) shows abnormal low (outside of the one standard deviation of the yearly mean) flow velocities and indications of a three layer flow as described for characteristic low inflow events at the end of January and February 2017 (Fig. 4.10a). As the moored observations at M2 show that this situation lasted for a few more days, it is probably comparable to the one in winter. At Dijmphna Sund, two profiles were taken at the mooring location in 2017, that were 6 hours apart from each other (Fig. 4.10b). Their different flow directions illustrate well the large impact of tides onto the flow at Dijmphna Sund. Both examples stress the importance of this framework for future observations.

Improving our understanding of the sources of the intra-annual variability is of high relevance for basal melt rate and the freshwater export to the shelf. Comparing characteristic features of the current time series of Dijmphna Sund and the inflow reveals that they appear slightly delayed at Dijmphna Sund. Therefore, one can assume that the waves are indeed traveling through the cavity. Even though the exchange rate is zero for baroclinic waves, they can introduce vertical mixing (see also Section 3.4 on tidal effects). The effect of upward mixing of heat in the glacial cavity due to waves, shall be addressed in future work. Characterizing only the short-term changes induced by the changes in velocity lead to melt rates ranging between 0 and 16 m yr^{-1} (low-pass filtered with cut-off frequency of 2 days, personal communication, J. Schaffer, 2018) and freshwater pulses at Dijmphna Sund of 2 mSv. The latter was calculated assuming a mean freshwater content of 2.15% (average of 2016 and 2017) and a maximal transport of -95 mSv.

The variability and the potential consequences discussed above are unlikely to be restricted to Dijmphna Sund and the 79NG bay. The high impact of waves onto the fjord circulation that are most likely produced by large scale atmospheric variations is anticipated in other

east Greenlandic fjords, that are characterized by deep sills and moderately strong tides. This implies that changes of the large scale atmospheric conditions have an direct impact on glacial fjord circulation and therefore on melting rates of marine-terminating glaciers. Consequently, assessments of the future changes at the 79NG and potentially other glaciers to present day climate change, need to take into account not only warming of the ocean, but also a possible impact of changes in the wave energy of low-frequency waves on the continental shelf.

5 Conclusions and Outlook

In this thesis, the variability of the glacial cavity circulation of the 79 North Glacier (79NG) has been explored, with particular focus on the currents at Dijmphna Sund. The analysis of a comprehensive data set of oceanographic observations at all gateways of the 79NG cavity, covering a time span of seven to twelve months, allowed to answer the following two questions:

1. What are the dominant time scales of current variability in Dijmphna Sund and how are they linked to local and regional drivers?

Current variability at Dijmphna Sund can be split into three groups. More than half of the variance (53%) is associated with barotropic tides. They dominate the sub-daily to daily range and are the only observed driver that can generate significant changes in the flow direction below 140 m at Dijmphna Sund. Compared to the tides observed close to the main calving front, tides in Dijmphna Sund are enhanced, most likely due to the channelized geometry and the shallow water-depth that initiate strong tidal currents and shallow-water tides. Knowledge about the tidal magnitude was found to be crucial when interpreting short-time current measurements from Dijmphna Sund.
The other half of the variability is observed at longer time scales (T>2 days) and is related to more regional processes. The daily to monthly time scales (from 2 to 30 days) accounts for 29% of the variance. At those time scales, current variations are weakly linked to sea ice conditions close to the coast and to enhanced wind speeds. Wind-induced Ekman pumping was proposed as potential mechanism explaining the relationship. When the sea ice concentration falls below 80-90%, wind stress to the ocean and subsequent down- and upwelling would be enhanced, influencing the ocean currents. Intra-annual variability (T>30 days) comprises 14% of the variance and exhibits a characteristic pattern with a low-energy phase from September until mid of November and a high-energy phase with fast speed fluctuations from mid of November until March. Since this characteristic pattern was also observed at the main calving front, the second research question has been posed as follows.

2. How does the cavity circulation influence the variability of mAIW export through Dijmphna Sund?

The Empircial Orthogonal Functions (EOFs) results indicate that the interaction between Dijmphna Sund and the 79NG cavity is time scale depended. At monthly time scales (2-30 days) variability is mainly limited to the flow in intermediate depths (90-240 m). Here, increased flow at one gateway is compensated by reduced flow at the other, while the inflow remains constant. Neither the EOFs (48% explained variance), nor the weak anti-correlation ($R = -0.33$) to sea ice conditions can explain the monthly variability of currents in Dijmphna Sund on its own. Therefore, a non-linear combination of at least those two processes is suspected.
At intra-annual timescales there is a strong link between the inflow at the main calving front and the export of mAIW through Dijmphna Sund, confirming that this part of the variability observed in Dijmphna Sund is clearly induced by the cavity circulation. The EOFs emphasize that the export through Dijmphna Sund balances in most cases (67%)

the variability of the inflow. The latter is most likely not generated by the buoyancy-driven circulation of the glacier, but rather by a different, remote large-scale driver. This hypothesis is based on the strong correlation (R=0.65) of the inflow at the calving front with velocities measured 170 km further south in the bottom-intensified boundary current that transports AIW to the 79NG. The signal delay between the two records is 27 ± 29 hours. This period of time appears too short to explain the correlation with advective processes. Barotropic and baroclinic topographic waves could offer a plausible explanation for the travel direction from north to south and the range of the observed delay. The origin of the topographic waves is not clear yet, since both, large-scale oceanographic and atmospheric changes lead to the generation of such waves. In the case of periodic up- and downwelling induced by large-scale wind fields as origin of the wave, the resulting Ekman transport could also provide a consistent explanation for the correlation between current speeds in Dijmphna Sund and sea ice conditions at the coast, as described in Section 3.3 and 3.4.

To summarize, analyzing the current variability at Dijmphna Sund, lead to the conclusion that most variability in Dijmphna Sund is induced by waves, in particular tides and low-frequency waves. Even though, those do not affect the mean flow directly, they can generate vertical mixing that has the potential to establish a flow and may increase the heat content of the waters in direct contact with the floating glacier tongue. Any non-linear processes, as e.g. the quadratic relationship between temperature and melt rate, will be enhanced by such waves. Combined with the observed temperature increase of 0.5°C in the AIW and mAIW, internal wave induced vertical mixing may have large consequences for the basal melt rates at the 79NG and subsequent freshwater export to the continental shelf.

In addition to this outcome, several objectives to be addressed in future work were identified in this thesis.
First, the moored observations need to be continued to confirm the link between the export of mAIW via Dijmphna Sund and the inflow at the main calving front also during other seasons than autumn and winter. Furthermore, longer time series are required to investigate the potential seasonality in the records.
Second, having identified the impact of waves, future studies may quantify the effects of wave-induced mixing in the 79NG cavity by exploring temperature and salinity datasets available from the calving front. Here, additional models of the subice cavity will be useful to compensate the lack of long-term observational data within the cavity.
Third, atmospheric observations from the calving front, or alternatively, high-resolution climate models able to resolve the complex topography of the fjord system at the 79NG, will be helpfull to clarify the dependency of the oceanic transport on local weather conditions.
Finally, a high resolution coupled ocean-atmosphere model with realistic continental shelf bathymetry and wave propagation, will add knowledge on potential drivers of the low-frequency waves. The current variability described in this study and its potential consequences for the 79NG are most likely an important part of the variability in current speeds in other glacial fjords, too. Therefore, modeling the origin and propagation of those waves may help to deepen our understanding of the impact that large-scale variability has on circulation in Eastern Greenland's glacial fjords. Eventually, those improvements will help to understand better the oceanic influence on the intra-annual variability of basal melting of marine-terminating glaciers.

Acknowledgement

Foremost, I would like to thank Dr. Janin Schaffer and Prof. Dr. Torsten Kanzow for their tireless support. Many thanks for the excellent supervision, for all the time that you spend discussing with me my progress, and for the strong interest in my topic. Thank you for truly engaging me with the GROCE project, for letting me participate in my first research cruise (PS109) and for sending me to my first conference.
I would like to acknowledge the University of Bremen for providing the sea ice concentration data that I have downloaded via the meereisportal (http://www.meereisportal.de, support REKLIM-2013-04). Brice Noël is acknowledged for sharing his new surface mass balance data with me.
Special thanks to Andreas Muenchow who showed me the wind data from Henrik Krøyer Holme and always had an open door when I had a quick question. Further, I would like to express my gratitude to Prof. Dr. Monika Rhein for accepting to review my thesis.
Finally, I would like to thank my great proof-readers, first of all, Dr. Janin Schaffer whose comments helped to improve this manuscript a lot. Thanks to Lorenzo, Florentina, Paula, Anna-Lena, Lutz, and Andy for your amazing support.

Bibliography

Bacon, S., A. Marshall, N. P. Holliday, Y. Aksenov, and S. R. Dye, Seasonal variability of the East Greenland Coastal Current, *Journal of Geophysical Research: Oceans*, *119*(6), 3967–3987, doi:10.1002/2013jc009279, 2014.

Bamber, J., M. van den Broeke, J. Ettema, J. Lenaerts, and E. Rignot, Recent large increases in freshwater fluxes from Greenland into the North Atlantic, *Geophysical Research Letters*, *39*(19), doi:10.1029/2012gl052552, 2012.

Bamber, J. L., R. M. Westaway, B. Marzeion, and B. Wouters, The land ice contribution to sea level during the satellite era, *Environmental Research Letters*, *13*(6), 063,008, doi:10.1088/1748-9326/aac2f0, 2018.

Beaird, N., F. Straneo, and W. Jenkins, Spreading of Greenland meltwaters in the ocean revealed by noble gases, *Geophysical Research Letters*, *42*(18), doi:10.1002/2015gl065003, 2015.

Bendtsen, J., J. Mortensen, K. Lennert, J. K. Ehn, W. Boone, V. Galindo, Y. bin Hu, I. A. Dmitrenko, S. A. Kirillov, K. K. Kjeldsen, Y. Kristoffersen, D. G. Barber, and S. Rysgaard, Sea ice breakup and marine melt of a retreating tidewater outlet glacier in northeast Greenland (81°N), *Scientific Reports*, *7*(1), doi:10.1038/s41598-017-05089-3, 2017.

Bevan, S. L., A. J. Luckman, and T. Murray, Glacier dynamics over the last quarter of a century at Helheim, Kangerdlugssuaq and 14 other major Greenland outlet glaciers, *The Cryosphere*, *6*(5), 923–937, doi:10.5194/tc-6-923-2012, 2012.

Böhm, E., T. Hopkins, and P. Minnett, Passive microwave observations of the Northeast Water Polynya interannual variability: 1978–1994, *Journal of Marine Systems*, *10*(1-4), 87–98, doi:10.1016/s0924-7963(96)00080-2, 1997.

Böning, C. W., E. Behrens, A. Biastoch, K. Getzlaff, and J. L. Bamber, Emerging impact of Greenland meltwater on deepwater formation in the North Atlantic Ocean, *Nature Geoscience*, *9*(7), doi:10.1038/ngeo2740, 2016.

Boone, W., S. Rysgaard, S. Kirillov, I. Dmitrenko, J. Bendtsen, J. Mortensen, L. Meire, V. Petrusevich, and D. Barber, Circulation and fjord-shelf exchange during the ice-covered period in Young Sound-Tyrolerfjord, Northeast Greenland (74°N), *Estuarine, Coastal and Shelf Science*, *194*, 205–216, doi:10.1016/j.ecss.2017.06.021, 2017.

Bourke, R. H., J. L. Newton, R. G. Paquette, and M. D. Tunnicliffe, Circulation and water masses of the East Greenland shelf, *Journal of Geophysical Research*, *92*(C7), doi:10.1029/jc092ic07p06729, 1987.

Brink, K. H., Coastal-Trapped Waves and Wind-Driven Currents Over the Continental Shelf, *Annual Review of Fluid Mechanics*, *23*(1), 389–412, doi:doi:10.1146/annurev.fl.23.010191.002133, 1991.

Buchwald, V. T., and J. K. Adams, The Propagation of Continental Shelf Waves, *Proceedings of the Royal Society A: Mathematical, Physical and Engineering Sciences*, *305*(1481), 235–250, doi:10.1098/rspa.1968.0115, 1968.

Budéus, G., and W. Schneider, On the hydrography of the Northeast Water Polynya, *Journal of Geophysical Research*, *100*(C3), doi:10.1029/94jc02024, 1995.

Choi, Y., M. Morlighem, E. Rignot, J. Mouginot, and M. Wood, Modeling the Response of Nioghalvfjerdsfjorden and Zachariae Isstrøm Glaciers, Greenland, to Ocean Forcing Over the Next Century, *Geophysical Research Letters*, *44*(21), doi:10.1002/2017gl075174, 2017.

Church, J., P. Clark, A. Cazenave, J. Gregory, S. Jevrejeva, A. Levermann, M. Merrifield, G. Milne, R. Nerem, P. Nunn, A. Payne, W. Pfeffer, D. Stammer, and A. Unnikrishnan, Sea Level Change, in *Climate Change 2013: The Physical Science Basis. Contribution of Working Group I to the Fifth Assessment Report of the Intergovernmental Panel on Climate Change*, 2013.

Cottier, F. R., F. Nilsen, R. Skogseth, V. Tverberg, J. Skarðhamar, and H. Svendsen, Arctic fjords: a review of the oceanographic environment and dominant physical processes, *Geological Society, London, Special Publications*, *344*(1), 35–50, doi:10.1144/sp344.4, 2010.

Cushman-Roisin, B., *Introduction to Geophysical Fluid Dynamics*, Pearson College Div, 1994.

Danilov, S., D. Sidorenko, Q. Wang, and T. Jung, The Finite-volume Sea ice–Ocean Model (FESOM2), *Geoscientific Model Development*, *10*(2), 765–789, doi:10.5194/gmd-10-765-2017, 2017.

Dickson, R., B. Rudels, S. Dye, M. Karcher, J. Meincke, and I. Yashayaev, Current estimates of freshwater flux through Arctic and subarctic seas, *Progress in Oceanography*, *73*(3-4), doi:10.1016/j.pocean.2006.12.003, 2007.

Dmitrenko, I. A., S. A. Kirillov, S. Rysgaard, D. G. Barber, D. G. Babb, L. T. Pedersen, N. V. Koldunov, W. Boone, O. Crabeck, and J. Mortensen, Polynya impacts on water properties in a Northeast Greenland fjord, *Estuarine, Coastal and Shelf Science*, *153*, 10–17, doi:10.1016/j.ecss.2014.11.027, 2015.

Dmitrenko, I. A., S. A. Kirillov, B. Rudels, D. G. Babb, L. T. Pedersen, S. Rysgaard, Y. Kristoffersen, and D. G. Barber, Arctic Ocean outflow and glacier-ocean interactions modify water over the Wandel Sea shelf (northeastern Greenland), *Ocean Science*, *13*(6), 1045–1060, doi:10.5194/os-13-1045-2017, 2017.

Dukhovskoy, D. S., S. L. Morey, and J. J. O'Brien, Generation of baroclinic topographic waves by a tropical cyclone impacting a low-latitude continental shelf, *Continental Shelf Research*, *29*(1), 333–351, doi:10.1016/j.csr.2008.01.007, 2009.

Dukhovskoy, D. S., P. G. Myers, G. Platov, M.-L. Timmermans, B. Curry, A. Proshutinsky, J. L. Bamber, E. Chassignet, X. Hu, C. M. Lee, and R. Somavilla, Greenland freshwater pathways in the sub-Arctic Seas from model experiments with passive tracers, *Journal of Geophysical Research: Oceans*, *121*(1), doi:10.1002/2015jc011290, 2016.

Enderlin, E. M., and I. M. Howat, Submarine melt rate estimates for floating termini of Greenland outlet glaciers (2000–2010), *Journal of Glaciology*, *59*(213), doi:10.3189/2013jog12j049, 2013.

Enderlin, E. M., I. M. Howat, S. Jeong, M.-J. Noh, J. H. van Angelen, and M. R. van den Broeke, An improved mass budget for the Greenland ice sheet, *Geophysical Research Letters*, *41*(3), 866–872, doi:10.1002/2013gl059010, 2014.

Fahnestock, M., T. Scambos, T. Moon, A. Gardner, T. Haran, and M. Klinger, Rapid large-area mapping of ice flow using Landsat 8, *Remote Sensing of Environment*, *185*, 84–94, doi:10.1016/j.rse.2015.11.023, 2016.

Fairbanks, R. G., A 17,000-year glacio-eustatic sea level record: influence of glacial melting rates on the Younger Dryas event and deep-ocean circulation, pp. 637–642, Springer Nature, doi:10.1038/342637a0, 1989.

Falck, E., Contribution of waters of Atlantic and Pacific origin in the Northeast Water Polynya, *Polar Research*, *20*(2), doi:10.1111/j.1751-8369.2001.tb00056.x, 2001.

Gade, H. G., Melting of Ice in Sea Water: A Primitive Model with Application to the Antarctic Ice Shelf and Icebergs, *Journal of Physical Oceanography*, *9*(1), doi:10.1175/1520-0485(1979)009<0189:moiisw>2.0.co;2, 1979.

Gill, A. E., *Atmosphere-Ocean Dynamics*, Elsevier Science Publishing Co Inc, 1982.

Gillard, L. C., X. Hu, P. G. Myers, and J. L. Bamber, Meltwater pathways from marine terminating glaciers of the Greenland ice sheet, *Geophysical Research Letters*, *43*(20), doi:10.1002/2016gl070969, 2016.

Grosfeld, K., R. Treffeisen, J. Asseng, A. Bartsch, B. Bräuer, B. Fritzsch, R. Gerdes, S. Hendricks, W. Hiller, G. Heygster, T. Krumpen, P. Lemke, C. Melsheimer, M. Nicolaus, R. Ricker, and M. Weigelt, Online Sea-Ice Knowledge and Data Platform, *Polarforschung; 85*, doi:doi:10.2312/polfor.2016.011, 2016.

Hellmer, H. H., S. S. Jacobs, and A. Jenkins, Oceanic erosion of a floating Antarctic glacier in the Amundsen Sea, in *Ocean, Ice, and Atmosphere: Interactions at the Antarctic Continental Margin*, American Geophysical Union, doi:10.1029/ar075p0083, 1998.

Heuzé, C., A. Wåhlin, H. L. Johnson, and A. Münchow, Pathways of Meltwater Export from Petermann Glacier, Greenland, *Journal of Physical Oceanography*, *47*(2), doi:10.1175/jpo-d-16-0161.1, 2017.

Hill, E. A., J. R. Carr, and C. R. Stokes, A Review of Recent Changes in Major Marine-Terminating Outlet Glaciers in Northern Greenland, *Frontiers in Earth Science*, *4*, doi:10.3389/feart.2016.00111, 2017.

Hinrichsen, H.-H., and M. Tomczak, Optimum multiparameter analysis of the water mass structure in the western North Atlantic Ocean, *Journal of Geophysical Research*, *98*(C6), doi:10.1029/93jc00180, 1993.

Holland, D. M., R. H. Thomas, B. de Young, M. H. Ribergaard, and B. Lyberth, Acceleration of Jakobshavn Isbræ triggered by warm subsurface ocean waters, *Nature Geoscience*, *1*(10), doi:10.1038/ngeo316, 2008.

Holland, P. R., The Transient Response of Ice Shelf Melting to Ocean Change, *Journal of Physical Oceanography*, *47*(8), 2101–2114, doi:10.1175/jpo-d-17-0071.1, 2017.

Holton, J. R., *An Introduction to Dynamic Meteorology, Volume 88 (International Geophysics)*, Academic Press, 2004.

Huhn, O., H. H. Hellmer, M. Rhein, C. Rodehacke, W. Roether, M. P. Schodlok, and M. Schröder, Evidence of deep- and bottom-water formation in the western Weddell Sea, *Deep Sea Research Part II: Topical Studies in Oceanography*, *55*(8-9), doi:10.1016/j.dsr2.2007.12.015, 2008.

Inall, M. E., F. Nilsen, F. R. Cottier, and R. Daae, Shelf/fjord exchange driven by coastal-trapped waves in the Arctic, *Journal of Geophysical Research: Oceans*, *120*(12), 8283–8303, doi:10.1002/2015jc011277, 2015.

Irvine-Fynn, T., and A. Hodson, Biogeochemistry and dissolved oxygen dynamics at a subglacial upwelling, Midtre Lovénbreen, Svalbard, *Annals of Glaciology*, *51*(56), doi:10.3189/172756411795931903, 2010.

Jackson, R. H., F. Straneo, and D. A. Sutherland, Externally forced fluctuations in ocean temperature at Greenland glaciers in non-summer months, *Nature Geoscience*, *7*(7), 503–508, doi:10.1038/ngeo2186, 2014.

Jacobs, S. S., A. Jenkins, C. F. Giulivi, and P. Dutrieux, Stronger ocean circulation and increased melting under Pine Island Glacier ice shelf, *Nature Geoscience*, *4*(8), doi:10.1038/ngeo1188, 2011.

Jenkins, A., The Impact of Melting Ice on Ocean Waters, *Journal of Physical Oceanography*, *29*(9), doi:10.1175/1520-0485(1999)029<2370:TIOMIO>2.0.CO;2, 1999.

Jenkins, A., and S. Jacobs, Circulation and melting beneath George VI Ice Shelf, Antarctica, *Journal of Geophysical Research*, *113*(C4), doi:10.1029/2007jc004449, 2008.

Johnson, H. L., A. Münchow, K. K. Falkner, and H. Melling, Ocean circulation and properties in Petermann Fjord, Greenland, *Journal of Geophysical Research*, *116*(C1), doi:10.1029/2010jc006519, 2011.

Joughin, I., M. Fahnestock, D. MacAyeal, J. L. Bamber, and P. Gogineni, Observation and analysis of ice flow in the largest Greenland ice stream, *Journal of Geophysical Research: Atmospheres*, *106*(D24), 34,021–34,034, doi:10.1029/2001jd900087, 2001.

Kanzow, T., The Expedition PS100 of the Research Vessel POLARSTERN to the Fram Strait in 2016 Reports on Polar and Marine Research, *Tech. Rep. 705*, Alfred Wegener Institute, Helmholtz Center for Polar and Marine Research, doi:10.2312/bzpm_0705_2017, 2017.

Kanzow, T., W.-J. von Appen, J. Schaffer, E. Köhn, T. Tsubouchi, N. Wilson, P. F. Lodeiro, F. Evers, and A. Wisotzki, Physical oceanography measured with ultra clean CTD/Watersampler-system during POLARSTERN cruise PS100 (ARK-XXX/2), PANGAEA, doi:10.1594/PANGAEA.871030, 2017a.

Kanzow, T., W.-J. von Appen, J. Schaffer, E. Köhn, T. Tsubouchi, N. Wilson, and A. Wisotzki, Physical oceanography measured with CTD/Large volume Watersampler-system during POLARSTERN cruise PS100 (ARK-XXX/2), PANGAEA, doi:10.1594/PANGAEA.871025, 2017b.

Kanzow, T., J. Schaffer, and G. Rohardt, Physical oceanography during POLARSTERN cruise PS109 (ARK-XXXI/4), doi:10.1594/pangaea.885358, 2018a.

Kanzow, T., J. Schaffer, and G. Rohardt, Physical oceanography measured on water bottle samples during POLARSTERN cruise PS109, doi:10.1594/pangaea.887108, 2018b.

Khan, S. A., K. H. Kjær, M. Bevis, J. L. Bamber, J. Wahr, K. K. Kjeldsen, A. A. Bjørk, N. J. Korsgaard, L. A. Stearns, M. R. van den Broeke, L. Liu, N. K. Larsen, and I. S. Muresan, Sustained mass loss of the northeast Greenland ice sheet triggered by regional warming, *Nature Climate Change*, *4*(4), doi:10.1038/nclimate2161, 2014.

Kirillov, S., I. Dmitrenko, S. Rysgaard, D. Babb, L. T. Pedersen, J. Ehn, J. Bendtsen, and D. Barber, Storm-induced water dynamics and thermohaline structure at the tidewater Flade Isblink Glacier outlet to the Wandel Sea (NE Greenland), *Ocean Science*, *13*(6), 947–959, doi:10.5194/os-13-947-2017, 2017.

Kjeldsen, K., N. Korsgaard, A. Bjørk, S. Khan, J. Box, S. Funder, N. Larsen, J. Bamber, W. Colgan, M. van den Broeke, M.-L. Siggaard-Andersen, C. Nuth, A. Schomacker, C. Andresen, E. Willerslev, and K. Kjær, Spatial and temporal distribution of mass loss from the Greenland Ice Sheet since AD 1900, *Nature*, *528*(7582), 396–400, doi:10.1038/nature16183, 2015.

Klinck, J. M., J. J. O'Brien, and H. Svendsen, A Simple Model of Fjord and Coastal Circulation Interaction, *Journal of Physical Oceanography*, *11*(12), 1612–1626, doi:10.1175/1520-0485(1981)011<1612:asmofa>2.0.co;2, 1981.

Kobayashi, S., Y. Ota, Y. Jarada, A. E. M. Mariya, H. Onoda, K. Onogi, H. Kamahori, C. Kobashi, H. Endo, K. Miyaoka, and K. Takahashi, The JRA-55 Reanalysis: General Specifications and Basic Characteristics, *Journal of the Meteorological Society of Japan. Ser. II*, *93*(1), 5–48, doi:10.2151/jmsj.2015-001, 2015.

Lilly, J., Lecture notes on time series analysis, http://www.jmlilly.net/index.html, 2017a.

Lilly, J. M., jLab: A data analysis package for Matlab, *Tech. rep.*, http://www.jmlilly.net/jmlsoft.html., 2017b.

Lilly, J. M., and S. C. Olhede, Generalized Morse wavelets as a superfamily of analytic wavelets., *IEEE Transactions on Signal Processing*, *60*(11), 2012.

Mackas, D. L., K. L. Denman, and A. F. Bennett, Least squares multiple tracer analysis of water mass composition, *Journal of Geophysical Research*, *92*(C3), doi:10.1029/jc092ic03p02907, 1987.

Makinson, K., and K. W. Nicholls, Modeling tidal currents beneath Filchner-Ronne Ice Shelf and on the adjacent continental shelf: Their effect on mixing and transport, *Journal*

of Geophysical Research: Oceans, *104*(C6), 13,449–13,465, doi:10.1029/1999jc900008, 1999.

Makinson, K., P. R. Holland, A. Jenkins, K. W. Nicholls, and D. M. Holland, Influence of tides on melting and freezing beneath Filchner-Ronne Ice Shelf, Antarctica, *Geophysical Research Letters*, *38*(6), n/a–n/a, doi:10.1029/2010gl046462, 2011.

Martin, T., M. Steele, and J. Zhang, Seasonality and long-term trend of Arctic Ocean surface stress in a model, *Journal of Geophysical Research: Oceans*, *119*(3), 1723–1738, doi:10.1002/2013jc009425, 2014.

Martinerie, P., D. Raynaud, D. M. Etheridge, J.-M. Barnola, and D. Mazaudier, Physical and climatic parameters which influence the air content in polar ice, *Earth and Planetary Science Letters*, *112*(1-4), doi:10.1016/0012-821x(92)90002-d, 1992.

Marzeion, B., G. Kaser, F. Maussion, and N. Champollion, Limited influence of climate change mitigation on short-term glacier mass loss, *Nature Climate Change*, *8*(4), 305–308, doi:10.1038/s41558-018-0093-1, 2018.

Mayer, C., N. Reeh, F. Jung-Rothenhäusler, P. Huybrechts, and H. Oerter, The subglacial cavity and implied dynamics under Nioghalvfjerdsfjorden Glacier, NE-Greenland, *Geophysical Research Letters*, *27*(15), doi:10.1029/2000gl011514, 2000.

Mayer, C., J. Schaffer, T. Hattermann, D. Floricioiu, L. Krieger, P. A. Dodd, T. Kanzow, C. Licciulli, and C. Schannwell, Large ice loss variability at Nioghalvfjerdsfjorden Glacier, Northeast-Greenland, *Nature Communications*, *9*(1), doi:10.1038/s41467-018-05180-x, 2018.

Messerli, A., N. B. Karlsson, and A. Grinsted, Brief Communication: 2014 velocity and flux for five major Greenland outlet glaciers using ImGRAFT and Landsat-8, *The Cryosphere Discussions*, *8*(6), 6235–6250, doi:10.5194/tcd-8-6235-2014, 2014.

Millgate, T., P. R. Holland, A. Jenkins, and H. L. Johnson, The effect of basal channels on oceanic ice-shelf melting, *Journal of Geophysical Research: Oceans*, *118*(12), 6951–6964, doi:10.1002/2013jc009402, 2013.

Moffat, C., Wind-driven modulation of warm water supply to a proglacial fjord, Jorge Montt Glacier, Patagonia, *Geophysical Research Letters*, *41*(11), 3943–3950, doi:10.1002/2014gl060071, 2014.

Morlighem, M., C. N. Williams, E. Rignot, L. An, J. E. Arndt, J. L. Bamber, G. Catania, N. Chauché, J. A. Dowdeswell, B. Dorschel, I. Fenty, K. Hogan, I. Howat, A. Hubbard, M. Jakobsson, T. M. Jordan, K. K. Kjeldsen, R. Millan, L. Mayer, J. Mouginot, B. P. Y. Noël, C. Cofaigh, S. Palmer, S. Rysgaard, H. Seroussi, M. J. Siegert, P. Slabon, F. Straneo, M. R. van den Broeke, W. Weinrebe, M. Wood, and K. B. Zinglersen, BedMachine v3: Complete Bed Topography and Ocean Bathymetry Mapping of Greenland From Multibeam Echo Sounding Combined With Mass Conservation, *Geophysical Research Letters*, *44*(21), 11,051–11,061, doi:10.1002/2017gl074954, 2017.

Mortensen, J., K. Lennert, J. Bendtsen, and S. Rysgaard, Heat sources for glacial melt in a sub-Arctic fjord (Godthåbsfjord) in contact with the Greenland Ice Sheet, *Journal of Geophysical Research*, *116*(C1), doi:10.1029/2010jc006528, 2011.

Mortensen, J., J. Bendtsen, R. J. Motyka, K. Lennert, M. Truffer, M. Fahnestock, and S. Rysgaard, On the seasonal freshwater stratification in the proximity of fast-flowing tidewater outlet glaciers in a sub-Arctic sill fjord, *Journal of Geophysical Research: Oceans*, *118*(3), 1382–1395, doi:10.1002/jgrc.20134, 2013.

Motyka, R. J., L. Hunter, K. A. Echelmeyer, and C. Connor, Submarine melting at the terminus of a temperate tidewater glacier, LeConte Glacier, Alaska, U.S.A., *Annals of Glaciology*, *36*, 57–65, doi:10.3189/172756403781816374, 2003.

Motyka, R. J., M. Truffer, M. Fahnestock, J. Mortensen, S. Rysgaard, and I. Howat, Submarine melting of the 1985 Jakobshavn Isbrae floating tongue and the triggering of the current retreat, *Journal of Geophysical Research: Earth Surface*, *116*(F1), n/a–n/a, doi:10.1029/2009jf001632, 2011.

Mouginot, J., E. Rignot, B. Scheuchl, I. Fenty, A. Khazendar, M. Morlighem, A. Buzzi, and J. Paden, Fast retreat of Zachariae Isstrom, northeast Greenland, *Science*, *350*(6266), doi:10.1126/science.aac7111, 2015.

Mueller, R. D., L. Padman, M. S. Dinniman, S. Y. Erofeeva, H. A. Fricker, and M. A. King, Impact of tide-topography interactions on basal melting of Larsen C Ice Shelf, Antarctica, *Journal of Geophysical Research: Oceans*, *117*(C5), n/a–n/a, doi:10.1029/2011jc007263, 2012.

Nerem, R. S., B. D. Beckley, J. T. Fasullo, B. D. Hamlington, D. Masters, and G. T. Mitchum, Climate-change–driven accelerated sea-level rise detected in the altimeter era, *Proceedings of the National Academy of Sciences*, *115*(9), 2022–2025, doi:10.1073/pnas.1717312115, 2018.

Noël, B., W. J. van de Berg, J. M. van Wessem, E. van Meijgaard, D. van As, J. T. M. Lenaerts, S. Lhermitte, P. K. Munneke, C. J. P. P. Smeets, L. H. van Ulft, R. S. W. van de Wal, and M. R. van den Broeke, Modelling the climate and surface mass balance of polar ice sheets using RACMO2 – Part 1: Greenland (1958–2016), *The Cryosphere*, *12*(3), 811–831, doi:10.5194/tc-12-811-2018, 2018.

Paul, F., T. Bolch, K. Briggs, A. Kääb, M. McMillan, R. McNabb, T. Nagler, C. Nuth, P. Rastner, T. Strozzi, and J. Wuite, Error sources and guidelines for quality assessment of glacier area, elevation change, and velocity products derived from satellite data in the Glaciers_cci project, *Remote Sensing of Environment*, *203*, 256–275, doi:10.1016/j.rse.2017.08.038, 2017.

Pawlowicz, R., B. Beardsley, and S. Lentz, Classical tidal harmonic analysis including error estimates in MATLAB using T_TIDE, *Computers & Geosciences*, *28*(8), 929–937, doi:10.1016/s0098-3004(02)00013-4, 2002.

Pugh, D., and P. Woodworth, *Sea-Level Science*, Cambridge University Press, 2014.

Reeh, N., H. H. Thomsen, A. K. Higgins, and A. Weidick, Sea ice and the stability of north and northeast Greenland floating glaciers, *Annals of Glaciology*, *33*, doi:10.3189/172756401781818554, 2001.

Richter, M., Fram Strait recirculation and the East Greenland Current: Spatial structure north of 79 N, Master's thesis, University of Bremen, 2017.

Rogers, J. C., The role of Fram Strait winter cyclones on sea ice flux and on Spitsbergen air temperatures, *Geophysical Research Letters*, *32*(6), doi:10.1029/2004gl022262, 2005.

Rohardt, G., CTD Data Processing Report - RV POLARSTERN Cruise PS109, *Tech. rep.*, 2018.

Rudels, B., G. Björk, J. Nilsson, P. Winsor, I. Lake, and C. Nohr, The interaction between waters from the Arctic Ocean and the Nordic Seas north of Fram Strait and along the East Greenland Current: results from the Arctic Ocean-02 Oden expedition, *Journal of Marine Systems*, *55*(1-2), 1–30, doi:10.1016/j.jmarsys.2004.06.008, 2005.

Schaffer, J., Ocean impact on the 79 North Glacier, Northeast Greenland, Ph.D. thesis, University of Bremen, 2017.

Schaffer, J., R. Timmermann, J. E. Arndt, S. S. Kristensen, C. Mayer, M. Morlighem, and D. Steinhage, A global high-resolution data set of ice sheet topography, cavity geometry and ocean bathymetry, *Earth System Science Data Discussions*, doi:10.5194/essd-2016-3, 2016.

Schaffer, J., W.-J. von Appen, P. A. Dodd, C. Hofstede, C. Mayer, L. de Steur, and T. Kanzow, Warm water pathways toward Nioghalvfjerdsfjorden Glacier, Northeast Greenland, *Journal of Geophysical Research: Oceans*, *122*(5), doi:10.1002/2016jc012462, 2017.

Schneider, W., and G. Budéus, On the generation of the Northeast Water Polynya, *Journal of Geophysical Research*, *100*(C3), doi:10.1029/94jc02349, 1995.

Schneider, W., and G. Budéus, Summary of the Northeast Water Polynya formation and development (Greenland sea), *Journal of Marine Systems*, *10*(1-4), 107–122, doi:10.1016/s0924-7963(96)00075-9, 1997.

Shaw, P.-T., and G. T. Csanady, Topographic Waves over the Continental Slope, *Journal of Physical Oceanography*, *18*(6), 813–822, doi:10.1175/1520-0485(1988)018<0813:twotcs>2.0.co;2, 1988.

Shepherd, A., E. R. Ivins, G. A, V. R. Barletta, M. J. Bentley, S. Bettadpur, K. H. Briggs, D. H. Bromwich, R. Forsberg, N. Galin, M. Horwath, S. Jacobs, I. Joughin, M. A. King, J. T. M. Lenaerts, J. Li, S. R. M. Ligtenberg, A. Luckman, S. B. Luthcke, M. McMillan, R. Meister, G. Milne, J. Mouginot, A. Muir, J. P. Nicolas, J. Paden, A. J. Payne, H. Pritchard, E. Rignot, H. Rott, L. S. Sorensen, T. A. Scambos, B. Scheuchl, E. J. O. Schrama, B. Smith, A. V. Sundal, J. H. van Angelen, W. J. van de Berg, M. R. van den Broeke, D. G. Vaughan, I. Velicogna, J. Wahr, P. L. Whitehouse, D. J. Wingham, D. Yi, D. Young, and H. J. Zwally, A Reconciled Estimate of Ice-Sheet Mass Balance, *Science*, *338*(6111), 1183–1189, doi:10.1126/science.1228102, 2012.

Spreen, G., L. Kaleschke, and G. Heygster, Sea ice remote sensing using AMSR-E 89-GHz channels, *Journal of Geophysical Research*, *113*(C2), doi:doi:10.1029/2005JC003384, 2008.

Stramska, M., A. Jankowski, and A. Cieszyńska, Surface currents in the Porsanger fjord in northern Norway, *Polish Polar Research*, *37*(3), doi:10.1515/popore-2016-0018, 2016.

Straneo, F., and C. Cenedese, The Dynamics of Greenland's Glacial Fjords and Their Role in Climate, *Annual Review of Marine Science*, *7*(1), 89–112, doi:10.1146/annurev-marine-010213-135133, 2015.

Straneo, F., and P. Heimbach, North Atlantic warming and the retreat of Greenland's outlet glaciers, *Nature*, *504*(7478), doi:10.1038/nature12854, 2013.

Straneo, F., G. S. Hamilton, D. A. Sutherland, L. A. Stearns, F. Davidson, M. O. Hammill, G. B. Stenson, and A. Rosing-Asvid, Rapid circulation of warm subtropical waters in a major glacial fjord in East Greenland, *Nature Geoscience*, *3*(3), 182–186, doi:10.1038/ngeo764, 2010.

Straneo, F., R. G. Curry, D. A. Sutherland, G. S. Hamilton, C. Cenedese, K. Våge, and L. A. Stearns, Impact of fjord dynamics and glacial runoff on the circulation near Helheim Glacier, *Nature Geoscience*, *4*(5), doi:10.1038/ngeo1109, 2011.

Sutherland, D. A., G. E. Roth, G. S. Hamilton, S. H. Mernild, L. A. Stearns, and F. Straneo, Quantifying flow regimes in a Greenland glacial fjord using iceberg drifters, *Geophysical Research Letters*, *41*(23), 8411–8420, doi:10.1002/2014gl062256, 2014a.

Sutherland, D. A., F. Straneo, and R. S. Pickart, Characteristics and dynamics of two major Greenland glacial fjords, *Journal of Geophysical Research: Oceans*, *119*(6), 3767–3791, doi:10.1002/2013jc009786, 2014b.

Talley, L. D., G. Pickard, W. Emery, and J. Swift, *Descriptive Physical Oceanography: An Introduction (Sixth Edition)*, 6 ed., Elsevier, Boston, 2011.

Thurnherr, A. M., A Practical Assessment of the Errors Associated with Full-Depth LADCP Profiles Obtained Using Teledyne RDI Workhorse Acoustic Doppler Current Profilers, *Journal of Atmospheric and Oceanic Technology*, *27*(7), 1215–1227, doi:10.1175/2010jtecho708.1, 2010.

Tomczak, M., and D. G. B. Large, Optimum multiparameter analysis of mixing in the thermocline of the eastern Indian Ocean, *Journal of Geophysical Research*, *94*(C11), doi:10.1029/jc094ic11p16141, 1989.

Topp, R., and M. Johnson, Winter intensification and water mass evolution from yearlong current meters in the Northeast Water Polynya, *Journal of Marine Systems*, *10*(1), doi:https://doi.org/10.1016/S0924-7963(96)00083-8, 1997.

van den Broeke, M., J. Bamber, J. Ettema, E. Rignot, E. Schrama, W. J. van de Berg, E. van Meijgaard, I. Velicogna, and B. Wouters, Partitioning Recent Greenland Mass Loss, *Science*, *326*(5955), doi:10.1126/science.1178176, 2009.

von Appen, W.-J., U. Schauer, T. Hattermann, and A. Beszczynska-Möller, Seasonal Cycle of Mesoscale Instability of the West Spitsbergen Current, *Journal of Physical Oceanography*, *46*(4), 1231–1254, doi:10.1175/jpo-d-15-0184.1, 2016.

Washam, P., A. Münchow, and K. W. Nicholls, A decade of ocean changes impacting the ice shelf of Petermann Gletscher, Greenland, *Journal of Physical Oceanography*, doi:10.1175/jpo-d-17-0181.1, 2018.

WCRP Global Sea Level Budget Group, Global sea-level budget 1993–present, *Earth System Science Data*, *10*(3), 1551–1590, doi:10.5194/essd-10-1551-2018, 2018.

Webber, B. G. M., K. J. Heywood, D. P. Stevens, P. Dutrieux, E. P. Abrahamsen, A. Jenkins, S. S. Jacobs, H. K. Ha, S. H. Lee, and T. W. Kim, Mechanisms driving variability in the ocean forcing of Pine Island Glacier, *Nature Communications*, *8*, 14,507, doi:10.1038/ncomms14507, 2017.

Weijer, W., M. E. Maltrud, M. W. Hecht, H. A. Dijkstra, and M. A. Kliphuis, Response of the Atlantic Ocean circulation to Greenland Ice Sheet melting in a strongly-eddying ocean model, *Geophysical Research Letters*, *39*(9), doi:10.1029/2012gl051611, 2012.

Williams, M. J. M., A. Jenkins, and J. Determann, Physical controls on ocean circulation beneath ice shelves revealed by numerical models, in *Ocean, Ice, and Atmosphere: Interactions at the Antarctic Continental Margin*, pp. 285–299, American Geophysical Union, doi:10.1029/ar075p0285, 1998.

Wilson, N., F. Straneo, and P. Heimbach, Submarine melt rates and mass balance for Greenlands remaining ice tongues, *The Cryosphere Discussions*, doi:10.5194/tc-2017-99, 2017.

Wilson, N. J., and F. Straneo, Water exchange between the continental shelf and the cavity beneath Nioghalvfjerdsbrae (79 North Glacier), *Geophysical Research Letters*, *42*(18), doi:10.1002/2015gl064944, 2015.

Appendix

The following content is an extract of the thesis paper that I prepared from 11/2017 to 02/2018 dealing with the properties of glacially modified water at the 79 North Glacier. Here, it is shown to provide the reader with details on the methods of the melt water fraction analysis described in section 2.1.3.

Abstract of

Properties and circulation of glacially modifed waters at the 79 North Glacier

thesis paper prepared by Luisa von Albedyll, 1.02.2018

The extensive floating ice tongue of the 79 North glacier (79NG) in Northeast Greenland experiences significant thinning. Atlantic Intermediate Water (AIW) exceeding 1°C is present in the glacier cavity and is suspected to be responsible for melting at the glacier base causing the observed thinning. Mixing of the AIW with basal melt water and subglacial runoff, forms glacially modified AIW (mAIW). Hydrographic measurements taken during the R/V *Polarstern cruise* in 2016 are used to analyze the properties of mAIW. The mAIW is characterized by high potential temperatures, low oxygen concentrations and is found in a density range between 27.0–27.75 $\mathrm{kg\,m^{-3}}$ corresponding to a depth of approximately 90–260 m. An Optimum Multiparameter Analysis based on potential temperature, salinity and dissolved oxygen revealed that the mAIW consists of approximately 2% glacial melt water. Basal melt water dominates accounting for three quarters of the total melt water content. The mAIW found at the mouth of Dijmphna Sund, one of the possible export pathways of mAIW, is characterized by the highest concentration of glacial melt water. A moored time series from Dijmphna Sund covering one year gives first insights into the export of mAIW through Dijmphna Sund. The prevailing flow direction points out of the fjord suggesting that Dijmphna Sund might play an important role in the export of mAIW from the 79NG onto the continental shelf. However, the strength of the speed into the prevailing flow direction varies between periods of strong speeds (0.4–0.65 $\mathrm{m\,s^{-1}}$) and periods of weak currents (−0.15–0.15 $\mathrm{m\,s^{-1}}$). Increasing melt water contributions linked to the observed glacier thinning and possible warming of AIW may not only change the characteristics of mAIW in the vicinity of the 79NG but also alter hydrograhpic properties on the Northeast Greenland continental shelf presumably affecting the shelf circulation.

Methods

To characterize and distinguish mAIW at different locations, the relative contributions of the source water types that form mAIW are analyzed. Here, an end-member analysis as described in the following is used to achieve this goal.

End-member water analysis is based on the idea of a unique set of water mass properties whose sinks and sources are only found at boundary interfaces (e.g. ocean/atmopshere, ocean/ice, *Mackas et al.*, 1987). When transported away from the formation site, those properties do not change unless mixing occurs, where the conservative properties combine linearly to a new set of properties. This linearity allows to decompose a new water mass into its source water types by setting up a system of linear equations. In the case of an over-determined system (more properties than source water types), it can be solved by an Optimum Multiparameter Analysis (OMP, *Hinrichsen and Tomczak*, 1993; *Huhn et al.*, 2008; *Tomczak and Large*, 1989).

In this study, the OMP is limited to the three end-members that reflect the source water masses of the glacially modified waters at the 79NG: Atlantic Intermediate Water (AIW), basal melt water (BMW) and subglacial runoff (SGR). This formation hypothesis is valid under the assumption that (1) inflow into the cavity takes place in a depth where only AIW is present (shown by *Schaffer*, 2017), and (2) analyzed casts are close enough to the cavity outflow that no significant mixing with other ambient water masses (e.g. PW, KW) has occurred before the measurements were made. In order to ensure (2) the minimum glacier draft height (90 m, also below the halocline) will be regarded here as the limit of any ongoing PW or atmospheric influence on the water column. Also, the analysis will be concerned only with casts that are located close to the calving front and exhibit characteristics associated with the mAIW. AIW, BMW and SGR end-members are defined in potential temperature, salinity and oxygen concentrations.

End-members

The end-members of the AIW are found by picking the warmest and most saline measurements taken at the 79NG, i.e. the most outstanding peaks in Θ-S space. To account for variability, a mean of 12 peaks is used to define the final end-member (*Huhn et al.*, 2008). The standard deviation expresses the error of the end-member definition. Oxygen measurements corresponding to the points chosen in Θ-S space are averaged, when available, to define the AIW oxygen end-member.

The temperatures of the glacial end-members are defined by thermodynamical considerations of their formation process. In a closed ice-seawater system, one can break down the melting process to: (1) Heat conduction from water to ice to heat it from its far-field temperature Θ_i to its in-situ freezing point temperature Θ_f. (2) Absorption of latent heat L for the phase change. (3) Mixing of melt water at freezing temperature with the surrounding seawater. To facilitate the handling of this phase change in the end-member analysis, the potential temperature of the melt water is defined as its effective potential temperature (Θ_{eff}, scaled to 1 kg) that incorporates heat conduction and the latent heat of its phase change:

$$\Theta_{eff} = \Theta_f - \frac{L}{c_w} - \frac{c_i}{c_w}(\Theta_f - \Theta_i) \tag{5.1}$$

where c_i and c_w represent the specific heat capacities at constant pressure of ice and seawater, respectively (*Gade*, 1979; *Jenkins*, 1999). As most of basal melt takes place at the grounding line in 600 m depth, Θ_f was calculated based on the salinity measurement obtained from the 79NG cavity at grounding line depth (*Schaffer*, 2017). Its error was found by taking the standard deviation over all depths from the grounding line to the calving front (90–600 m depth) and over a salinity range of 30–35 (*Schaffer*, 2017). The uncertainty of the BMW end-member of this study is found by error propagation.
Mixing seawater with glacial runoff does not require latent heat for melting, i.e. its temperature is assumed to be at the in-situ freezing point. This value was obtained by averaging over all in-situ freezing points (at zero salinity) from 0-600 m depth (*Schaffer*, 2017).

Salinity is assumed to be negligible for both glacial end-members (*Jenkins*, 1999). Oxygen end-members for the glacial source types may be found by theoretical considerations or by extrapolation. Firn transforms into ice via packing and sintering of snow grains while air pockets within the ice are isolated from the atmosphere. Depending on air temperature and atmospheric pressure at the formation site, the enclosed pore volume varies, but can be approximated to 120–130 $\mathrm{ml\,kg^{-1}}$ air per ice for surface elevations of 1000–1500 m in the catchment basin (*Martinerie et al.*, 1992). Taking into account that 21% of air comprises of oxygen, and basal ice dissolves under high pressure leading to the complete dissolution of the gases within it to the ambient waters, one can estimate oxygen concentrations of $27\,\mathrm{ml\,l^{-1}}$ for the BMW end-member (*Hellmer et al.*, 1998; *Jenkins and Jacobs*, 2008; *Johnson et al.*, 2011).
Subglacial runoff is far more variable and more difficult to model. *Irvine-Fynn and Hodson* (2010) and *Beaird et al.* (2015) assume that surface melt water is at saturation or even supersatured with gases when in contact with the atmosphere because melt water lakes are rather shallow and water drains in turbulent ways down active crevasses. Assuming a temperature of 0 °C, a salinity of zero and saturation, this results in $10\,\mathrm{ml\,l^{-1}}$.

In most studies however, oxygen concentration of the glacial end-members is found by extrapolation of the mixing line to the potential temperature and salinity properties of the glacial end-members (*Heuzé et al.*, 2017; *Jenkins*, 1999; *Jenkins and Jacobs*, 2008; *Johnson et al.*, 2011). Line fitting is restricted to water with density larger than 27.0 to capture only inflow and outflow signals (*Schaffer*, 2017). The uncertainty of the fitted end-members is expressed by the uncertainty of the linear fit.

OMP analysis

Each observed property of the water parcel d_{obs} is expressed as a linear combination of fractions x_i of the source-water masses and their characteristic properties A_i. Mass conservation is ensured by adding one equation that sums up all fractions to 1.

$$d_{obs,i} = \Sigma\ x_i A_i + R_i \tag{5.2}$$

In the ideal case, all observations can be fully explained by the linear equations and the residual R_i is zero. However, uncertainties in the measurements and/or the source water type definitions will lead to nonzero residuals. Therefore, a combination of positive mixing

ratios is searched that minimizes the residual, i.e. the deviation between observed and computed properties (*Huhn et al.*, 2008; *Mackas et al.*, 1987). This is commonly done by finding the least squares solution of the problem in matrix formulation:

$$\boldsymbol{A}\boldsymbol{x} - \boldsymbol{d}_{obs} = \boldsymbol{R} \tag{5.3}$$

Assuming that mixing takes place between n source water types and that $m-1$ water properties are available for analysis, A is a $m \times n$ matrix consisting of the properties of each source water mass type, x is a vector of the unknown mixing rations of size n, d_{obs} a vector of the observed properties with size m, and R a vector of size m that accounts for the residuals. Minimizing the residuals in a least square sense is done by finding a solution vector x in a way that the gradient of the *cost function* F (∇_x(F), function of the residuals depending on x) is zero.

$$\begin{aligned} \boldsymbol{F} =& \boldsymbol{R}^T\boldsymbol{R} && (5.4)\\ =& (\boldsymbol{A}\boldsymbol{x} - \boldsymbol{d}_{obs})^T(\boldsymbol{A}\boldsymbol{x} - \boldsymbol{d}_{obs}) \\ \boldsymbol{\nabla}_{\boldsymbol{x}}(\boldsymbol{F}) =& 0 && (5.5) \end{aligned}$$

This leads to the so called normal equations that can solved easily for x by either Gauss elimination method or by inverting $\boldsymbol{A}^T\boldsymbol{A}$.

$$(\boldsymbol{A}^T\boldsymbol{A})\boldsymbol{x} = \boldsymbol{A}^T\boldsymbol{d}_{obs} \tag{5.6}$$

A large advantage of this approach is that each property can be weighted individually. At first, all quantities are normalized by their mean and range. For example, one subtracts the mean of all temperature end-members ($\overline{A_T}$) from the individual end-member and divides by the standard deviation of the mean (σ_{A_T}).

$$A_{norm\{i,T\}} = \frac{A_{i,T} - \overline{A_T}}{\sigma_{A_T}} \tag{5.7}$$

$$d_{norm\{i,T\}} = \frac{d_{i,T} - \overline{A_T}}{\sigma_{A_T}} \tag{5.8}$$

Second, the matrix is weighted such that each property has an influence proportional to its ability to distinguish between the end-members (expressed by its variance $\sigma^2_{A_T}$), and is inversely proportional to the largest uncertainty in the end-member definition ($\epsilon^2_{T,max}$). To find the largest uncertainty, every end-member is assigned an uncertainty, either the uncertainty of the end-member definition or, if larger, the measurement uncertainty of the property. Then, the largest uncertainty of a property is taken for the weighting. Consequently, the weighting factor (here for temperature) is defined as (*Beaird et al.*, 2015; *Tomczak and Large*, 1989):

$$w_T = \left(\frac{\sigma_{A_T}}{\epsilon_{T,max}}\right)^2 \tag{5.9}$$

Mass conservation is weighted like temperature (*Beaird et al.*, 2015). The information are implemented to the linear equation system by the diagonal weight matrix W that changes

equation 5 to:

$$\boldsymbol{F} = \boldsymbol{R}^T\boldsymbol{R} = (\boldsymbol{A}_{norm}\boldsymbol{x} - \boldsymbol{d}_{norm})^T\boldsymbol{W}^T\boldsymbol{W}(\boldsymbol{A}_{norm}\boldsymbol{x} - \boldsymbol{d}_{norm}) \tag{5.10}$$

with

$$\boldsymbol{W} = \begin{pmatrix} w_T & 0 & 0 & 0 \\ 0 & w_{Ox} & 0 & \\ 0 & 0 & w_S & 0 \\ 0 & 0 & 0 & w_{M.} \end{pmatrix} \tag{5.11}$$

In the case of a system with three source water types and only two parameters (plus mass conservation), the linear equations simplify to the classical mixing triangle and solutions are given by e.g. *Jenkins* (1999) and *Jacobs et al.* (2011). Those are used to calculate water mass fractions for the XCTD casts where no oxygen measurements are available.
In this study, the weighted linear equations are solved using the Matlab (Student Version R2017b) built in function *lsqnonneg* that solves constraint linear equation systems for both, the over-determined and the critical case. The calculated residuals of the equations are used as a measure of quality (*Huhn et al.*, 2008).

Uncertainty assessement

To quantify the uncertainty of the water mass fractions, the set of linear equation is solved 1000 times with random end-members taken from a normal distribution. The distribution is designed with a mean equal to the undisturbed end-member and a standard deviation equal to its uncertainty. For each pertubation, the difference between undisturbed and disturbed water mass fraction is calculated.

Results of Uncertainty assessment

To assess the uncertainty of the water mass fractions shown previously, the OMP is repeated 1000 times with end-members that are changed randomly within their uncertainty range. This uncertainty range is estimated by taking the larger of two uncertainties. (1) either the uncertainty in the the end-member definition (see Tab. 5.1) or (2) the measurement error of the property itself. The largest uncertainty for the temperature and salinity end-members is the end-member definition. For oxygen, the the oxygen measurement error of 2% of saturation exceeds the uncertainty of the end-member, and therefore this limit is used, corresponding to $9.6901\,\mu\mathrm{mol}\,\mathrm{l}^{-1}$. The random distribution of the end-members is depicted graphically in Fig. 5.1.

A relative error is calculated for each water mass by taking the difference between the disturbed and undisturbed solution. This difference is expressed as percentage of the undisturbed fraction to account for fractions spanning more than one order of magnitude (Fig. 5.1). SGR fractions have a standard deviation of 5.3% (relative to the fraction), but suffer from outliers that are removed prior to further calculations. BMW varies stronger with a standard deviation of 11.53%, but has less outliers.

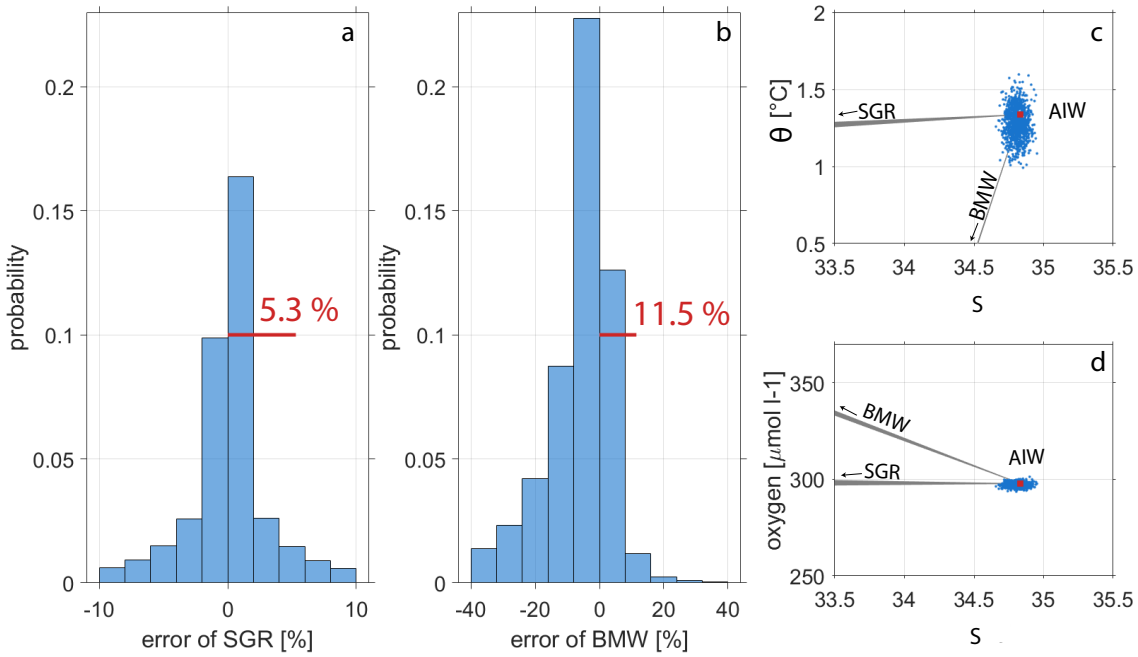

Figure 5.1: Uncertainty of the water mass fractions and statistically disturbed end-members. The relative uncertainty of SGR (a) and BMW (b) is expressed in percentage of the undisturbed fraction. The standard deviation of SGR and BMW is 5.3% and 11.5%, respectively. c and d: All disturbed AIW end-members are shown as a point cloud in Θ-S (c) and Oxygen-S (d) diagrams. The gray lines show the mixing lines of the disturbed glacial end-members. The increasing width of the line displays their uncertainty, respectively

end-member-definitions

Table 5.1 summarizes the end-members with their uncertainty.

Table 5.1: End-members with uncertainties and relative weights of the properties

	AIW	BMW	SGR	weight
Θ [°C]	1.336 ± 0.106	-93 ± 0.27	-0.22 ± 0.13	4003
salinity [ ]	34.834 ± 0.046	0	0	17 927
oxygen [μmol l^{-1}]	295 ± 1.0867	1253 ± 8	311 ± 2	446